Conversations between the Earth and Atmosphere

A study on the seismo-acoustic wavefield

Averbuch, Gil

DOI
10.4233/uuid:6ee6ec6d-9ffc-461f-9278-da38a7409d01

Publication date
2020

Document Version
Final published version

Citation (APA)
Averbuch, G. (2020). *Conversations between the Earth and Atmosphere: A study on the seismo-acoustic wavefield*. [Dissertation (TU Delft), Delft University of Technology]. https://doi.org/10.4233/uuid:6ee6ec6d-9ffc-461f-9278-da38a7409d01

Conversations between the Earth and Atmosphere

A study on the seismo-acoustic wavefield

Conversations between the Earth and Atmosphere

A study on the seismo-acoustic wavefield

Dissertation

for the purpose of obtaining the degree of doctor
at Delft University of Technology,
by the authority of the Rector Magnificus, prof. dr. ir. T.H.J.J. van der Hagen,
chair of the Board for Doctorates,
to be defended publicly on
Monday, 9 of March 2020 at 15:00 o'clock

by

Gil AVERBUCH

Master of Science in Geophysics, Tel-Aviv University, Israel
born in Bat-Yam, Israel

This dissertation has been approved by the promotor.

Composition of the doctoral committee:

Rector Magnificus	chairman
Prof. dr. L. G. Evers	Delft University of Technology, promotor

Independent members:

Prof. dr. ir. C. P. A. Wapenaar	Delft University of Technology
Prof. dr. ir. E. C. Slob	Delft University of Technology
Prof. dr. J. Trampert	Utrecht University, the Netherlands
Prof. dr. O. A. Godin	Naval Postgraduate School, United States
Prof. dr. R. M. Waxler	University of Mississippi, United States
Dr. D. N. Green	AWE Blacknest, United Kingdom

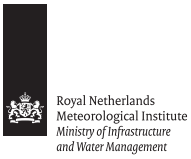

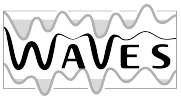

Keywords: infrasound, seismo-acoustics, wave propagation, array processing

Cover illustration: Tslil Strauss

ISBN 978-94-6384-120-7

Typesetting system: LaTeX.
Printed by Proefschriften Printen, Ede, the Netehrlands.

An electronic version of this dissertation is available at
`http://repository.tudelft.nl/`.

For my family

Preface

"There are three rules to succeed...unfortunately, no one knows what they are."

John Gill

My journey of writing this dissertation started, unofficially, at the end of my bachelor at Tel Aviv University. Inspired by Dr. Dan Kosloff and Dr. Ran Bachrach, who introduced me to research and numerical methods, I decided to pursue a masters degree. Dr. Colin Price, my masters supervisor, was the first to present me to the field of infrasound. Thanks to his endless support and freedom, I found my way into the the field of seismo-acoustics. Colin, thank you for giving me this priceless opportunity.

The EGU meeting in Vienna, in April 2015, was the next significant event in my journey. When I first met Dr. Läslo Evers, I saw a tall man with round glasses, colorful pants (probably green or orange) hanged by suspenders, and a big smile. At this moment I already had a good feeling about this meeting. A one-hour coffee meeting led to a job offer, which I immediately accepted. Coming to the Netherlands is not an obvious decision for a climber, but it's pretty close to Fontainebleau, so I thought that it is not that bad. Eventually, it turned out to be one of the best decisions I ever made.

Upon starting my Ph.D. I was lucky to join the WAVES project. This project brought together a group of smart, exciting, and fun scientists who are fascinated by wave phenomena. Thanks to all the WAVES participants for many interesting and fun times in conferences, workshops, and bars.

In the Netherlands, I was proud to be part of two respected departments; the Ap-

plied Geophysics department at TU Delft, and the R&D Department of Seismology and Acoustics at the Royal Netherlands Meteorological Institute (KNMI). Surrounded by many motivated scientists, these places provided the breeding ground for many interesting discussions, brainstorming, new ideas, finding solutions, and discovering many more open questions. I would like to thank Christian Reinicke, who was also part of WAVES, for interesting scientific discussion, lot's of funny moments, and many great trips to wherever WAVES sent us. Big ups to the support teams of both departments, Brigitta Kamphuis-van Thoor, Marlijn Ammerlaan, Lydia Broekhuijsen-Bentvelzen, Margot Bosselaar-Perk, Marja Roep-Van der Klis, Marijke Schillemans-Van Tuijl, and Ralf Haak. Special thanks to Dr. Kees Wapenaar and Dr. Evert Slob for always willing to help with mathematical questions.

The unique link between these two excellent institutes is the seismo-acoustic group, lead by Dr. Läslo Evers. For four years, besides being my colleagues, everyone within this group also became a close friend. Läslo, Jelle, Pieter, Shahar, Kees, Madelon, and Ollie. Thank you for many joint projects, conferences, discussions, and fun times. Being part of this diverse group allowed me to learn a lot from each one's philosophy and evolve as a scientist. Shahar and Pieter, thank you for so many hours of data analysis, interpreting results, coding, writing and re-writing, and never forgetting to have fun during the process. Jelle, thank you for being there from day one. Thank you for all the hours of meditating about science and life, endless derivations, mentoring, and being a close friend. Läslo, thank you for giving me this great opportunity to learn, make mistakes, find my own way, and pursue my passion. Being driven from unique observations and seeking elegant and straightforward solutions are lifelong lessons. This is a dream-team.

During these four years, I had the chance to work with two more special people. I want to thank Dr. Yochai Ben-Horin from Soreq Nuclear Research Center, and Dr. Roger Waxler from the National Center for Physical Acoustics. Working with both of you was a unique learning experience; from looking at waveforms and explaining observations to blackboard math derivations, I enjoyed every moment and hope to keep working together in the future.

I wouldn't be able to survive these years without my mistress, climbing. I would like to thank the climbing gang Rutger, Meagan, Bart, Irma, Enzo, Sanne, Michiel, Sophia, Frank, Wieneke, Remmelt, Ivo, Sander, and Jolanda, for many many hours of climbing and fun. Special thanks to Bart and Rutger for many climbing trips to the magical forest. These short escapes from life made the last four years possible.

Finally, I would like to thank two families.
Amit, Tzlil, Shahar, Dana, and Camila. My alternative family. You made this place feel like home. You've all been there in hard and happy moments, always loving, willing to listen and give advise, laughing together while having a coffee or dinner, or just keeping company.
Mom, Dad, Or, Nir, and the Iuclas. My not-alternative family. This entire journey

wouldn't be possible without you. The Iuclas, thanks for all the love from across the sea, and the fun times during my visits and when you were here. Nir and Or, thanks for many fun and funny times. You are excellent brothers. Mom and Dad, thank you for always being there. Thanks you for listening, advising, supporting, laughing, and loving. I know that I never liked school as a kid, but thank you for pushing me to do my homework. I guess that it paid off.

To conclude this emotional part I would just say again, thank you.
I will miss all of you a lot.

Gil Averbuch,
Delft,
2019/20

Summary

Conversations between the Earth and the atmosphere: A study on the seismo-acoustic wavefield

The study of seismo-acoustic events is by no means new. Observations of earthquake-induced infrasound signals are dated back to the 1950s. However, the relative recent deployment of the International Monitoring System (IMS) by the Comprehensive Nuclear-Test-Ban Treaty Organization (CTBTO) provided world coverage for such signals. The continuous monitoring led to many detections of seismo-acoustic events and brought interest in this field back. Driven by unique and complex seismo-acoustic observations, this study uses array processing techniques to analyze the recorded data, back-projections to determine the origins of the infrasonic signals and numerical models to simulate infrasound wave propagation in coupled geophysical systems.

The North Korean underground nuclear tests in 2013, 2016, and 2017 generated atmospheric infrasound. Detections were made in the Russian Federation (I45RU) and Japan (I30JP) IMS microbarometers arrays. These detections formed the basis of the presented empirical studies on the seismo-acoustic wavefield. It is shown that atmospheric variability can explain only part of the observations; therefore, changes in the source characteristics must be considered. Moreover, back-projections show that infrasound radiation is not confined to the epicentral region. More distant regions are found to be consistent with locations of topography, sedimentary basins, and underwater evanescent sources.

A seismo-acoustic numerical model is used to simulate long-range infrasound propagation from underwater and underground sources. The Fast Field Program (FFP) is used to model the seismo-acoustic coupling between the solid Earth, the ocean, and the atmosphere under the variation of source and media parameters. A

thorough analysis of the seismo-acoustic coupling mechanisms reveals that evanescent wave coupling and leaky surface waves are the main energy contributors to long-range infrasound propagation. Moreover, it is found that source depth affects the relative amplitude of the tropospheric and stratospheric phases. This characteristic is further employed in an infrasound based inversion for the source parameters. A Bayesian inversion scheme is tested on synthetic data under the variations of the number of stations, the signals frequency band, and the signal-to-noise ratio (SNR). Also, an ensemble of realistic perturbed atmospheric profiles is used to investigate the effect of atmospheric uncertainties on the inversion results. Results show that variations in the number of stations, their positions, and SNRs, lead to source strength estimations with uncertainties up to 50%. However, all of the estimated depths were within a $\pm$100 m range from the original source depth.

Samenvatting

Titel in NL

Het bestuderen van seismo-akoestische gebeurtenissen is niet per definitie nieuw. De eerste meting van infrageluid van een aardbeving dateert uit de jaren vijftig van de vorige eeuw. Echter, met de komst van het alomvattende kernstopverdrag (Comprehensive Nuclear-Test-Ban Treaty) is er het wereldwijde Internationaal Monitoring Systeem (IMS) geplaatst en is er nu meer informatie over dit soort signalen. Het globaal en continue meten door het IMS heeft geleid tot meer detecties van seismo-akoestische signalen, wat heeft geresulteerd in meer interesse. Gedreven door deze unieke en complexe seismo-akoestische metingen wordt in deze thesis gebruik gemaakt van array processing technieken om de infrageluid metingen te analyseren, back-projections om de bron locatie te bepalen en numerieke modellen om te simuleren hoe infrageluid propageert en koppelt in geofysische systemen.

De door Noord Korea uitgevoerde ondergrondse nucleaire testen in 2013, 2016 en 2017 genereerde infrageluid dat door de atmosfeer propageerde. Deze signalen zijn opgevangen door de IMS microbarometer arrays in Rusland (I45RU) en Japan (I30JP). De detecties van beide stations vormen de basis van de gepresenteerde empirische onderzoeken naar het seismo-akoestisch golfveld. Het is aangetoond dat de variabiliteit in de atmosfeer maar delen van deze metingen kan verklaren; veranderingen van bron karakteristieken dienen ook onderzocht te worden. Back-projections van het gemeten signaal tonen aan dat de origine van het infrageluid niet alleen het epicentrum van de bron is. De back-projections wijzen op bron regios met veel topografie, sedimentaire bekkens en vanuit onderwater evanescent gekoppelde bronnen.

Om infrageluid propagatie, waarvan de bron onderwater of ondergronds is, over lange afstand te simuleren is er een seismo-akoestisch numeriek model ontwikkeld. Het Fast Field Program is gebruikt om de seismo-akoestische koppeling tussen de

ondergrond, de ocean en de atmosfeer te modelleren waarbij de bron en medium eigenschappen kunnen variëren. Uit grondige analyse van seismo-akoestische koppeling komt voort dat de evanescent golf koppeling en oppervlakte golven de twee grootste bronnen zijn van propagatie van infrageluid over lange afstanden. Daarnaast kwam voort uit de analyse dat de diepte van de bron de relatieve amplitude van de troposferische en stratosferische fases beïnvloedt. Deze eigenschap is verder uitgewerkt in een op infrageluid gebaseerde inversie van de bron eigenschappen. Een Bayesiaans inversie schema is getest met een variërende hoeveelheden sensoren, een variërende frequentie band van het signaal en een variërende signaal-ruis verhouding (SNR). Om te bepalen hoeveel invloed de atmosfeer heeft op de nauwkeurigheid van de inversie is een ensemble van realistische veranderingen van de atmosfeer gebruikt in het model. Uit de resultaten blijkt dat de variaties in hoeveelheid van sensoren, positie van de sensoren en de SNR resulteren in een bron sterkte met een 50% foutmarge. Echter is de geschatte diepte van de bron in de orde van $\pm$100m van de daadwerkelijke diepte.

Contents

1

Introduction: the seismo-acoustic wavefield

"It's always further than it looks. It's always taller than it looks. And it's always harder than it looks."

Reinhold Messner

Low-frequency acoustic waves, i.e., infrasound, propagate in the atmosphere, and have frequencies between 0.01 to 20 Hz. Infrasonic waves in the atmosphere may originate from sources in all geophysical media, such as the solid Earth, the oceans, and the atmosphere [*Campus and Christie*, 2009]. Examples of infrasound sources include underground explosions [*Assink et al.*, 2016], earthquakes in an Earth-atmosphere and an Earth-ocean-atmosphere system [*Benioff et al.*, 1951; *Evers et al.*, 2014], and volcanic eruptions both underwater and above ground [*Fee and Matoza*, 2013; *Green et al.*, 2013]. Due to the high impedance contrast, the Earth-atmosphere and ocean-atmosphere interfaces are usually treated as a free surface [*Aki and Richards*, 2002]. Nevertheless, infrasound generated by subsurface source has been observed.

An event is said to be seismo-acoustic if it generates elastic waves in the Earth and acoustic waves in the ocean and atmosphere. The elastic waves in the Earth are known as seismic waves. In the ocean and atmosphere, pressure waves are known as acoustic or sound waves. The typical low-frequency content of the observed atmospheric signals results in low-frequency sound waves that are known as infrasound. Due to atmospheric characteristics, which may result in waveguides, infrasonic waves can efficiently propagate over hundreds and thousands of kilometers, allowing to detect events in great distances from their origin. Besides of identifying events, detections of infrasound signals are used to retrieve characteristics of the

upper atmosphere, where few observations are available.

This study focuses on long-range infrasound propagation in Earth-atmosphere, ocean-atmosphere, and Earth-ocean-atmosphere systems. Since the coupling of acoustic waves from the Earth and ocean to the atmosphere is not trivial, an investigation of the coupling mechanisms that allow enhanced transmission and long-range atmospheric propagation is explored. Section 1.1 discusses the basic concepts of elastic and acoustic wave propagation in the Earth, ocean, and atmosphere. Derivation of the acoustic and elastic wave equations is presented in Sec. 1.2. A brief history review can be found in Sec. 1.3 I will conclude this introduction with the statement of research (Sec. 1.4), and an outline of the thesis (Sec. 1.5).

1.1 Wave propagation in the Earth, ocean, and atmosphere

Observations of infrasonic signals from underwater and underground sources are dated back to the 1950s and mainly deal with earthquake associated infrasound. *Benioff et al.* [1951] were the first to detect acoustic arrivals caused by an earthquake. Since then, various other studies have focused on the analysis of infrasound associated with earthquakes. Observations of infrasound signals from an underground source can be a result of long-range propagation and locally coupled waves. Observed long-range signals mean that the acoustic waves were coupled at a distance from the infrasound array. If the infrasound was coupled in the source epicenter, the signal is considered as epicentral infrasound, and it is attributed to the interaction of seismic waves with topographic features at the source region [*Mutschlecner and Whitaker*, 2005; *Green et al.*, 2009]. The efficient coupling can also occur remotely from the source epicenter in sedimentary basins and mountainous areas. This kind of signals is known as secondary infrasound [*Le Pichon et al.*, 2006; *Shani-Kadmiel et al.*, 2018]. Local infrasound is a signal that is locally induced by the passage of surface waves near the receiver.

Epicentral and secondary infrasound signals also exist in an Earth-ocean-atmosphere system. *Evers et al.* [2014] observed epicentral infrasound signals from the 2004 M_w 8.1 earthquake near the Macquarie oceanic Ridge. The earthquake generated seismic waves that were then coupled to hydroacoustic waves in the ocean and then to infrasound waves in the atmosphere. *Assink et al.* [2018] detected secondary infrasound signals from the 2017 North Korea underground nuclear test. Surface waves that were generated by the explosion propagated to the Japan basin, coupled to hydroacoustic waves, and then to infrasonic waves.

Wave propagation in each of the media depends on different parameters that define the existence of the waves, the propagation velocities, and amplitudes. Elastic waves in the Earth primarily depend on the density and elasticity of the medium. The elasticity is described by the stress-strain relationships, which is known as Hooke's law. Two essential parameters that arise in Hooke's law are the Lamé pa-

rameters λ and μ. These parameters describe the relationship between the medium density, compressional-wave velocity, and shear-wave velocity (through the bulk and shear modulus) [*Kausel*, 2006]. In the Earth, seismic waves are bounded between the increasing densities and velocities with depth and the Earth's surface (Figure 1.1). Depending on the seismic waves' properties, Earth's interface with the ocean and the atmosphere can be considered as free surface (total reflection) or continuous [*Aki and Richards*, 2002]. For instance, body waves from deep earthquakes will experience the Earth-atmosphere interface as a free surface, and reflect into the Earth. In contrast, surface waves that travel along the Earth-ocean interface emit acoustic waves into the ocean that can propagate over great distances [*Biot*, 1952].

The ocean acts as an acoustic waveguide bounded by the sea surface and the seafloor [*Ewing and Worzel*, 1948; *Munk*, 1974] . This waveguide allows for efficient propagation of sound for thousands of kilometers. Within the ocean column, the speed of sound depends on the temperature, salinity, and pressure [*Colosi*, 2016]. In high latitudes, the water column temperature is relatively uniform. Thus, the speed-of-sound profile is driven by the adiabatic gradient, which provides a constant increase in the speed of sound. In mid-latitudes, the speed of sound profile can be separated into two parts. First, at shallow depth, there is an increase of temperature toward the sea surface (thermocline), which leads to an increase in the speed of sound. Second, in lower depth, the speed of sound is controlled by the adiabatic gradient. Combining the two parts yields a minimum in the speed of sound profile around 1 km. This profile is known as the Munk profile [*Munk*, 1974], and it contains the Sound Fixing and Ranging channel (SOFAR channel) with its axis at a depth of one kilometer for the deep ocean (Figure 1.1).

In the atmosphere, the ideal gas law, $p = \rho RT$ relates pressure (p), density (ρ), and temperature (T), where R is is the specific gas constant. As sound propagation can be approximated as an adiabatic process (no heat flow), Laplace introduced the formulation

$$p = K\rho^{\gamma}. \tag{1.1.1}$$

Here, K is constant, and $\gamma = c_p/c_v$ is the ratio of the specific heat constants. For an adiabatic process, the entropy, s, is constant and the derivative of the pressure with respect to density lead to the relation

$$\left.\frac{\partial p}{\partial \rho}\right|_S = \gamma K \rho^{\gamma-1} = \gamma RT = \tilde{c}^2, \tag{1.1.2}$$

where $\tilde{c}$ is the speed of sound in the presence of sound. Since the atmosphere is a moving medium (winds), and the wind velocity can be within the same order of magnitude as the adiabatic speed of sound, its effect must be considered; the atmospheric waveguides depends on both winds and adiabatic speed of sound. It can either be introduced as a variable in the wave equation for moving medium [*Brekhovskikh and Godin*, 1999; *Ostashev et al.*, 2015; *Pierce*, 2019](Section 1.2) or be combined with the adiabatic speed of sound [*Godin*, 2002; *Waxler*, 2004]. Combining the adiabatic speed of sound and the horizontal winds yield the effective speed

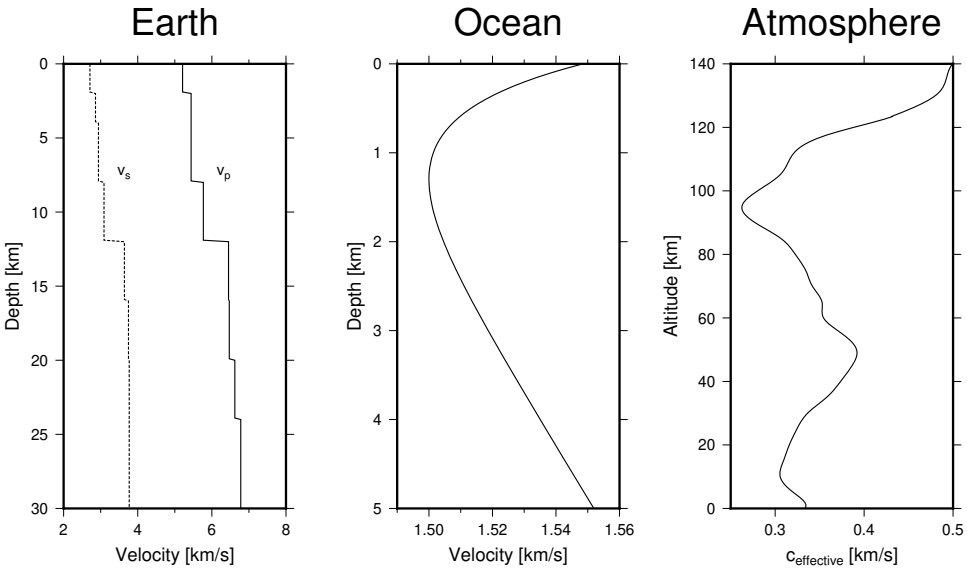

Figure 1.1: *Seismic and acoustic velocity profiles in the Earth, ocean, and atmosphere. The profiles in the Earth represent pressure (v_p) and shear (v_s) velocity profiles for the first 30 km at Haiti [Possee et al., 2019]. The oceanic profile is a standard Munk profile with a minimum at a depth of 1 km. This minimum represents the axis of the SOFAR channel. The atmospheric effective speed of sound profile is calculated for eastward propagation on January 10^{th}, 2017, which is further specified in Figure 1.2.*

of sound.

Unlike the Earth and the ocean, the atmosphere is a rapidly changing medium. From seasonal to diurnal changes, monitoring the variability of the atmosphere is a key element in understanding infrasound observations. On the other hand, infrasound monitoring can be used to probe the atmosphere [*Smets and Evers*, 2014; *Fricke et al.*, 2014]. Figure 1.2 shows an example of summer and winter atmospheric climatologies from HWM14 [*Drob et al.*, 2015] and MSIS-00 [*Picone et al.*, 2002] empirical models. The troposphere is the lowest atmospheric layer, and a decrease in the temperature characterizes it. An inversion of the temperature profile marks the top of the troposphere, and it is also the location of the eastward tropospheric jet stream. A constant increase in temperature between 12 to 55 km represents the stratosphere. At the top of the stratosphere, the stratospheric circumpolar vortex can reach velocities exceeding 100 m/s. It typically flows eastward in the winter, and westward in the summer. However, during wintertime, strong disturbances in the troposphere-stratosphere boundary can lead to a shift in the jet direction [*Smets and Evers*, 2014]. Depending on the direction of propagation, the combination of the adiabatic speed of sound and winds, i.e., the effective speed of sound, may or may

not form the atmospheric waveguides. For instance, for an eastward propagation, the eastward tropospheric jet stream forms the tropospheric waveguide, providing ideal propagation conditions. In contrast, during winter, westward propagation will experience unfavored propagation conditions in the stratosphere.

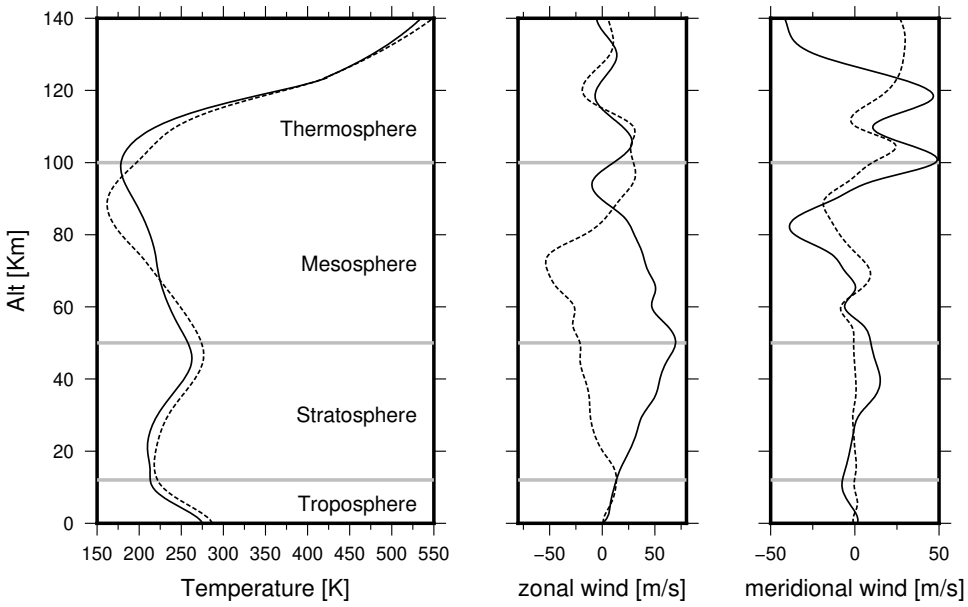

Figure 1.2: *Temperature, zonal wind , and meridional wind on January 10^{th}, 2017 (solid lines) and July 10^{th}, 2017 (dashed lines) at $50°N$ $50°W$. The gray horizontal lines represent the approximated boundaries of the tropopause, stratopause, and mesopause.*

The distinct decrease in temperature above the stratosphere represents the mesosphere. An increase in temperature bounds the mesosphere and marks the lower boundary of the thermosphere. This rapid increase in temperature with altitude forms the thermospheric waveguide. Due to the thermosphere's low density, acoustic waves experience high damping. Therefore, the longer infrasound travels through the thermosphere, the higher the damping will be. Semi-diurnal solar tides enhance detections of thermospheric returns. These tides lead to variations in the mesopause altitude and therefore in the thermosphere return height. When return heights are low, there is less damping, and more energy propagates over long distances [*Averbuch et al.*, 2019].

The effective speed of sound defines the trace velocities (horizontal phase velocity) that can propagate in the atmosphere (Figure 1.1). For an atmospheric point

source, the trace velocities of the propagating waves will be bounded by the minimum and maximum effective speed of sound. Waves with lower trace velocities will be evanescent (Chapter 1.2), and decay. Waves with higher trace velocities will propagate steeply upwards and not get trapped in the atmospheric waveguides. In case of a subsurface source, the characteristics of the waves trace velocities in the atmosphere also depend on the source parameters and coupling mechanisms. Radiation from a subsurface source into the atmosphere is not homogeneous; waves with different trace velocities will have different amplitudes [*Godin*, 2006, 2011]. Therefore, although the atmosphere allows a range of propagating waves, not all of them will propagate and be observed.

1.2 Wave propagation theory

Acoustic waves are small perturbations of the background state of pressure, density, and particle velocity. To describe the propagation of acoustic waves in a moving medium, such as the atmosphere, we must consider three equations: momentum equation (1.2.1a), continuity equation (1.2.1b), and an equation of state (1.2.1c).

$$\rho\left(\frac{\partial \boldsymbol{v}}{\partial t} + (\boldsymbol{v}\cdot\nabla)\boldsymbol{v}\right) = -\nabla p - \rho g\hat{z} \tag{1.2.1a}$$

$$\frac{\partial \rho}{\partial t} + \nabla\cdot(\rho\boldsymbol{v}) = 0 \tag{1.2.1b}$$

$$p = p(\rho, S), \tag{1.2.1c}$$

where p, ρ, and $\boldsymbol{v}$ are pressure, density, and velocity, respectively. In equation (1.2.1a) g is the gravity constant, and in equation (1.2.1c), S is the total entropy, and is assumed to be constant. Let us define p, ρ, and $\boldsymbol{v}$ as

$$p = p_0 + p' \quad \rho = \rho_0 + \rho' \quad \boldsymbol{v} = \boldsymbol{v}_0 + \boldsymbol{v}'. \tag{1.2.2}$$

Here, subscript 0 corresponds to the background state, and the prime denotes the perturbation.

Following the derivation by *Brekhovskikh and Godin* [1990], in order to derive the linearized wave equation for infrasound propagation in the atmosphere we will take several assumptions. (1) The perturbed quantities are much smaller than the background state. (2) In the atmosphere, vertical winds are considered to be much weaker than horizontal winds. Therefore, the vertical winds will be neglected and the wind will be defined as $\boldsymbol{v}_0 = (\boldsymbol{v}_{0H}, 0)$, where $\boldsymbol{v}_{0H}$ is the horizontal wind component. (3) The acoustic propagation is assumed to be an adiabatic process in a lossless atmosphere, which means that the viscosity is zero. (4) The background state depends only on the vertical axis, i.e., neglecting horizontal variations.

Expending the right hand side of equation (1.2.1a) provides

$$\rho\left(\frac{\partial \boldsymbol{v}}{\partial t} + (\boldsymbol{v}\cdot\nabla)\boldsymbol{v}\right) = -\nabla p_0 - \nabla p' - \rho_0 g\hat{z} - \rho' g\hat{z}. \tag{1.2.3}$$

Due to the vertical dependency of the background state, the arguments $(\boldsymbol{v}_0 \cdot \nabla)\boldsymbol{v}_0$ is equal to zero, and the remaining zero order terms gives $dp_0/dz = -\rho_0 g\hat{z}$, which is the hydrostatic pressure. For infrasonic frequencies, gravity effects can be neglected, i.e., neglecting $\rho' g\hat{z}$. Now, keeping only first order terms, equation (1.2.3) will take the following form

$$\frac{d\boldsymbol{v}'}{dt} + (\boldsymbol{v}' \cdot \nabla)\boldsymbol{v}_0 = -\frac{1}{\rho_0}\nabla p'. \tag{1.2.4}$$

Here, $d/dt = \partial/\partial t + \boldsymbol{v}_0 \cdot \nabla$ is the material derivative, and $(\boldsymbol{v}' \cdot \nabla)\boldsymbol{v}_0 = v'_z d\boldsymbol{v}_{0H}/dz$, which is the wind-shear term.

A useful form of equation (1.2.1c) (equation of state), can be derived based on the entropy equation [*Blackstock*, 2000]

$$\rho T\frac{dS}{dt} = \aleph^{\text{visc}} + \kappa\nabla^2 T, \tag{1.2.5}$$

where $\aleph^{\text{visc}}$ represents the viscous energy dissipation, and κ is the thermal conduction coefficient. Since we assume an adiabatic process and a lossless atmosphere, the right hand side can be neglected, and equation (1.2.5) becomes

$$\frac{dS}{dt} = 0. \tag{1.2.6}$$

Following *Wilson* [1957], an increment of the entropy can be expressed as

$$dS = c_p\frac{dT}{T} - R\frac{dp}{p}. \tag{1.2.7}$$

Integrating equation (1.2.7), and combining with equations (1.1.1), (1.1.2), and (1.2.6) yields the following equation of state

$$\left(\frac{\partial}{\partial t} + \boldsymbol{v} \cdot \nabla\right)p = \tilde{c}^2\left(\frac{\partial}{\partial t} + \boldsymbol{v} \cdot \nabla\right)\rho = 0. \tag{1.2.8}$$

The coefficient $\tilde{c}^2 = c^2 + c'^2$ represents the speed of sound. Let us write equation (1.2.1b) as

$$\left(\frac{\partial}{\partial t} + \boldsymbol{v} \cdot \nabla\right)\rho + \rho\nabla \cdot \boldsymbol{v} = 0. \tag{1.2.9}$$

Combining equations (1.2.9) and (1.2.8) yields

$$\frac{1}{\tilde{c}^2}\left(\frac{\partial}{\partial t} + \boldsymbol{v} \cdot \nabla\right)p + \rho\nabla \cdot \boldsymbol{v} = 0. \tag{1.2.10}$$

As before, keeping first order terms and noting that $(\boldsymbol{v}_0 \cdot \nabla)p_0 = 0$, we obtain

$$\frac{1}{c^2}\frac{dp'}{dt} + \rho_0\nabla \cdot \boldsymbol{v}' = 0. \tag{1.2.11}$$

The remaining zero-order argument satisfies $\rho_0 \nabla \cdot \boldsymbol{v}_0 = 0$.

Taking the divergence of equation (1.2.4), the material derivative of equation (1.2.11), and subtract the first from the last leads to

$$\frac{d}{dt}\left(\frac{1}{\rho_0 c^2}\frac{dp'}{dt}\right) + \frac{d}{dt}\nabla \cdot \boldsymbol{v}' - \nabla \cdot \frac{d\boldsymbol{v}'}{dt} - \frac{d\boldsymbol{v}_{0H}}{dz} \cdot \nabla v_z' - \nabla \cdot \left(\frac{1}{\rho_0}\nabla p'\right) = 0. \quad (1.2.12)$$

One can show that

$$\frac{d}{dt}\nabla \cdot \boldsymbol{v}' - \nabla \cdot \frac{d\boldsymbol{v}'}{dt} = -\frac{d\boldsymbol{v}_{0H}}{dz} \cdot \nabla v_z', \quad (1.2.13)$$

and equation (1.2.12) can be written as

$$\frac{d}{dt}\left(\frac{1}{\rho_0 c^2}\frac{dp'}{dt}\right) - 2\frac{d\boldsymbol{v}_{0H}}{dz} \cdot \nabla v_z' - \nabla \cdot \left(\frac{1}{\rho_0}\nabla p'\right) = 0. \quad (1.2.14)$$

To arrive in a closed form of equation (1.2.14), we will take its material derivative and express dv_z'/dt using equation (1.2.4). The result will be the acoustic wave equation in a moving layered media

$$\frac{d}{dt}\left[\frac{d}{dt}\left(\frac{1}{\rho_0 c^2}\frac{dp'}{dt}\right) - \nabla \cdot \left(\frac{1}{\rho_0}\nabla p'\right)\right] + 2\left(\frac{d\boldsymbol{v}_{0H}}{dz} \cdot \nabla\right)\left(\frac{1}{\rho_0}\frac{\partial p'}{\partial z}\right) = 0. \quad (1.2.15)$$

The term $d\boldsymbol{v}_{0H}/dz$ represents the effect of wind-shear on the acoustic propagation. For infrasonic frequencies, wind-shear is negligible. Hence, neglecting the wind-shear term from equation (1.2.15) yields the infrasound wave equation in a moving layered media:

$$\frac{1}{c^2}\frac{d^2 p'}{dt^2} - \rho_0 \nabla \cdot \left(\frac{1}{\rho_0}\nabla p'\right) = 0. \quad (1.2.16)$$

Defining ∇_H as the horizontal gradient, equation (1.2.16) can be written as

$$\frac{1}{c^2}\left(\frac{\partial}{\partial t} + \boldsymbol{v}_{0H} \cdot \nabla_H\right)^2 p' - \nabla_H^2 p' - \rho_0 \frac{\partial}{\partial z}\left(\frac{1}{\rho_0}\frac{\partial p'}{\partial z}\right) = 0. \quad (1.2.17)$$

In the frequency-(horizontal)wavenumber domain, the operator $(\partial/\partial t + \boldsymbol{v}_{0H} \cdot \nabla_H)^2/c^2$ can be written as $(i\omega - i\boldsymbol{k}_H \cdot \boldsymbol{v}_{0H})^2/c^2$. Approximating $\boldsymbol{k}_H \approx \omega \hat{k}_H/c$, where $\hat{k}_H$ is the horizontal direction of propagation, the operator can be approximated by

$$\frac{i\omega}{c}\left(1 - \frac{\boldsymbol{v}_{0H} \cdot \hat{k}_H}{c}\right) = \frac{i\omega}{c}\left(\frac{1}{1 + \frac{\boldsymbol{v}_{0H} \cdot \hat{k}_H}{c}}\right) + \mathcal{O}(M^2) + ... \approx \frac{i\omega}{c + \boldsymbol{v}_{0H} \cdot \hat{k}_H} \equiv \frac{i\omega}{c_{\text{eff}}}, \quad (1.2.18)$$

where $c_{\text{eff}} = c + \boldsymbol{v}_{0H} \cdot \hat{k}_H$. The approximation of the effective speed of sound, c_{eff}, may overestimate the effects of the winds on the propagation. Therefore, this approximation holds for (1) small vertical propagation angles (2) in-plane propagation, and (3) low Mach number, $\mathrm{M} = |\boldsymbol{v}_{0H}|/c$ [*Godin*, 2002; *Waxler*, 2004].

Plugging equation. (1.2.18) into the the frequency domain form of equation. (1.2.17) yields

$$k_{z,\text{eff}}^2 p + \rho_0 \frac{\partial}{\partial z}\left(\frac{1}{\rho_0}\frac{\partial p}{\partial z}\right) = 0, \tag{1.2.19}$$

where the vertical wavenumber is defined as $k_{z,\text{eff}} = \sqrt{k_{\text{eff}}^2 - k_H^2}$, and $k_{\text{eff}} = \omega/c_{\text{eff}}$. This form of the infrasound wave equation is used for the seismo-acoustic wave propgation modeling that is presented in Chapters 3 and 4. In the case of a dissipative atmosphere, absorption is frequency-dependent, and the winds can cause a Doppler shift to the waves' frequencies. Nevertheless, this effect is small for infrasonic frequencies [*Waxler et al.*, 2017a].

Solutions to the presented wave equations have a general form of a sinusoidal time-harmonic $p(\boldsymbol{x}, t) = Ae^{i(\boldsymbol{k}\cdot\boldsymbol{x}-\omega t)}$, where A is the amplitude, $\boldsymbol{x}$ is a three dimensional position vector in the euclidean space, $\boldsymbol{k}$ is the three dimensional wavenumber vector, and ω is a constant angular frequency. The medium wavenumber is defined as $k = \omega/c$, and the wavenumber vector components must satisfy the relation $k^2 = k_x^2 + k_y^2 + k_z^2$. The magnitude of the components defines the direction of the propagating wave as well as its nature. For example, if all of the wavenumber components are real, the propagating wave is said to be homogeneous. On the contrary, if one of the wavenumber components is imaginary, the wave is considered as inhomogeneous (also known as evanescent). Such waves decay exponentially along the axis of the imaginary wavenumber [*Caviglia and Morro*, 1992].

Deriving the wave equation for ocean acoustics is similar to the derivation of the infrasound wave equation. As in the atmosphere, the speed of sound in the ocean is related to the density and compressibility. The density in the ocean depends on the temperature, salinity, and hydrostatic pressure. Usually, the oceanic speed of sound profile is computed by empirical functions that are based on these parameters [*Brekhovskikh and Lysanov*, 1982]. Since the oceanic speed of sound (approximately 1500 m/s) is much higher than the ocean currents (several meters per second), the ocean flow can be neglected and the medium is considered at rest for acoustic propagation. The acoustic wave equation for oceanic propagation can be obtained by setting the wind components, in the previous derivation, to zero.

Modeling the elastic wavefield requires solving the elastic wave equation. Let us write another form of the momentum equation. Here, we will assume a medium at rest, and allow forces to act from any orientation as opposed to only normal forces allowed in the fluid case. By doing that, both compressional and shear components are taken into account. The linearized momentum equation for solids reads [*Wapenaar and Berkhout*, 1989]

$$\rho_0 \frac{\partial \boldsymbol{v}}{\partial t} - \nabla \cdot \boldsymbol{\sigma} = 0, . \tag{1.2.22}$$

Here $\boldsymbol{\sigma} = \sigma_{ij}$ represents the stresses on an elastic element due to small deformations, and $i, j = x, y, z$. By choosing the medium to be shear-stress-free, the off-diagonal

Homogeneous and inhomogeneous body waves are solutions of the wave equation, and they are defined by the wavenumber components. Let us assume a general solution of the wave equation in the form of $\Phi(\boldsymbol{x}, t) = Ae^{i(\boldsymbol{kx}-\omega t)}$.

Homogeneous wave: $\boldsymbol{k}$ is real, and the disturbance propagates in a phase speed of $c_{phase} = \omega/|\boldsymbol{k}|$. In that case the phase speed and the medium velocity are equal, i.e. $c = c_{phase}$. it means that planes of constant phase correspond to planes with constant amplitude.

Inhomogeneous (evanescent) wave: $\boldsymbol{k}$ has an imaginary component and is defined as $\boldsymbol{k} = \boldsymbol{k}_{\mathrm{H}} + i\boldsymbol{k}_{\mathrm{V}}$. Substituting it to the general solution yields $\Phi(\boldsymbol{x}, t) = Ae^{-\boldsymbol{k}_{\mathrm{V}}\boldsymbol{x}}e^{i(\boldsymbol{k}_{\mathrm{H}}\boldsymbol{x}-\omega t)}$. Clearly, the first exponent is real, and represents a decaying amplitude that depends on the wave vertical position. The real part of the wavenumber, $\boldsymbol{k}_{\mathrm{H}}$, defines the wave phase speed as $c_{phase} = \omega/|\boldsymbol{k}_{\mathbf{H}}|$. For these wavenumber characteristics, the phase speed is lower than the medium velocity, and planes with constant phase (horizontal axis) and amplitudes (vertical axis) do not correspond to each other. For a lossless medium, these components must be perpendicular to each other. However, when the medium is dissipative, they do not have to be perpendicular.

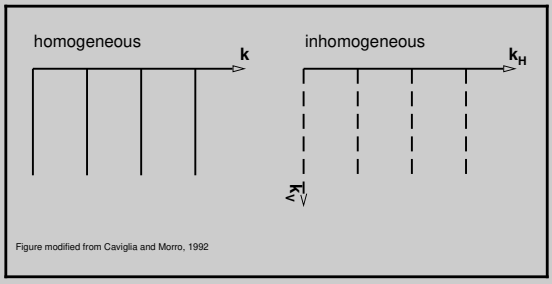

Figure modified from Caviglia and Morro, 1992

Snell's law implies that the wave's horizontal component does not change when crossing an interface. Therefore, a wave can be homogeneous in one medium and become inhomogeneous when crossing to another, and vice versa. Defining the horizontal phase velocity as trace velocity, this can be further seen in

$$k_{z1,2} = \omega\sqrt{\frac{1}{c_{1,2}^2} - \frac{1}{c_{\mathrm{trace}}^2}}.$$

Given a wave that travels from medium 1 to 2, if $c_1 < c_2 < c_{trace}$, the wave is homogeneous in both media. If $c_1 < c_{\mathrm{trace}} < c_2$, the wave is homogeneous in medium 1 and inhomogeneous in medium 2. If $c_{\mathrm{trace}} < c_1 < c_2$, the wave is inhomogeneous in both media.

Infrasound wave equation for reduced pressure: Our starting point for this derivation is equation (1.2.15). Noting that $d/dt = (i\omega - i\boldsymbol{k}_H \cdot \boldsymbol{v}_{0H})$, and defining $\beta = 1 - \boldsymbol{k}_H \cdot \boldsymbol{v}_{0H}/\omega$, equation (1.2.15) takes the form

$$\left(k^2\beta^2 - k_H^2\right)p' + \rho_0\beta^2\frac{\partial}{\partial z}\left(\frac{1}{\rho_0\beta^2}\frac{\partial p'}{\partial z}\right) = 0, \tag{1.2.20}$$

which preserves the wind-shear term. See Appendix A.1 for a detailed derivation.
The reduced pressure is defined as $\tilde{p} = p/\sqrt{\rho_0}\beta$. Substituting it in the previous equation yields

$$\frac{\partial^2\tilde{p}}{\partial z^2} + \left[(k^2\beta^2 - k_H^2) + \frac{1}{2\rho_0\beta^2}\frac{\partial^2(\rho_0\beta^2)}{\partial z^2} - \frac{3}{4}\left(\frac{1}{\rho_0\beta^2}\frac{\partial(\rho_0\beta^2)}{\partial z}\right)^2\right]\tilde{p} = 0. \tag{1.2.21}$$

For infrasonic frequencies above 0.05Hz, the second-order derivative and the square of the first-order derivative of $\rho_0\beta^2$ are negligible [*Assink et al.*, 2017]. Omitting them provides the Helmholtz equation for the reduced pressure.

entries will be zero and the diagonal elements will relate to the pressure by $p = -\sigma_{ii}$. A complementary constitutive equation (an equivalent to the equation of state) is the stress-strain relation which is also known as Hooke's law. For isotropic media, Hooke's law can be written as

$$\boldsymbol{\sigma} = \lambda tr(\boldsymbol{\epsilon})I + 2\mu\boldsymbol{\epsilon}; \quad \boldsymbol{\epsilon} = \frac{1}{2}\left(\nabla\boldsymbol{u} + (\nabla\boldsymbol{u})^T\right), \tag{1.2.23}$$

where I is an identity matrix, $\boldsymbol{\epsilon}$ is the strain, and $tr(\boldsymbol{\epsilon})$ is the trace of the strain tensor. Replacing the particle velocity by the particle displacement according to $\boldsymbol{v} = \partial\boldsymbol{u}/\partial t$ yields the elastic wave equation

$$\rho_0\frac{\partial^2\boldsymbol{u}}{\partial t^2} - \nabla\cdot\boldsymbol{\sigma} = 0. \tag{1.2.24}$$

Solutions for equation 1.2.24 consist of pressure and shear body waves that can be both homogeneous and inhomogeneous. Moreover, linear combinations of elastic inhomogeneous body waves that travel along interfaces give rise to different types of surface waves. Lord Rayleigh was the first to define elastic surface wave that travels along the free-surface of an elastic half-space [*Rayleigh*, 1885]. In a coupled elastic-acoustic system, combining these solutions with homogeneous or inhomogeneous acoustic waves in the acoustic half-space give rise to leaky Rayleigh or Scholte waves, respectively [*Bromwich*, 1898; *Scholte*, 1947; *Biot*, 1952]. Similarly, an interface wave that propagates along an elastic-elastic interface is known as Stoneley wave, and it is defined by a linear combination of inhomogeneous elastic waves in both sides of the interface [*Stoneley*, 1926].

In Chapter 3, we will show that solutions in the form of inhomogeneous body waves and surface waves play an essential role in long-range infrasound propagation from subsurface sources. Due to the lower acoustic propagation velocity in the atmosphere, the coupled waves become propagating. Since the spectrum of the coupled evanescent waves consists of large horizontal wavenumbers, the waves can get trapped in the atmospheric waveguides and propagate over large distances (Figure 1.3, 2^{nd} type). The contribution of air-coupled surface waves to long-range infrasound propagation (Figure 1.3, 3^{rd} type) depends on the surface wave trace velocity. For high trace velocities, the coupled waves will propagate upwards, and as the trace velocity decreases, the horizontal component of the coupled wave increases. If the surface wave trace velocity is in the order of the effective speed of sound, the coupled waves can get trapped in the atmospheric waveguides.

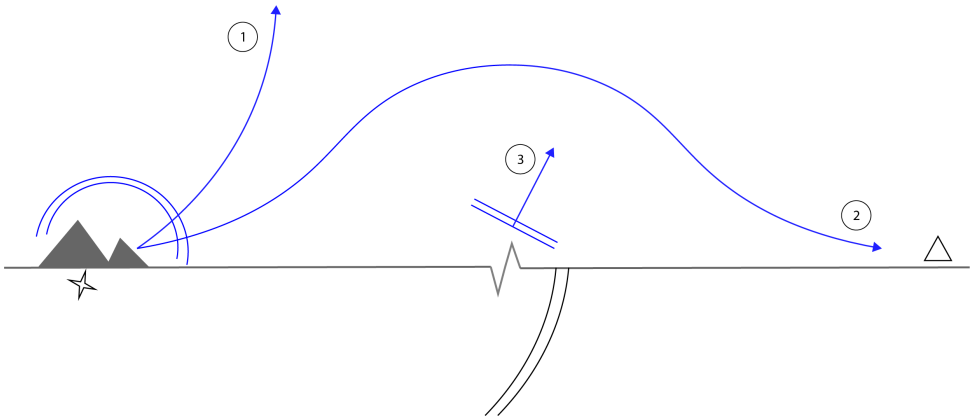

Figure 1.3: *Atmospheric propagation from the three Earth-atmosphere coupling mechanisms. (1) propagation from homogeneous body waves. These waves are characterized by high trace velocities, leading to almost vertical propagation in the atmosphere. (2) propagation from inhomogeneous body waves. Due to the low trace–velocity content, these waves have a large horizontal component, and (3) propagation from surface waves. The direction of the propagating wave depends on the surface-wave trace velocity.*

1.3 A brief history

Sources of seismic energy in the subsurface can generate low-frequency acoustic waves in the atmosphere, i.e., infrasound. There are various mechanisms through which seismic waves in the subsurface can be coupled to infrasonic waves in the atmosphere, at the lithosphere-atmosphere interface. Previous studies with earthquake recordings have shown: (1) epicentral infrasound, (2) topographical infrasound, and

(3) evanescently coupled infrasound. *Benioff et al.* [1951] were the first to detect acoustic arrivals caused by an earthquake of unknown magnitude at a distance of 265 km. Following that, infrasonic observations of the 1964 M_w 9 Alaska earthquake have been studied in detail and have been associated with epicentral infrasound [*Bolt*, 1964; *Donn and Posmentier*, 1964; *Mikumo*, 1968] as well as secondary radiation from mountain ranges [*Young and Greene*, 1982]. Since the 1960s, various other studies have focused on the analysis of infrasound associated with earthquakes. Usually, such signals are assigned to the interaction of seismic body waves and surface waves with topographic features at the epicentral region [*Mutschlecner and Whitaker*, 2005; *Watada et al.*, 2006; *Mikumo et al.*, 2008; *Green et al.*, 2009]. However, efficient coupling also occurs remotely from the source epicenter in sedimentary basins and mountainous areas [*Le Pichon et al.*, 2006; *Marchetti et al.*, 2016; *Shani-Kadmiel et al.*, 2018]. The detection of these signals was dependent on the ground-to-air coupling and atmospheric propagation conditions to a distant array [*Shani-Kadmiel et al.*, 2018]. While the ability to detect seismo-acoustic signals and distinguish between the infrasonic phases has improved, associating them with the seismic wavefield and quantifying the contribution of the coupling mechanisms to the perturbed wavefield in the atmosphere is still an open question.

Investigating the acoustic and seismic response to a different type of sources has been the focus of many experimental, analytical, and numerical studies. For example, Lord Rayleigh, Stoneley [*Rayleigh*, 1885], Scholte [*Scholte*, 1947], and Biot [*Biot*, 1952] developed exact representations of both acoustic and seismic responses for simplified elastic and acoustic models. *Godin* [2006] and *McDonald and Calvo* [2007] solved the problem for two half-spaces with stark density and velocity contrast. For more complex media, numerical methods provide different solutions to the acoustic and elastic linear wave equations. Solutions of the time-space and frequency-space forms of the wave equation are commonly obtained by using finite-difference [*Kelly and Ward*, 1976; *Tappert*, 1977], spectral methods [*Kosloff et al.*, 1990], finite elements [*Komatitsch and Tromp*, 1999] and ray methods [*Virieux*, 1986; *Cerveny*, 2001]. Modeling wave propagation in layered media with smooth lateral variations, like the ocean, is usually done by using normal modes [*Pekeris*, 1939] and parabolic-equation [*Tappert*, 1977] methods for solving the frequency-wavenumber (f-k) wave equation.

Infrasonic waves can be simulated with all of the mentioned methods; some of them are finite-difference in the space-time domain [*de GrootHedlin*, 2008], ray methods [*Dessa et al.*, 2005; *Smets and Evers*, 2014], and normal modes [*Waxler*, 2004; *Waxler et al.*, 2017a]. Coupled seismo-acoustics models have been developed over the years with a center of attention on Earth-ocean models. The Fast Field Program (FFP) is used to solve the problem for a layered coupled system in the f-k domain [*Schmidt and Tango*, 1986], and the spectral elements SPECFEM provide solutions to a more complex setups [*Komatitsch et al.*, 2000]. However, very little attention was given to a coupled ocean-atmosphere and Earth-atmosphere systems. To the best of my knowledge, only *Mikhailenko and Mikhailov* [2014] and *Martire*

et al. [2018] solved the problem for infrasonic waves induced by an underground source. However, both studies were focused on short range propagation and there was lack of analysis of the coupling mechanisms. Therefore, the understanding of how the different waves are coupled to the atmosphere, what is the impact of the source parameters and medium, and what are the topographic effects on the coupled energy still need to be investigated.

1.4 Statement of research

Following Chapter 1.3, this thesis focuses on the study of the seismo-acoustic wavefield from both observational and theoretical points of view. Particular attention is given to long-range infrasound propagation from underground sources. Seismic and infrasonic waves are complementary and occur along different propagation paths of the seismo-acoustic wavefield produced by an event. Thus, the observable seismic and acoustic signals are independent and enable improving the event detection, and the source characterization. Studying the seismo-acoustic coupling mechanisms and their effect on long-range infrasound propagation is essential in understanding previous observations like the North Korea underground nuclear tests [*Assink et al.*, 2016, 2018], and earthquake-induced infrasound [*Evers et al.*, 2014; *Shani-Kadmiel et al.*, 2018] , as well as future observations. Moreover, the growing interest in compiling seismic and infrasonic observations to provide more insights into the locations and mechanisms of the sources is based on a fundamental comprehension of the coupling processes.

In the upcoming chapters the following questions will be addressed:

- What part of the subsurface wavefield spectrum contributes to long-range infrasound propagation?
- What is the effect of the source parameters, and medium properties on the amplitudes of the coupled waves and the observable signals?
- Can infrasound observations be used to extract subsurface source characteristics?

1.5 Outline

The disseration is organized as follows. Chapter 2 describes the observations of three DPRK's underground nuclear tests. It contains the first attempt to estimate an underground source depth from long-range infrasound observations, as well as analyzing the complex seismo-acoustic wavefield. It shows both epicentral and secondary infrasound that was coupled in an earth-atmosphere and earth-ocean-atmosphere systems. Chapter 3 is a detailed numerical analysis of the coupling mechanisms in a ocean-atmosphere and Earth-atmosphere system. The FFP is used to model the seismo-acoustic coupling between the solid Earth, the ocean, and the atmosphere

under the variation of source and media parameters. Chapter 4 is a theoretical study that shows the prospect of infrasound based inversion, which extracts the subsurface source's absolute depth and strength. Moreover, an ensemble of realistic perturbed atmospheric profiles is used to investigate the effect of atmospheric uncertainties on the inversion results. Chapter 5 concludes the dissertation with conclusions, recommendations and outlook.

Rayleigh wave is an elastic surface wave that travels along the free surface of an elastic half space. To describe a Rayleigh wave in a xz plane, the displacement field will be represented in terms of compressional and shear potentials according to $\boldsymbol{u} = \nabla\Phi + \nabla \times \boldsymbol{\Psi}$. The compressional potential is $\Phi(\boldsymbol{x}, t) = Ae^{-k_z z}e^{i(k_x x - \omega t)}$, and the shear potential is represented by $\Psi(\boldsymbol{x}, t) = Be^{-\tilde{k}_z z}e^{i(k_x x - \omega t)}$. Substituting the potentials into the Helmholtz equation yield the relations between the surface wave trace velocity to the medium compressional wave velocity, v_p, and shear wave velocity, v_s.

$$[\nabla^2 + k_p^2]\Phi(r, z) = 0 \;\rightarrow\; k_p^2 + k_z^2 - k_x^2 = 0 \;\rightarrow\; k_z = \omega\sqrt{\frac{1}{c_{\text{trace}}^2} - \frac{1}{v_p^2}},$$

$$[\nabla^2 + k_s^2]\Psi(r, z) = 0 \;\rightarrow\; k_s^2 + \tilde{k}_z^2 - k_x^2 = 0 \;\rightarrow\; \tilde{k}_z = \omega\sqrt{\frac{1}{c_{\text{trace}}^2} - \frac{1}{v_s^2}}.$$

Since both k_z and $\tilde{k}_z$ are real numbers, the terms in the square roots need to be positive. Therefore, we can deduce that $c_{\text{trace}} < v_s < v_p$. A free-surface boundary conditions states that the normal and tangential stresses equal to zero. Substituting the potentials into Hooke's law at $z = 0$ yields the equations

$$\begin{aligned}(2\mu k_z^2 - \lambda k_p^2)A - ik_x\tilde{k}_z B = 0\\ -2ik_x k_z A - (k_x^2 + \tilde{k}_z^2)B = 0.\end{aligned}$$

We can rewrite this set in the form of

$$\begin{aligned}\Big(2 - \frac{k_s^2}{k_x^2}\Big)A - 2i\Big(1 - \frac{k_s^2}{k_x^2}\Big)^{\frac{1}{2}}B = 0\\ 2i\Big(1 - \frac{k_p^2}{k_x^2}\Big)^{\frac{1}{2}}A + (2 - \frac{k_s^2}{k_x^2}\Big)B = 0.\end{aligned}$$

A particular solution exists if the determinant is equal to zero. The determinant yields the equation

$$\Big(2 - \frac{k_s^2}{k_x^2}\Big)^2 = 16\Big(1 - \frac{k_s^2}{k_x^2}\Big)^{\frac{1}{2}}\Big(1 - \frac{k_p^2}{k_x^2}\Big)^{\frac{1}{2}}.$$

It can also be written as

$$\Big(2 - \frac{c_{\text{trace}}^2}{v_s^2}\Big)^2 = 16\Big(1 - \frac{c_{\text{trace}}^2}{vs^2}\Big)^{\frac{1}{2}}\Big(1 - \frac{c_{\text{trace}}^2}{v_p^2}\Big)^{\frac{1}{2}}.$$

Discarding the obvious solution $c_{\text{trace}} = 0$, since the left hand side of the equation is squared, it has to be positive. From that we can conclude that the arguments in the right hand side must be positive too. Therefore, the surface wave trace velocity is bounded between zero and the shear wave velocity $0 < c_{\text{trace}} < v_s$.

2

Detection of infrasonic signals from the DPRK's underground nuclear tests

"Experience without theory is blind, but theory without experience is mere intellectual play."

Immanuel Kant

2.1 On the infrasound detected from the 2013 and 2016 DPRKs underground nuclear tests

Abstract The underground nuclear tests by the Democratic People's Republic of Korea (DPRK) generated atmospheric infrasound, both in 2013 and 2016. Clear detections were made in the Russian Federation (I45RU) and Japan (I30JP) in 2013 at stations from the International Monitoring System. Both tropospheric and stratospheric refractions arrived at the stations. In 2016, only a weak return was potentially observed at I45RU. Data analysis and propagation modeling shows that the noise level at the stations and the stratospheric circumpolar vortex were different in 2016 compared to 2013. As the seismic magnitude of the 2013 and 2016 nuclear test explosions was comparable, we hypothesize that the 2016 test occurred 1.5 times deeper. In such a case, less seismic energy would couple through the lithosphere-atmosphere interface, leading to less observable infrasound. Since explosion depth

Published as: J. D. Assink, G. Averbuch, P. S. M. Smets, and L. G. Evers (2016), On the infrasound detected from the 2013 and 2016 DPRKs underground nuclear tests, Geophysical Research Letters, 43 (7), 35263533, doi:10.1002/2016GL068497.
Note that minor changes have been introduced to make the text consistent with the other chapters.

is difficult to estimate from seismic data alone, this motivates a synergy between seismics and infrasonics.

■ 2.1.1 Introduction

Sources of seismic energy in the subsurface can generate low-frequency acoustic waves in the atmosphere, i.e., infrasound. Examples of such sources are earthquakes and explosions [*Donn and Posmentier*, 1964]. There are various mechanisms through which seismic waves in the subsurface can couple to infrasonic waves in the atmosphere, at the lithosphere-atmosphere interface. Previous studies with earthquake recordings have shown: (1) epicentral infrasound, (2) topographical infrasound and (3) evanescently coupled infrasound. (1) Epicentral infrasound is the direct coupling of seismic-to-infrasonic energy at the earthquake's epicenter, due to the movement of the earth surface [*Mutschlecner and Whitaker*, 2005]. (2) Topographical infrasound can be generated away from the epicentral region by the movement of mountain ranges [*Le Pichon et al.*, 2006] or steep slopes, like a cliff [*Green et al.*, 2009]. Here also the movement of the earth surface due to seismic waves is the source of infrasonic waves [*Walker et al.*, 2013]. (3) Evanescently coupled infrasound has been observed from an earthquake under the ocean. Secondary sources in the water column generated hydro-acoustical waves. The ocean-atmosphere interface became anomalously transparent, since the underwater source depths were within one acoustic wavelength, generating infrasound in the atmosphere [*Evers et al.*, 2014].

When a source in the subsurface is capable of generating infrasound, there is no guarantee that the infrasound generated will be detected at a distant station. This strongly depends on the source-receiver distance, the atmospheric winds and temperature and noise levels at the receiver due to wind and turbulence. In long-range infrasound propagation, i.e., over distances of more than 100 km, the state of the stratosphere [*Assink et al.*, 2014; *Waxler et al.*, 2015] and to a lesser extent the thermosphere determine the (un)favorable conditions for detection.

The Democratic People's Republic of Korea (DPRK) has tested four nuclear devices over the years 2005 and 2016 [*Selby*, 2010; *Wen and Long*, 2010]. All four tests took place at the Punggye-ri Nuclear Test Site in the northeast of the country (see Figure 2.1). It is a mountainous area, mainly consisting of granite. Details on the source are listed in Table 2.1 and are derived with seismic stations from the global International Monitoring System (IMS). The IMS is in place for the verification of the Comprehensive Nuclear-Test-Ban Treaty (CTBT). Next to seismic stations, the IMS also consists of radionuclide, hydro-acoustic and infrasonic measurement devices [*Dahlman et al.*, 2009]. Recordings from the latter will be used in this study. The closest IMS infrasonic stations to the Punggye-ri site are in the Russian Federation (I45RU) and Japan (I30JP), as shown in Figure 2.1. Infrasound has not been detected on IMS infrasound stations from the 2006 and 2009 test. Non-IMS infrasound stations will not be considered here [*Che et al.*, 2009]. A suggested fifth test in 2010 is disputed and will not be discussed, as it would have had a too small

Table 2.1: *Details from the DPRK's nuclear tests using the IMS. Yield estimates were obtained from NORSAR, as published at http://www.norsar.no/norsar/about-us/News/North-Korea-nuclear-test-on-6-January-2016, last accessed 2016.01.21*

Date	Time (UTC)	Lat (deg)	Lon (deg)	Uncertainty (km^2)	Mb	Yield (kT TNT)
2006.10.09	01:35:27.58	41.3119	129.0189	880	4.1	∼1
2009.05.25	00:54:42.80	41.3110	129.0464	265	4.5	∼5
2013.02.12	02:57:50.80	41.3005	129.0652	181	4.9	∼10
2016.01.06	01:30:00.49	41.3039	129.0481	193	4.8	<10

yield to be detected with infrasound [*Zhang and Wen*, 2015].
In this study, it is discussed why infrasound from the 2013 DPRK nuclear test was clearly detected and why the 2016 test left a less clear signature in the atmosphere. Although the source strengths were comparable, the source depth, the state of the upper atmosphere and receiver noise levels appear to have played an important role in the detectability of infrasound. Since the depth of an explosion is difficult to estimate from seismic data alone [*Bowers and Selby*, 2009], this motivates a synergy between the seismic and infrasound technologies to improve on the depth estimation of (nuclear) explosions.

■ 2.1.2 Atmospheric propagation of infrasound in 2013 and 2016

Infrasound can travel over long ranges, because of its low frequency contents and since several wave guides exist in the atmosphere, in which acoustic energy can be trapped. Three wave guides between the earth's surface and upper atmosphere exist. (1) The tropospheric wave guide with its upper bound in the tropopause (∼10 km), caused by the jet stream. Winds at a lower level and temperature inversions can also form a tropospheric wave guide. (2) The stratospheric wave guide with its upper limit around the stratopause (∼50 km), formed by the temperature increase due to the presence of ozone and the circumpolar vortex. (3) The thermospheric wave guide from the mesopause (∼90 km) and upwards, due to the increase in temperature. However, infrasonic waves are much attenuated at these altitudes in the highly rarefied atmosphere.

The wind strength and direction, as a function of altitude, make the atmosphere a highly anisotropic medium for the propagation of infrasound. Typically, infrasound is detected in the down-wind direction. The westerly jet stream near the tropopause directs the infrasound to the east, while the direction of circumpolar vortex changes direction between the equinoxes. On the northern hemisphere, the polar vortex is directed to the east in winter and west in summer. The summer stratosphere is stable, but in winter planetary waves from the troposphere can propagate into the stratosphere. Interaction of such waves with the polar vortex can lead to Sudden Stratospheric Warmings (SSWs). Even bi-directional wave guides can be formed

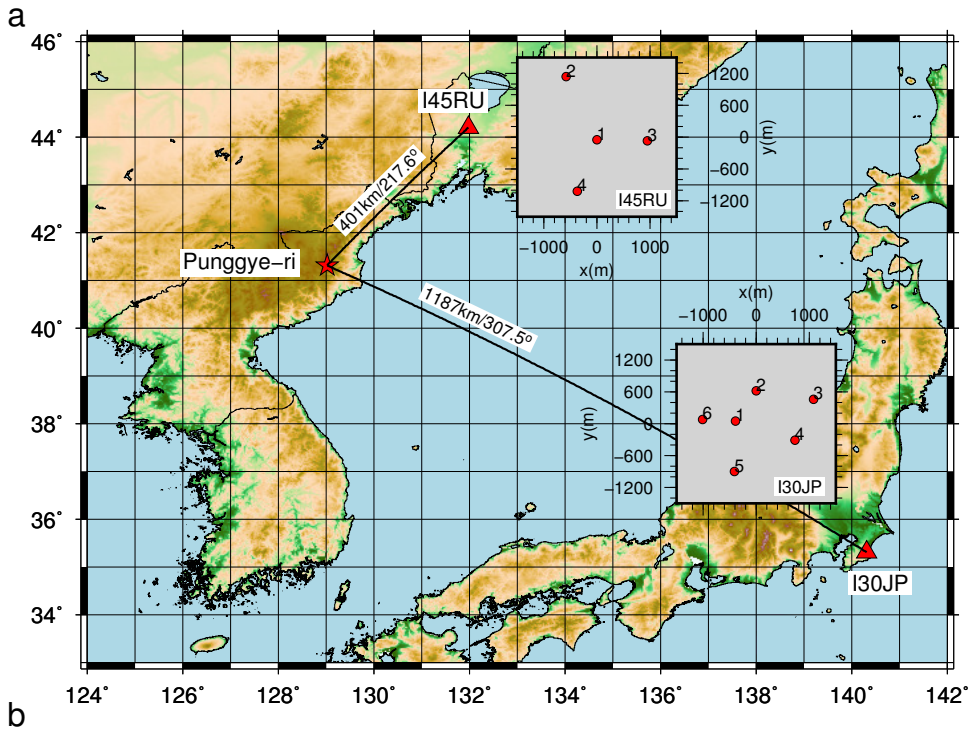
a
I45RU
401km/217.6°
Punggye–ri
1187km/307.5°
I30JP
x(m)
y(m)
b
Punggye–ri
2006
2009
2013
2016
km
0
10

under such circumstances [*Assink et al.*, 2014]. These SSWs occur every winter and can be minor or major. In the latter case, stratospheric winds reverse and the temperature increases with tens of degrees Celsius in only a few days. These conditions strongly affect infrasound propagation [*Evers and Siegmund*, 2009; *Evers et al.*, 2012; *Smets and Evers*, 2014].
Infrasonic propagation can be modeled in a high frequency approach by applying raytracing. However, such an approach does not cover full wave effects like scattering and diffraction. Therefore other methods, such as the Parabolic Equation (PE) method are used, which account for full wave phenomena [*Collins*, 1993]. Inputs necessary for the propagation modeling are atmospheric specifications of density, temperature and wind. Especially, the latter two are highly variable as a function of altitude, time and geographical location. The European Centre for Medium-Range Weather Forecasts (ECMWF) provides hourly global atmospheric specifications with a spatial resolution of 0.125 degree, up to 0.01 hPa (∼79 km altitude).

Figure 2.2 shows the ECMWF's wind and temperature specifications near the stratopause (1.5 hPa or ∼45 km). In February 2013, there was a well developed circumpolar vortex around the cold Arctic stratosphere. In contrast, in January 2016, the vortex was displaced from its circumpolar trajectory and a warm stratosphere was present over the area of interest. The eastward vortex, as in 2013, is no longer present and a mixture of eastward and westward wind directions is visible over the area of interest. Such a state of the stratosphere is formed in the early stages of a SSW. The results on the propagation of these different wind and temperature conditions, between the years, are shown in Figure 2.3.

A well formed tropospheric and stratospheric wave guide is present for I45RU in 2013. Both wave guides exist due the strong winds near the tropopause and stratopause. Comparing the adiabatic and effective sound speed, which takes into account the wind effect, shows that the jet stream and circumpolar vortex, respectively, lead to a downward refracting atmosphere. In 2016, tropospheric and weak stratospheric refractions are predicted to reach I45RU. The stratospheric paths interact with the troposphere, but have a relative large transmission loss, due to the weaker vortex. Tropospheric refractions are predicted for I30JP in both 2013 and 2016, which are caused by the jet stream. A weak stratospheric return might be observed in 2013. However, the partly counteracting circumpolar vortex in 2016 will prevent such a

Figure 2.1 (preceding page): *(a) Map showing the DPRK's Punggye-ri Nuclear Test Site in the northeast of the country. The IMS infrasound arrays, and their configurations of microbarometers are also shown, being I45RU in the Russian Federation and I30JP in Japan. Element 2 from I45RU was missing in 2013 and element 3 from I30JP in 2016. (b) Map showing the locations of the nuclear test at the Punggye-ri site from 2006, 2009, 2013 and 2016. The uncertainty ellipses are also shown, as derived from IMS seismic recordings (see Table 2.1 for details).*

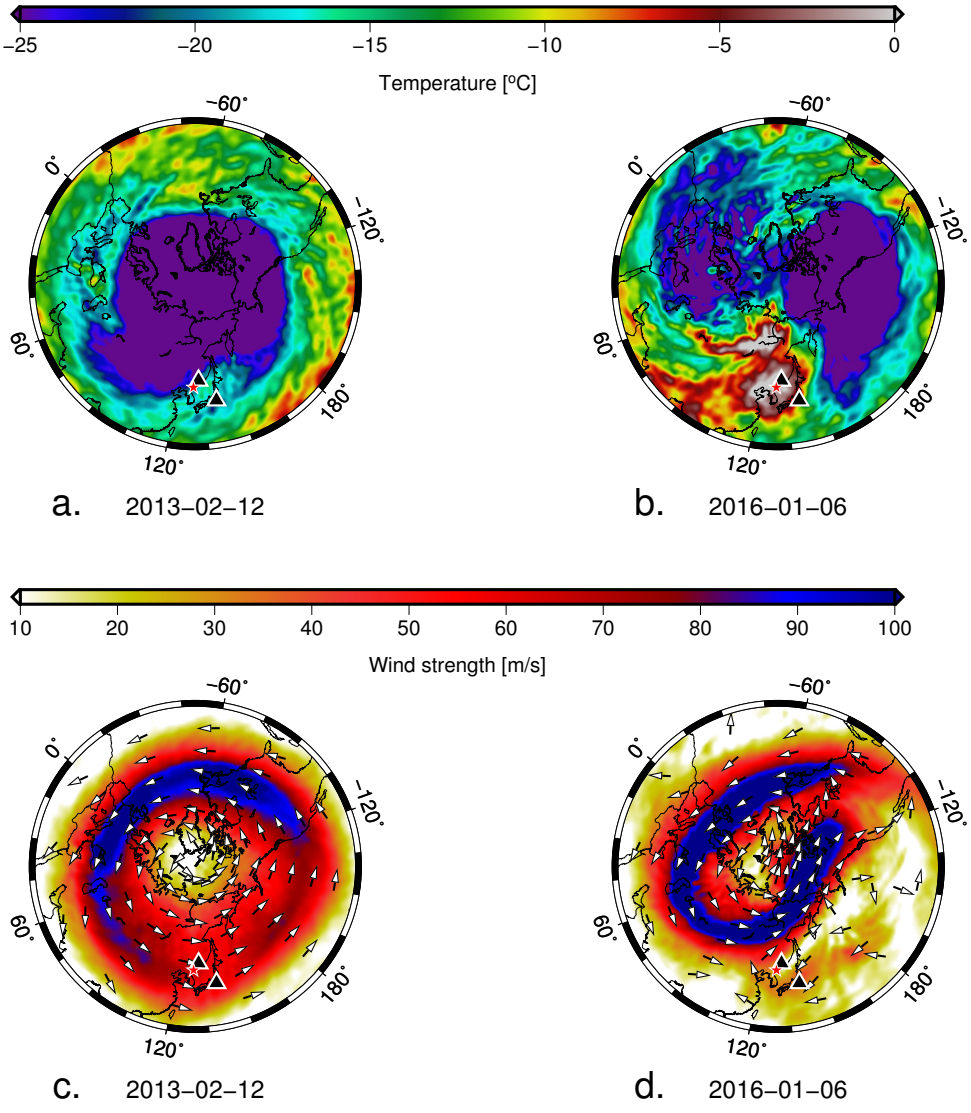

Figure 2.2: *The wind and temperature at 1.5 hPa (∼45 km) from ECMWF atmospheric specifications. IMS infrasound stations are indicated with the black triangles, being I45RU to the north of Punggye-ri (star) and I30JP to the east. The temperatures are given in the top frames, for (a) 2013-02-12 03:00 UTC and (b) 2016-01-06 02:00 UTC. The wind strength and direction are shown in the bottom frames for (c) 2013 and (d) 2016.*

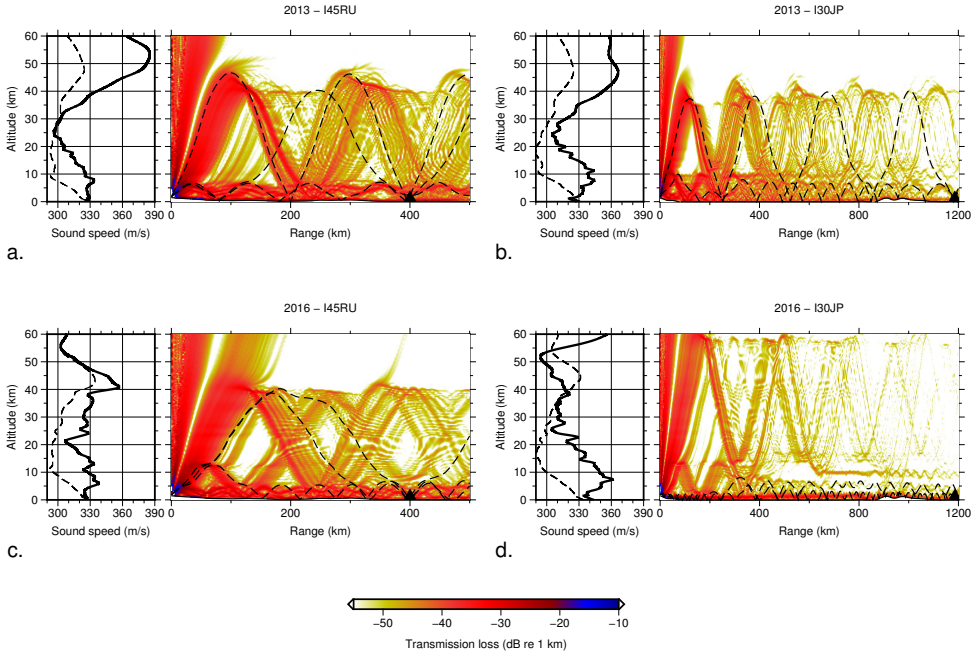

Figure 2.3: *The propagation of infrasound from the Punggye-ri Nuclear Test Site to the IMS infrasound stations, for I45RU in (a) 2013 and (c) 2016 and for I30JP in (b) 2013 and (d) 2016. The transmission loss is shown as a function of distance and altitude at 1.0 Hz. The eigenrays that connect the source and receiver are shown as dashed lines. The adiabatic (dashed line) and effective sound speeds (solid line) are given in separate frames, to the left of each propagation frame. These profiles are taken at the mid-point between source and receiver. In Table 2.2 the exact transmission loss values are given.*

Table 2.2: *Transmission loss in dB re. to 1 km at 1.0 Hz, for tropospheric (Iw) and stratospheric (Is) refractions*

2013	Iw	Is
I45RU	-37.7	-47.9
I30JP	-53.4	-53.4
2016		
I45RU	-38.1	-53.0
I30JP	-50.6	-67.5

stratospheric refraction. In 2016, the refraction altitude is higher than in 2013, which leads to a stronger attenuation. Furthermore, the strong jet stream hardly allows refractions to reach the earth's surface. A so-called elevated wave guide has formed. The transmission losses at each array are given in Table 2.2.

■ 2.1.3 Infrasound detections of the 2013 and 2016 tests

Infrasound is measured with arrays of microbarometers (see Figure 2.1), which are sensitive in the frequency range of at least 0.02 to 4 Hz. Within this range, small-sized atmospheric nuclear tests of about 1 kT TNT can be detected, as these are expected to generate infrasound of 0.1 to 0.2 Hz. Underground tests can generate higher frequencies in the atmosphere, as the seismic wavefield contains more higher frequencies. The advantage of measuring with arrays is twofold. (1) The noise due to wind and turbulence is reduced by summing the signals of the individual microbarometers. Those are spaced at such a distance that the wind field leaves an incoherent pressure field, while the long wave lengths of the infrasound are coherent. (2) The apparent velocity of the infrasonic wave can be estimated, being a measure of the angle of incidence of the wave. Furthermore, the direction of arrival or back azimuth can be obtained. In order to do so, beamforming is applied to the individual recordings, by time delaying and summing the recordings.

Continuous infrasonic recordings are processed based on the signal coherency, with a sliding window approach. An increase in signal coherency over the array indicates the presence of an infrasonic wave. The Fisher ratio is a sensitive measure of the signal coherency or signal-to-noise ratio (SNR) [*Melton and Bailey*, 1957]. Array processing results are shown for the I45RU and I30JP infrasonic recordings in 2013 and 2016, in Figure 2.4. I45RU clearly detects both tropospheric (Iw) and stratospheric (Is) refractions in 2013. A intermediate return (Iws) is also identified, which is a signal that has leaked from the troposphere into the stratosphere (see also Figure 2.3). The expected arrival time, back azimuth and apparent velocity (blue dots) from raytracing and the observations (red dots) are in agreement. The increase in apparent velocity as a function of time is representative for the increase in refractions altitude. Furthermore, the celerities (horizontal distance divided by traveltime), as given in the SNR-frame, correspond to the expected values for tropospheric and stratospheric returns [*Brown et al.*, 2002]. Other local impulsive sources with a high SNR are visible throughout the recording. In 2016, only one arrival is potentially identified at I45RU. This arrival can be associated with both tropospheric and stratospheric propagation paths (Figure 2.3c), considering the observations and the modeled parameters. The detection is very weak and its identification is much dependent on the processing parameters. In that sense, it is a rather unstable detection that might be missed with different settings for the binsize, overlap and corner frequencies of the bandpass filter. The local noise levels in 2016 are higher than those in 2013, as can be seen from the high spectral values in the spectrograms, outside the times signal is present. ECMWF surface winds are 2.4 m/s in 2016 and 0.9 m/s in 2013, which are consistent with higher noise levels.

Tropospheric returns are not observed in I30JP neither in 2013 nor in 2016. The only refractions that could be identified is a stratospheric return in 2013. Noise levels from the spectral amplitudes seem not to differ too much. The surface winds in 2016 are only slightly higher than those in 2013, i.e., 1.9 versus 1.6 m/s.

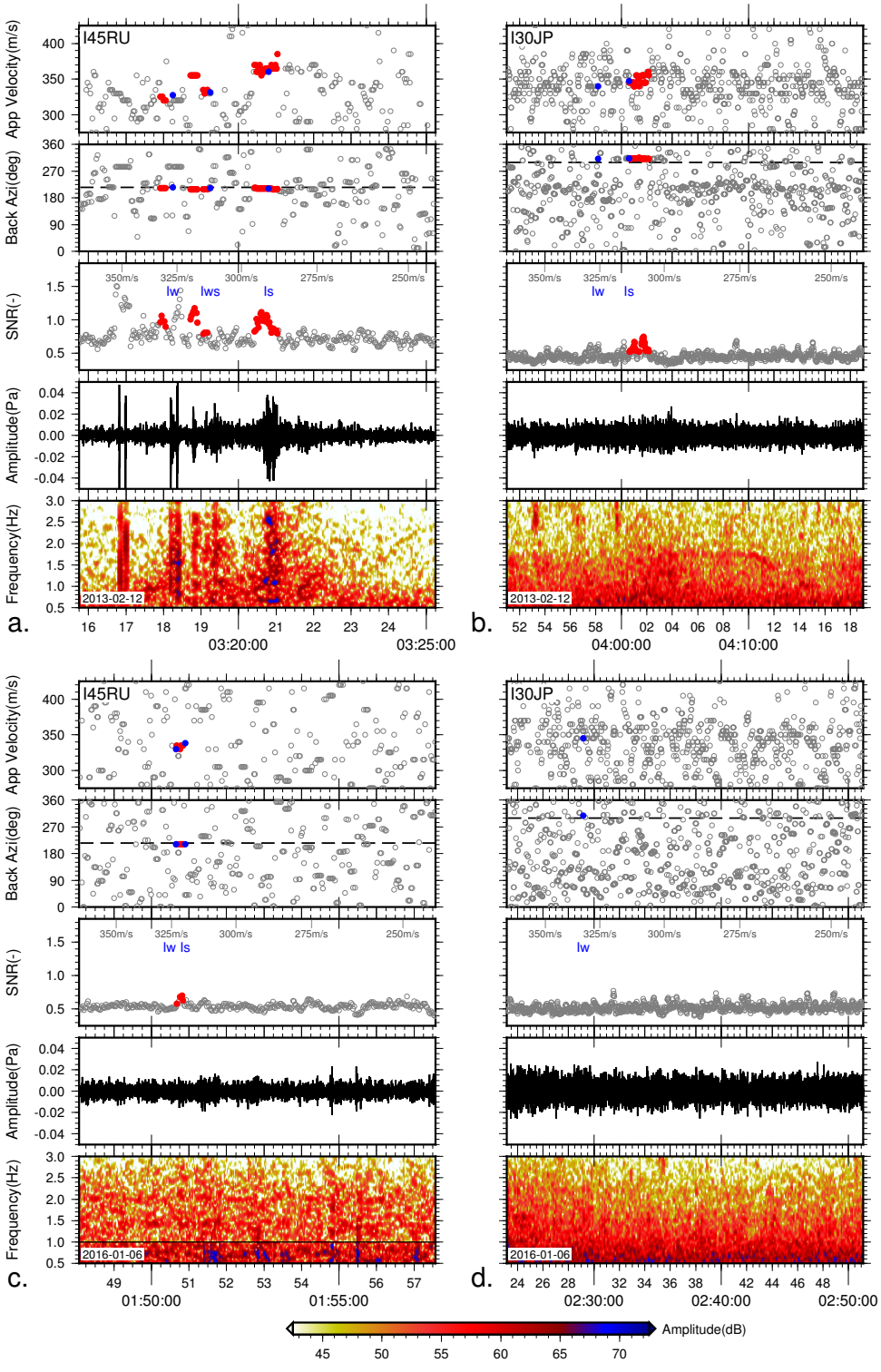
I45RU
I30JP
App Velocity(m/s)
Back Azi(deg)
SNR(-)
Amplitude(Pa)
Frequency(Hz)
350m/s 325m/s 300m/s 275m/s 250m/s
Iw Iws Is
2013-02-12
2016-01-06
a.
b.
c.
d.
03:20:00
03:25:00
04:00:00
04:10:00
01:50:00
01:55:00
02:30:00
02:40:00
02:50:00
Amplitude(dB)
45 50 55 60 65 70

■ 2.1.4 Discussion and conclusions

The underground nuclear tests conducted by the DPRK in 2013 and 2016 both generated observable atmospheric infrasound. Clear signatures were obtained in the Russian Federation, by IMS array I45RU, and in Japan by I30JP in 2013. At I45RU both a tropospheric and stratospheric refraction were identified from the 2013 test. In 2016, only a weak tropospheric return could potentially be found at I45RU. The stratospheric refraction detected at I30JP in 2013 was not observed in 2016.

The following explanations are postulated, based on observations and modeling.
(1) The 2016 stratosphere was disturbed by planetary waves interacting with the circumpolar vortex, i.e. a possible early stage SSW. Propagation of infrasound through the stratosphere was unfavorable for I30JP. This also follows from the transmission loss modeling (see Table 2.2).
(2) The local noise levels at I45RU due to wind were higher in 2016 than 2013, which can obscure a clear detection.
(3) It should be noted that the detection capability of I45RU was higher in 2016 than in 2013, since one of the microbarometers (element 2) was missing in 2013.
(4) The size of the nuclear test, in terms of yield, might be somewhat smaller in 2016 (m_b 4.8) than in 2013 (m_b 4.9), based on IMS magnitudes. Therefore, less energy was possibly coupled into the atmosphere. However, it should be noted that this difference in magnitudes falls within the typical range of uncertainties. Indeed, comparable seismic moment magnitudes have been estimated for the 2013 ($M_w = 4.7$) and 2016 ($M_w = 4.71$) events [*IRIS*, 2013, 2016], as well.

We have not considered scattering off small-scale atmospheric structure (e.g. Kulichkov et al. [2010]), which could enhance stratospheric propagation efficiency, in particular for 2016. The lack of detections of tropospheric refractions at I30JP can only be explained by the fact that the wave guide is very thin and its continuity can be disrupted by wind and turbulence.

Figure 2.4 (preceding page): *Results from array processing the infrasonic recording of I45RU in (a) 2013 and (c) 2016 and those for I30JP in (b) 2013 and (d) 2016. For each array and date, a set of four frames is shown to characterize the signals. Shown are subsequently: the spectral contents, the bestbeam, the signals-to-noise ratio (SNR), the back azimuth (with the true back azimuth as dashed line) and the apparent velocity, from bottom to top and as a function of time. The celerities are given in m/s in the SNR-frame. The red dots indicate events of interest which are also labeled as Iw, Iws and Is, for respectively tropospheric, combined tropospheric-stratospheric and stratospheric refractions. The blue dots follow from three-dimensional raytracing (in spherical coordinates) through ECMWF atmospheric specifications. The following settings were used to obtain these results: binsize 256 samples, overlap 224 samples, 2nd order Butterworth filter with two passes and corner frequencies of 0.5 to 3.0 Hz (for I45RU 2016 1.0 to 3.0 Hz).*

The fact that (1) tropospheric propagation towards I45RU was similar in 2013 and 2016 and no clear detection could be made at I45RU in 2016, (2) no stratospheric returns were identified at I45RU, though possible from the transmission loss calculations and (3) the seismic magnitudes of the 2013 and 2016 test explosions were comparable, motivates us to hypothesize that the 2016 test was at a greater depth than the 2013 test.

Based on a preliminary analysis of relative source depths of the 2013 and 2016 explosions (Appendix B), we estimate that the 2016 test took place 1.5 times deeper than the 2013 test. Such an explanation could indeed explain the reduced coupling of seismic energy through the lithosphere-atmosphere interface. However, this hypothesis should be further tested, to investigate the effects of differences in rock conditions as well as uncertainties in yield estimates and atmospheric structure.

Future studies, involving a more extensive observational dataset and numerical modeling that accounts for lithosphere-atmosphere coupling and varying geological conditions, will be conducted to further test this hypothesis and to provide quantitative constraints on the source depth. As the depth of an explosion is difficult to estimate from seismic data alone [*Bowers and Selby*, 2009], infrasound may thus provide useful complementary information.

2.2 A Seismo-Acoustic Analysis of the 2017 North Korean Nuclear Test

Abstract The 2017 North Korean nuclear test gave rise to seismic and low-frequency acoustic signals, i.e. infrasound. The infrasonic signals are due to seismo-acoustic coupling and have been detected on microbarometer array I45RU in the Russian Federation at 401 km from the test site. I45RU is part of the International Monitoring System for the verification of the Comprehensive Nuclear-Test-Ban Treaty. We analyze the seismo-acoustic coupling by making use of array processing and back-projection techniques. The back-projections show that infrasound radiation is not confined to the epicentral region. More distant regions are found to be consistent with locations of topography, sedimentary basins, and underwater evanescent sources. The back-projections can be used to estimate the average infrasonic propagation speed through the atmosphere. We discuss these findings in the context of infrasound propagation conditions during the sixth nuclear test. It is suggested that propagation from the test site to I45RU may have occurred along unexpected paths instead of typical stratospheric propagation. We present several scenarios that could be considered in the interpretation of the observations.

■ 2.2.1 Introduction

The Democratic People's Republic of Korea (DPRK) has performed six underground nuclear tests since 2006. Seismic signals from these tests have been detected globally and have been used to estimate the epicenter, origin time and seismic magnitude. The seismic measurements indicate that the DPRK has tested larger nuclear weapons over time. The facilities of the International Monitoring System (IMS), which is in place for the verification of the Comprehensive Nuclear-Test-Ban Treaty (CTBT), have been instrumental in the accurate localization and characterization of the tests (e.g., *Gibbons et al.* [2017]). The yield estimate of the explosions strongly trades-off with their depth, which is difficult to estimate from tele-seismic arrivals alone [*Bowers and Selby*, 2009].

Large seismic sources also generate observable infrasound in the atmosphere. The coupling of seismic waves to atmospheric infrasound waves can occur due to various mechanisms. Generation of acoustic waves from surface waves in a solid-fluid system is a well-known phenomenon [*Stoneley*, 1926; *Scholte*, 1947]. It has been shown that air-coupled surface waves also contribute to the observed acoustic signal in the atmosphere [*Ewing et al.*, 1957; *Ben-Menahem and Singh*, 1981]. It follows that the solid earth-atmosphere and ocean-atmosphere interfaces are transparent for the inhomogeneous part of the wave field as this spectrum includes low phase velocities that are evanescent in the solid earth or oceans, but can be propagating in the atmosphere [*Godin*, 2008, 2011]. Evanescently coupled infrasound has been

Published as: J. Assink, G. Averbuch, S. Shani-Kadmiel, P. Smets, and L. Evers (2018), A SeismoAcoustic Analysis of the 2017 North Korean Nuclear Test, Seismological Research Letters, doi:10.1785/ 0220180137.
Note that minor changes have been introduced to make the text consistent with the other chapters.

observed from the 2004 Mw8.1 Macquarie ridge earthquake, as acoustic signals with relatively large wavelengths coupled from shallow underwater features [*Evers et al.*, 2014].

Previous studies of infrasound from earthquakes have shown that most of the coupled seismo-acoustic signals originate from the epicentral region. This is referred to as epicentral infrasound. In addition, secondary infrasonic signals have been observed from the movement of mountain ranges, away from the epicenter [*Young and Greene*, 1982; *Le Pichon et al.*, 2003; *Green et al.*, 2009]. In an analysis of the 2016 Central Italy earthquakes, it was shown that seismo-acoustic coupling occurs over an even larger extent. The detection of these signals was dependent on the ground-to-air coupling and atmospheric propagation conditions to a distant array [*Shani-Kadmiel et al.*, 2018].

The detection of infrasound at a remote station is strongly dependent on the noise levels due to the local wind and turbulence and the propagation conditions along the source-receiver path. Long-range infrasound propagation, i.e. propagation over distances longer than 100 km, is facilitated by atmospheric waveguides. These waveguides are formed between the ground and atmospheric layers aloft and are much dependent on the prevailing vertical temperature and wind distribution. The stratospheric waveguide is particularly important in the detection of long-range infrasound and is sustained by a strong wind jet around 50 km altitude, i.e. the stratospheric vortex. As the direction of the flow reverses during the equinoxes, the propagation efficiency of the stratospheric waveguide reduces. A thermospheric waveguide always exists because of a strong temperature gradient in the lower thermosphere. The low density in the upper atmosphere leads to non-linear propagation effects and significant absorption (e.g., *Lonzaga et al.* [2014]; *Waxler et al.* [2017b]).

Previous underground nuclear tests by the DPRK have generated infrasound that has been observed on IMS stations [*Assink et al.*, 2016] and infrasound arrays in South Korea [*Che et al.*, 2014]. As seismo-acoustic coupling is related to source depth, this motivates a synergy between seismology and acoustics, e.g. to improve depth-yield estimates of (nuclear) explosions. The effect of source depth on seismo-acoustic coupling has been studied previously [*Arrowsmith et al.*, 2011; *Ford et al.*, 2014]. *Assink et al.* [2016] hypothesized that a relative source depth between two events can be estimated from infrasonic observations. In this procedure, 1) the coupling of seismic waves to infrasound is quantified and 2) the propagation paths are known in order to estimate the relative transmission loss from the Earth surface to the receiver.

In this article, we focus on a seismo-acoustic analysis of the 03 September 2017 nuclear test. Besides a main event at 03:30:01 UTC, a non-tectonic aftershock occurred at 03:38:32 in the vicinity of the test site, possibly related to collapse of the underground cavity [*Liu et al.*, 2018]. The source characteristics are summarized in Table 2.3 and are derived with seismic stations from the IMS. Infrasound was

Table 2.3: *Details from the events associated with the 2017 North Korean Nuclear Test from the Revised Event Bulletin (REB) published by the CTBT Organization. The yield estimates are estimated by NORSAR, as published at https://www.norsar.no/press/latest-press-release/archive/the-nuclear-explosion-in-north-korea-on-3-september-2017-a-revised-magnitude-assessment-article1548-984.html, last accessed on 30 April 2018.*

	Time	Lat (deg.)	Long (deg.)	m_b	Est. Yield (kT)
Nuclear Test	03:30:01.08	41.3205	129.0349	6.1	200 - 300
Aftershock	03:38:32.08	41.3206	129.0615	4.1	-

detected on a nearby IMS infrasound array in the Russian Federation, I45RU (see Figure 2.5), as well as in South-Korea. This analysis focuses on seismo-acoustic signals that have been detected on I45RU. This array is located at a distance of 401 km distance to the northeast of the Punggye-ri Nuclear Test Site. We show that array processing and back-projections using recorded data from this IMS array provide unprecedented insight into seismo-acoustic coupling.

Furthermore, we discuss the infrasound propagation conditions during the sixth nuclear test, during which the stratosphere was in a state of transition from summer to winter and the stratospheric vortex was relatively weak. As long-range infrasound propagation is largely conditioned by the strength and the direction of the stratospheric vortex, this implies that propagation from the test site to I45RU may have occurred along unexpected paths [*Kulichkov*, 2010; *Green et al.*, 2011; *Chunchuzov et al.*, 2015]. We present several scenarios that could be considered in the interpretation of the observations.

■ 2.2.2 Data acquisition and processing

I45RU is a triangular array with a central element and has an aperture of 2.1 km. The array is equipped with four MB2000 absolute microbarometers that have a flat frequency response between 0.01-8 Hz. A rosette wind-noise reduction system is used to reduce wind noise over the infrasonic frequency band by spatially averaging the pressure field in the vicinity of each infrasound sensor. The MB2000 sensors sample the pressure field at 20 Hz. The microbarometers are primarily sensitive to pressure fluctuations but appear to be responsive to mechanical vibrations as well [*Alcoverro et al.*, 2005]. The sensitivity to both seismic and acoustic waves has been discussed in previous seismo-acoustic analyses of larger earthquakes (e.g., *Le Pichon et al.* [2003]; *Shani-Kadmiel et al.* [2018]).

We use time-domain [*Melton and Bailey*, 1957] and frequency-domain [*Smart and Flinn*, 1971] beamforming techniques for the detection of coherent infrasound and the estimation of plane wave parameters, i.e. back azimuth and apparent velocity. The detection of a signal is based on the evaluation of a Fisher ratio. The probability of detection can be estimated through the statistical framework of Fisher

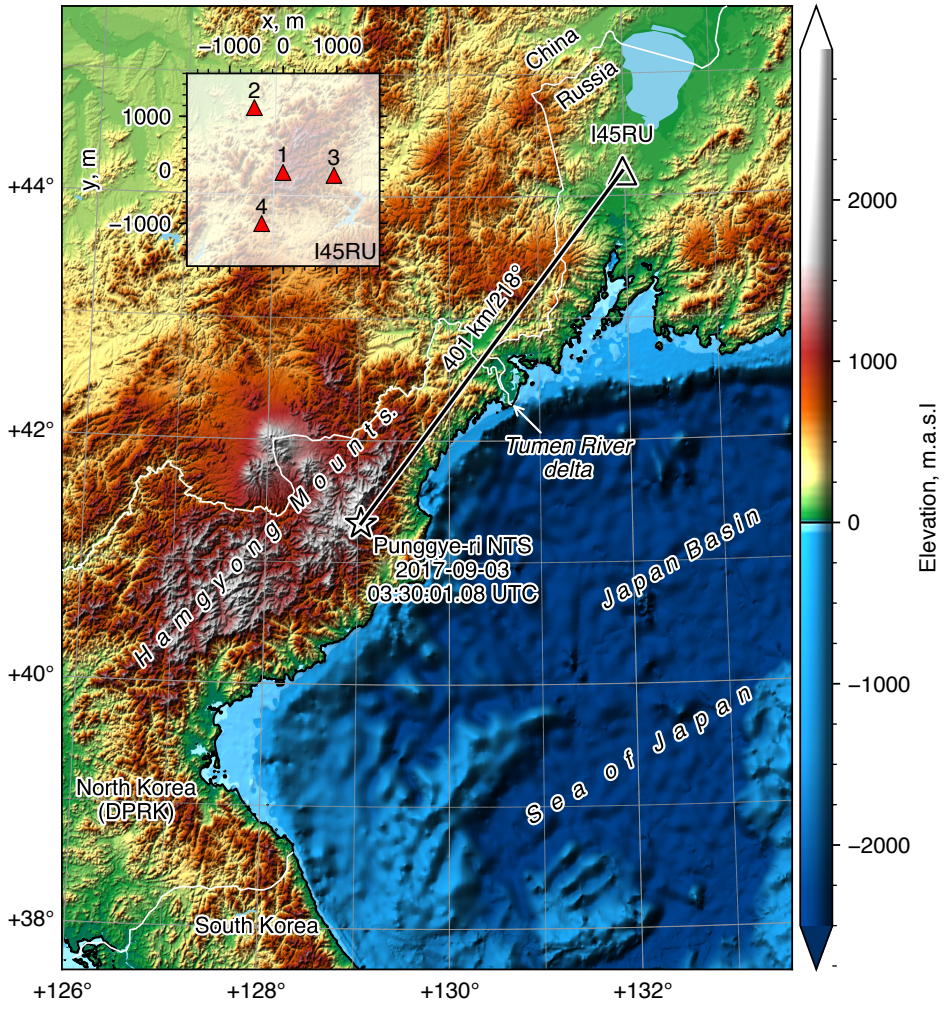

Figure 2.5: *Shaded relief of surface topography and bathymetry from General Bathymetric Chart of the Oceans (GEBCO) 30 arc-second grid [Weatherall et al., 2015]. Punggye-ri Nuclear Test Site (NTS) and event epicenter marked by a star and IMS array I45RU marked by a triangle. Hamgyong Mountains and Tumen River delta are marked for further discussion in the text. Inset frame shows I45RU 4 microbarometer configuration.*

statistics. Moreover, a single-channel SNR value can be estimated from the Fisher ratio. A detailed description of these algorithms can be found in *Evers* [2008].

The waveform data is detrended and band-pass filtered before time-domain beamforming. A second order Butterworth band-pass filter between 0.35 to 4 Hz

appears to be a good trade-off between the coherency of the signals of interest and interference from low-frequency noise, such as coherent noise in the microbarom band. In addition, a 1.0-3.0 Hz frequency band is considered in order to detect smaller amplitude arrivals that would otherwise be masked. The waveforms are oversampled to 100 Hz using Fourier interpolation for an enhanced time resolution as smaller time shifts may be used. This enhanced time resolution benefits the beamforming of the seismic arrivals.

The frequency-domain algorithm carries out the analysis in discrete frequency bands. The window size is 20 and 40 seconds for the time-domain and frequency domain processing, respectively. In all cases, we consider 90% overlap between successive windows. The samples are delayed and summed over a horizontal slowness grid. The grid is designed to include back azimuth and apparent velocity values of interest. The back azimuth values range between 155 to 270 degrees and are spaced by 1 degree. The lower limit of 155 degrees is selected to avoid detection of microbarom sources in the Pacific. The apparent velocity values range between 300 m/s and 10 km/s. Between 300 m/s and 450 m/s the values are separated by 5 m/s (the infrasonic signal range), and between 450 m/s and 10 km/s the values are logarithmically spaced (the seismic signal range).

■ 2.2.3 Array processing and waveform analysis

Figure 2.6 shows array processing results for I45RU between 03:30:00 and 04:05:00. From top to bottom, the frames show as a function of time: apparent velocity, back azimuth, best beam and coherency as a function of frequency. Detections with a SNR above 0.6 are colored conforming to the color map. Travel time and celerity (defined as the epicentral distance divided by the traveltime) are indicated on the lowest frame and are relative to the origin time. A first interpretation of the arrival structure follows from these celerity values.

Figure 2.6a shows the arrival of various coherent arrivals in the 0.35-4.0 Hz frequency band from the direction of the test site, indicated by the dashed horizontal line. The wave train between 57 and ~300 seconds corresponds to the seismic arrivals. The first P-wave arrives after 57 seconds, which is in agreement with the iasp91 seismic travel time tables [*Kennett et al.*, 1995]. After the high-frequency P-wave, a dispersive Lg wave group is detected, which represents a guided waveform with predominantly transverse particle motion. The measured apparent velocities are consistent with seismic propagation velocities. The seismic waves radiate infrasound vertically into the atmosphere, which is measured by the microbarometer (e.g., *Cook* [1971]). However, part of this measurement is a contribution from the mechanical sensitivity of the MB2000 [*Alcoverro et al.*, 2005], for the larger accelerations between 57 and ~130 s.

The second set of arrivals from the direction of the test site corresponds to infrasound waves that have propagated through the atmosphere, having typical celerity

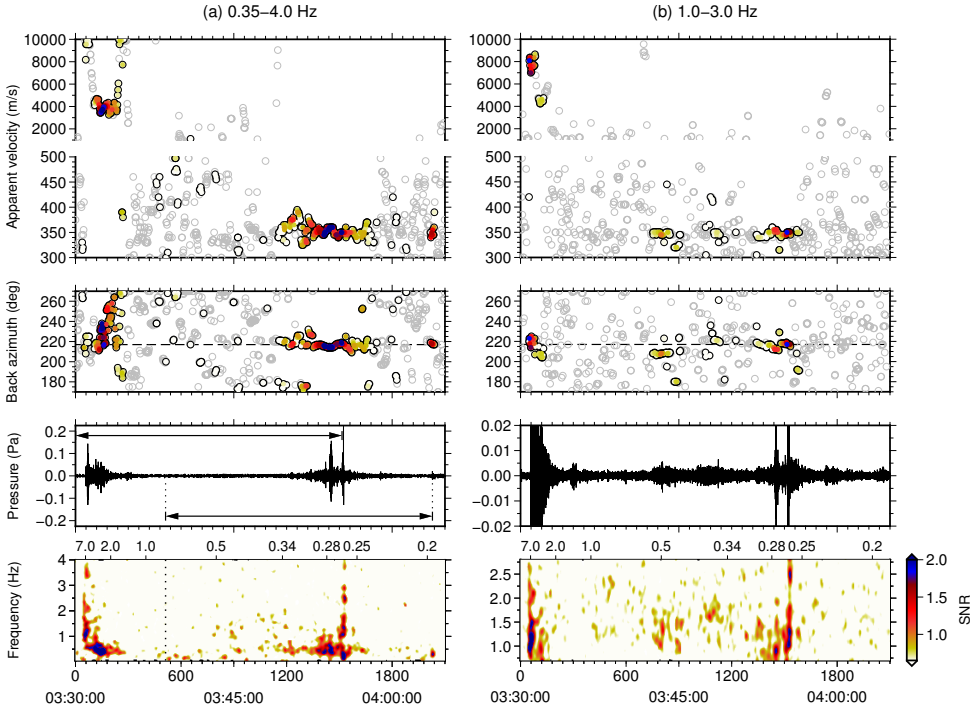

Figure 2.6: *Array processing results (a) 0.35-4.0 Hz wide-band, and (b) 1.0-3.0 Hz narrow band of I45RU between 03:30:00 and 04:05:00 on 3 September 2017. The frames show the following wavefront parameters as a function of time: apparent velocity, back azimuth, best beam, and coherency as a function of frequency. The color scale indicates the signal-to-noise ratio (SNR) of the detection. Travel time in seconds and celerity (in km/s) are indicated on the lowest frame and are relative to the origin time.*

values between 0.23 and 0.34 km/s and apparent velocities around 340 m/s. These infrasonic arrivals are interpreted to be epicentral infrasound. The resolved back azimuth and apparent velocity values show significant variations along the mostly emergent wave train. Most of the energy is coherent in a frequency range between 0.35 to 1.5 Hz.

Within this wave train, two phases, which are detailed in Figure 2.7, stand out: (1) An oscillatory wave package with a duration of ~20 seconds, arriving after 1440 seconds with a dominant frequency around 0.4 Hz and a peak-to-peak (ptp) amplitude of 0.3 Pa. (2) A broadband signal arriving after 1510 seconds, coherent between 0.05 to 4 Hz and a ptp amplitude of 0.75 Pa. The broadband signal consists of higher frequencies that are superimposed on a low-frequency (~0.1 Hz) U-wave. The shape of this signal matches the classical shape of thermospheric return signals as described in many cases in the scientific literature [*Whitaker and Mutschlecner*,

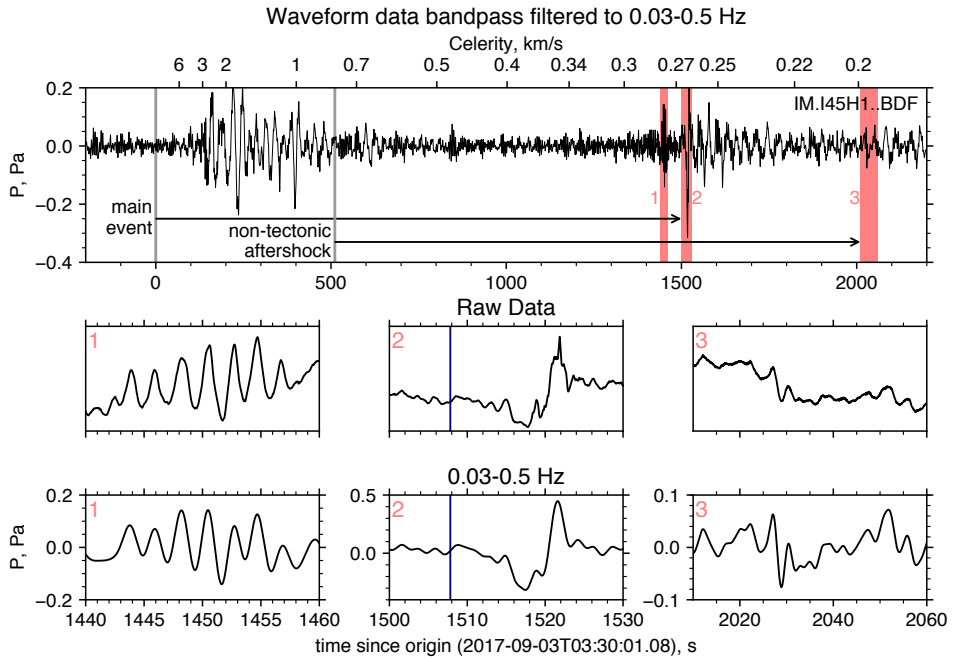

Figure 2.7: *Waveform data from element 1 of IMS array I45US. Top: Bandpass filtered to 0.03-0.5 Hz. 3 time windows marked in red are enlarged in the bottom two rows. Middle: Raw data, and Bottom: Bandpassed. The number at the top-left corner of the middle and bottom frames corresponds to the label next to each of the marked windows in the top frame. Vertical lines at 0, 511, and 1507 (blue) seconds correspond to main event origin time, non-tectonic origin time and calculated time of arrival from ray theory, respectively. Time is in seconds since origin time of the main event. Celerity values with respect to the main event have been added to the top axis.*

2008; *Assink*, 2012; *Lonzaga et al.*, 2014].

Another arrival, labeled (3) in Figure 2.7, is observed around 2025 seconds after the main event, with a dominant frequency around 0.25 Hz and a ptp amplitude of 0.15 Pa. The back azimuth is consistent with the direction of the test site and apparent velocities are consistent with an acoustic signal. When associated with the non-tectonic aftershock, this late arrival has a similar travel time (indicated by horizontally spanning arrows in Figure 2.6a) as arrival (2) does with respect to the main event, suggesting it has propagated along a similar path.

Figure 2.6b shows the array processing results in the 1.0-3.0 Hz band. In between 600 and 1300 seconds, coherent infrasound is detected that is predominantly coherent between 1.0-2.0 Hz. As such, these arrivals have celerity values between

0.6 and 0.34 km/s and appear before the epicentral infrasound. Compared to the epicentral infrasound, these arrivals have much smaller amplitudes and arrive from a different back azimuth. The resolved back azimuth is 208°, whereas the test site is at 218°. Similar signals have been identified in previous studies on infrasound from large earthquakes, as secondary infrasound [*Le Pichon et al.*, 2003; *Marchetti et al.*, 2016; *Shani-Kadmiel et al.*, 2018]. To understand where seismo-acoustic coupling occurs, array processing results are back-projected following the method described in *Shani-Kadmiel et al.* [2018].

■ 2.2.4 Back projections

Detections shown in Figure 2.6 are back-projected assuming a constant seismic and infrasonic propagation velocities. Due to the order of magnitude difference between seismic and infrasonic propagation velocities, this procedure is much more sensitive to the latter than the former. It is therefor fairly safe to approximate the seismic propagation velocity by fixing it around the celerity value of the peak amplitude arrival of the seismic wave train and to test a range of infrasonic propagation velocities. For the purpose of this study we fixed the seismic propagation velocity to 6 km/s. In contrast to seismic propagation velocities, infrasonic propagation velocities are constrained to a relatively small range between 220 m/s and 340 m/s. In this range, 0.28 km/s was found to provide the best overlap with respect to epicentral location, topographic features, and potential sources of evanescent wave coupling (Figure 2.8). It also matches the celerity value for the peak amplitude arrival of the infrasonic signal and is in agreement with expected celerities of thermospheric returns.

A grid of theoretical source to receiver travel times (seismic + infrasonic) and back azimuths is constructed with a 0.05° spacing. Time of arrival and back-azimuth associated with each detection point arriving more than 600 seconds after origintime with SNR > 0.7 and apparent velocity in the 280 m/s to 450 m/s range, are used to locate the grid cell from which it most likely originated. The contribution of each detection to the count of detections originating in each cell is the associated SNR value; For example, two detections originating from the same grid cell, one with SNR=1 and another with SNR=0.8 will result in a count of 1.8. This approach does not account for any horizontal advection due to crosswind and along track wind, which may result in inaccurate locations. However, as described in the next section, during low wind conditions such as in this case, infrasound propagation is predominantly controlled by the temperature structure. Thus, we expect errors related to horizontal advection to be negligible.

Figure 2.8 shows back-projection results from both frequency bands shown in Figure 2.6. The wide-band back-projection (Figure 2.8a) illuminates an elongated infrasound radiation patch along the trend of the Hamgyong mountain range (see Figure 2.5 for location) with its maximum surrounding the test site. In the narrow-band back-projections, smaller patches of increased infrasound radiation within the

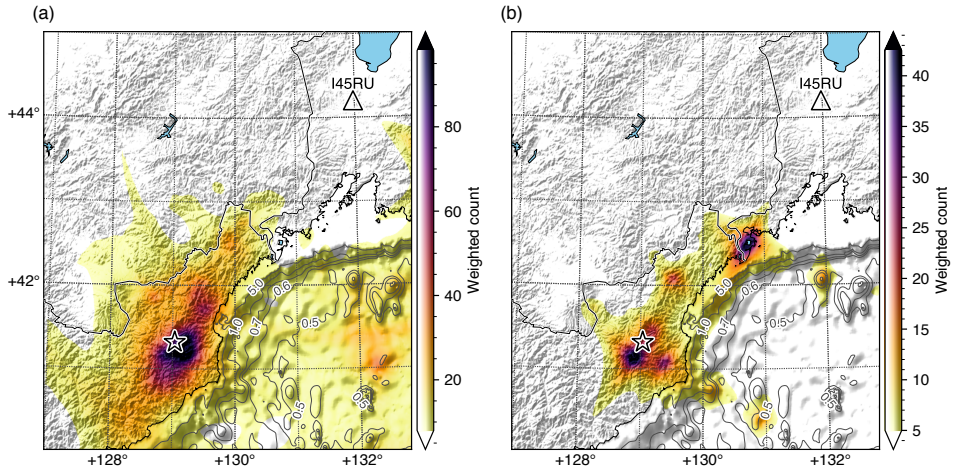

Figure 2.8: *Back-projection results for (a) 0.35-4.0 Hz and (b) 1.0-3.0 Hz frequency bands overlaid on a topography/bathymetry shaded relief (GEBCO 2014 30 arc-second grid, Weatherall et al. [2015]). Contour lines over the bathymetry correspond to water depth of 1 acoustical wavelength at the labeled frequency in Hz. The event location, as listed in the REB, is marked by a star; the I45RU array location is marked by a triangle. Color coding by (SNR) weighted count of detections that originate in each grid cell.*

mountain range suggest areas of more efficient radiation to station IS45 exist at this time (Figure 2.8b). Additionally, infrasound is detected from the Tumen River delta (see Figure 2.5 for location) about half way between the test site and I45RU. *Marchetti et al.* [2016] and *Shani-Kadmiel et al.* [2018] made similar observations of anomalous infrasonic radiation atop alluvial basins due to the interaction of seismic waves with the unconsolidated sediments. Interestingly, this area is not illuminated in the wide-band back-projections, presumably because seismic wave interaction with the shallow unconsolidated sediments of the Tumen River delta is likely to generate higher frequencies and in turn radiate infrasound in the higher frequency band. Infrasound is also detected from over the Japan Basin east of the test site. This basin is within 1 hydroacoustical wavelength of the water-air interface, suggesting evanescent wave coupling. Seismic wave interaction with seamounts protruding from the Japan basin generates higher frequencies. However, evanescent wave coupling may still occur as these are closer to the water-air interface. These effects are illustrated by our back-projection results in Figure 2.8. Contour lines in Figure 2.8 correspond to a depth of 1 acoustical wavelength at a range of frequencies calculated as $d_i = c_H / f_i$, with c_H the hydroacoustic speed of sound taken to be 1550 m/s.

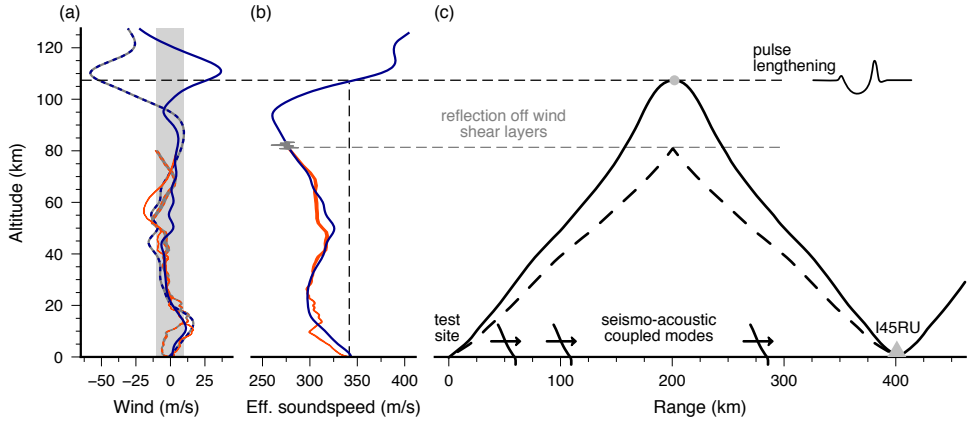

Figure 2.9: *Atmospheric profile at nuclear test site using the ECMWF HRES ensemble of analyses (red, whereas the width indicates the ensemble spread) and HMW14/MSIS-00 climatologies (blue). (a) Along track and crosswind from the test site towards I45RU, indicated by the solid and dashed lines, respectively. Grey area indicates wind velocities of 10 m/s and less. (b) Effective speed of sound approximation in direction of I45RU. A conceptual wind shear layer is added to aid in the understanding of a mechanism for acoustic reflections from mesospheric altitudes. (c) Thermospheric ducting (solid) with caustic (gray circle), simulated by ray theory using the HWM14/MSIS-00 climatologies. Alternative non-resolved paths can be mesospheric returns by reflection off strong wind shear layers (dashed) and seismo-acoustic coupled modes (arrow).*

■ 2.2.5 Infrasound propagation during a weak stratospheric vortex

For the analysis of infrasonic propagation conditions, we have compared the European Centre for Medium-range Weather Forecasts (ECMWF) operational high resolution ensemble of analyses (HRES EDA) [*Smets et al.*, 2015] with the MSIS-00 and HWM14 empirical models (Figure 2.9). The vertical structure of the atmosphere in the region of interest is characterized by a typical eastward jetstream (maximum wind velocity of 16.5 m/s at 11 km) and a weak westward stratospheric vortex (average wind velocity of 5.8 +/-0.5 m/s between 17-50 km) with a maximum in the stratopause (21.6 m/s at 55 km). Above 65 km, no synoptic state is represented by the climatologies: vertically narrow mesospheric inversion layers (MILs), intense wind shears, and sporadic layers are not present.

Since the nuclear test occurred near the autumnal equinox, planetary waves can reach a zero-wind condition in the middle atmosphere (stratosphere - mesosphere, Figure 2.9a) enhancing turbulence and small-scale wave activity. MILs typically form near the mesopause throughout the year and near the middle mesosphere during equinox and winter solstice periods [*Brown et al.*, 2004]. Small-scale structure and wind shear layers can occur e.g. due to (the breaking of) gravity waves [*Yue et al.*, 2010].

From the effective sound speed profile (Figure 2.9b), it follows that only a thermospherically ducted arrival is supported (Figure 2.9c). The effective sound speed is defined as the sum of the adiabatic sound speed and the wind speed in the direction of propagation. Estimates of travel time (1507 seconds, indicated by a vertical blue line in Figure 2.7), back-azimuth and apparent velocity from ray tracing are in first-order agreement with the observed low-frequency arrival at 1510 seconds after the explosion. This arrival has propagated through the mesosphere and lower thermosphere where non-linear propagation effects are significant. This non-linearity distorts the frequency content of the signal through signal lengthening and wavefront steepening. There is an interplay between these non-linear effects and attenuation as lengthening mitigates against signal attenuation while attenuation limits shock formation [*Lonzaga et al.*, 2014]. Indeed, this particular arrival is coherent down to 0.05 Hz.

However, this propagation path does not explain all the observed infrasound at I45RU, as infrasonic arrivals with high celerities, higher frequency content and other azimuths are also observed. These arrivals could be explained by a combination of various mechanisms (Figure 2.9c), including:

- Scattering and (partial) reflections off small scale structure and wind shear layers (e.g., *Kulichkov* [2010]; *Chunchuzov et al.* [2015]. Moreover, higher frequencies are more likely to reflect off such structures.
- Propagation along the Earth surface by coupled seismo-acoustic modes. This could be reflected by the similarity in the frequency spectrum between the Lg phase and the bulk of the infrasonic arrivals.
- Evanescent wave coupling from a shallow, low-frequency source. Interaction of radiated energy, from both evanescent and surface waves can keep the energy trapped near the surface and propagate over long distances.
- Uncertainties in atmospheric models or assimilation of data below the mesosphere is possible (e.g., *Smets et al.* [2016]). However simultaneous observations of Pacific microbaroms at the time of the nuclear tests indicates that the stratospheric vortex was indeed weak, yielding thermospheric ducting (see Appendix C).

Finally, the mathematical and physical approximations that are made in the derivation of the propagation modeling techniques should be considered.

■ 2.2.6 Discussion and Conclusions

Array processing of recorded pressure fluctuations at IMS array I45RU, 401 km northeast of the Punggye-ri Nuclear Test Site show seismic and infrasonic signals related to the nuclear test. Seismic arrivals are detected with a back azimuth that corresponds to the direction of the test site. Epicentral infrasound with acoustic

apparent velocities and celerities in the range 0.34 to 0.24 km/s are also detected as a result of the nuclear test.

Back-projections using the above detections in two frequency (wide- and narrow-) bands reveals sources of infrasound radiation. Four infrasound sources are identified: (1) The epicentral region, (2) The Hamgyong mountain range, (3) The Tumen River delta, and (4) The Japan Basin and the seamounts protruding from it. The narrow-band back-projections illuminates different regions. This perhaps has the potential to discriminate between sources of infrasound. We defer this investigation to future studies.

A weak stratospheric vortex occurs twice a year during vernal and autumnal equinox as well as at the onset and recovery of Sudden Stratospheric Warming (SSW) events. During this time the paradigm of classical infrasound propagation paths in the middle atmosphere is challenged. During the 2017 test, the structure of the speed of sound in the atmosphere is mostly attributed to the temperature structure with little direct contribution from wind. However, turbulence and small-scale wave activity enhance during these low-wind conditions increasing the importance of scattering and (partial) reflections and the need for synoptic upper atmospheric specifications.

Although the use of infrasound in the estimation of source depth has been previously discussed, a depth analysis has not been considered here due to the unexpected propagation paths.

3

Long-range atmospheric infrasound propagation from subsurface sources

"To struggle and to understand - never this last without the other."

George Mallory

Abstract In seismology and ocean acoustics, the interface with the atmosphere is typically represented as a free surface. Similarly, these interfaces are considered as a rigid surface for infrasound propagation. This implies that seismic or acoustic waves are not transmitted into the atmosphere from subsurface sources, and vice versa. Nevertheless, infrasound generated by subsurface sources has been observed. In this work, seismo-acoustic modeling of infrasound propagation from underwater and underground sources will be presented. The Fast Field Program (FFP) is used to model the seismo-acoustic coupling between the solid Earth, the ocean, and the atmosphere under the variation of source and media parameters. The FFP model allows for a detailed analysis of the seismo-acoustic coupling mechanisms in frequency-wavenumber space. A thorough analysis of the coupling mechanisms reveals that evanescent wave coupling and leaky surface waves are the main energy contributors to long-range infrasound propagation. Moreover, it is found that source depth affects the relative amplitude of the tropospheric and stratospheric phases, which allows for source depth estimation in the future.

Accepted for publication as: G. Averbuch, J. D. Assink, L. G. Evers (2020), Long-range atmospheric infrasound propagation from subsurface sources, The Journal of the Acoustical Society of America.
Note that minor changes have been introduced to make the text consistent with the other chapters.

3.1 Introduction

Low-frequency acoustic waves, i.e., infrasound, propagate in the atmosphere in a frequency range between 0.01 to 20 Hz. Infrasonic waves in the atmosphere may originate from sources in all geophysical media, such as the solid Earth, the oceans, and the atmosphere. Examples of infrasound sources include underground explosions, earthquakes, and volcanoes [*Campus and Christie*, 2009]. Due to the high impedance contrast, the Earth-atmosphere and ocean-atmosphere interfaces are typically treated as a free surface [*Aki and Richards*, 2002]. Wave physics predicts transmission on the order of the impedance contrast, which is less than one-hundredth of a percent. Moreover, the coupled waves are confined within a narrow cone around the vertical axis, which is defined by the critical angle. Waves propagating at such steep angles do not get trapped in atmospheric waveguides and do not travel over long distances. Therefore, wavefields that are generated in the Earth and oceans are not expected to be detected in the atmosphere. Nevertheless, observations of infrasound signals from underwater and underground sources contradicts this traditional assumption. Such events are known as seismo-acoustic events.

A seismo-acoustic event is an event for which the seismic wavefield in Earth and the acoustic wavefield in the oceans and/or the atmosphere are coupled and have been generated by the same source. *Benioff et al.* [1951] were the first to detect acoustic arrivals caused by an earthquake of unknown magnitude at a distance of 265 km. Following that, infrasonic observations of the 1964 M_w 9 Alaska earthquake have been studied in detail and have been associated with epicentral infrasound [*Bolt*, 1964; *Donn and Posmentier*, 1964; *Mikumo*, 1968] as well as secondary radiation from mountain ranges [*Young and Greene*, 1982]. It was proposed that the infrasound was locally coupled to the atmosphere through the passage of Rayleigh waves.

Vice versa, atmospheric sources can also comprise seismo-acoustics events, as the infrasound waves can readily couple to seismic waves. *Ben-Menahem and Vered* [1975] investigated the generation of seismic waves from atmospheric nuclear explosions. In August 1989, the return of the Columbia space shuttle generated an atmospheric shock wave that coupled to seismic P waves [*Kanamori et al.*, 1991], and in February 2013, the shock wave from the breakup of the Chelyabinsk meteor excited Rayleigh waves that were recorded at distances up to 4000 km [*Tauzin et al.*, 2013].

Since the 1960s, various other studies have focused on the analysis of infrasound associated with earthquakes. Usually, such signals are assigned to the interaction of seismic body waves and surface waves with topographic features at the epicenteral region [*Mutschlecner and Whitaker*, 2005; *Watada et al.*, 2006; *Mikumo et al.*, 2008; *Green et al.*, 2009]. However, efficient coupling also occurs remotely from the source epicenter in sedimentary basins and mountainous areas [*Le Pichon et al.*, 2006; *Marchetti et al.*, 2016; *Shani-Kadmiel et al.*, 2018]. Such coupling may be

observed when propagation paths are efficient from such regions to the observing infrasound array [*Shani-Kadmiel et al.*, 2018]. Thus, different infrasound arrays may observe different regions of efficient coupling [*Le Pichon et al.*, 2006]. In addition, evidence for seismo-acoustic events can also be found in the ionosphere; measurements of perturbations in the ionosphere total electron content have been linked to air-coupled surface waves following large earthquakes [*Artru et al.*, 2004].

Seismo-acoustic events also exist in an Earth-ocean-atmosphere system. In 2004 a M_w 8.1 earthquake near Macquarie Ridge generated infrasound waves that were detected at a distance of 1300 km. The observations could be qualitatively explained by the coupling of seismic to hydroacoustic waves and then to infrasound waves in the atmosphere [*Evers et al.*, 2014]. Such a complex seismo-acoustic event also followed the 2017 North Korean underground nuclear test. Seismic waves from the underground explosion were coupled to infrasound waves in both the Earth-atmosphere and Earth-ocean-atmosphere systems [*Assink et al.*, 2018].

Analytic studies attribute sound transmission through the ocean-atmosphere and Earth-atmosphere interfaces to two primary mechanisms that are frequency and wavenumber dependent. These mechanisms consist of air-coupled surface waves and enhanced transmission of inhomogeneous body waves. However, the effect of these mechanisms has not been investigated regarding long-range sound propagation. The goal of this work is to numerically study the effect of these mechanisms on long-range infrasound propagation from underwater and underground sources.

The paper is organized as follows. Chapter 3.2 provides an overview of the different coupling mechanisms. For convenience, the coupling mechanisms are discussed regarding Earth-atmosphere (solid-fluid) and ocean-atmosphere (fluid-fluid) systems. Nevertheless, the theory holds for any arbitrary solid-fluid or fluid-fluid system. The theory of retrieving the seismo-acoustic wavefield in a horizontally layered media is explained in Chapter 3.3. Numerical investigation of long-range infrasound propagation from subsurface sources is presented in Chapter 3.4 and the conclusions are drawn in Chapter 3.5.

3.2 Coupling mechanism

Coupling of seismo-acoustic energy into the atmosphere happens in both ocean-atmosphere and Earth-atmospheres systems. Efficient coupling is attributed to three types of waves that are associated with different parts of the wavefield spectrum. These waves can be distinguished by their horizontal phase velocity, which is known as trace velocity. The first type is homogeneous P and S waves. These waves consist of relatively high trace velocities, that once in the atmosphere, propagate almost vertically. Consequently, in a horizontally layered system, these waves cannot get trapped in the atmospheric waveguides, therefore having the smallest contribution to long-range infrasound propagation.

The second type is inhomogeneous body waves, which are also known as evanescent waves. These waves have trace velocities that are lower than the medium velocity and therefore have an imaginary vertical wavenumber components, resulting in an exponential decay in amplitude. Let us define k as the source's medium wavenumber, and z_s as the source depth. Theory predicts that for a non-dimensional source depth, kz_s, smaller than one, the interface (ocean-atmosphere or Earth-atmosphere) becomes transparent to the evanescent spectrum; allowing all the evanescent energy to radiate into the atmosphere. Moreover, the emitted pressure field into the air can be up to three orders of magnitude greater than for kz_s larger than one [*Godin*, 2006; *McDonald and Calvo*, 2007; *Godin*, 2008]. The contribution of this mechanism is twofold; besides emitting most of their energy into the air, evanescent waves in the Earth or ocean consist of a large horizontal wavenumber component. Therefore, once in the atmosphere, these waves become oscillatory in the air, get trapped in the atmospheric waveguides, and propagate over hundreds and thousands of kilometers.

The third type is surface waves. Surface waves propagate along the free-surface of an elastic half-space, and they are a linear combination of elastic inhomogeneous body waves [*Rayleigh*, 1885]. In a coupled elastic-acoustic system, combining their solutions with a propagating or evanescent acoustic waves in the acoustic layer give rise to leaky Rayleigh (evanescent-propagating) or Stoneley (evanescent-evanescent) waves, respectively [*Bromwich*, 1898; *Stoneley*, 1926; *Biot*, 1952]. In contrast, Love waves would not contribute to coupled seismo-acoustic waves due to their horizontal polarization. The existence of such waves is determined by the elastic and acoustic properties, i.e., densities and Lamé parameters [*Scholte*, 1947; *Brower et al.*, 1979].

Such waves exist in an Earth-atmosphere system. Ewing and Ben-Menahem studied the generation of Rayleigh waves from atmospheric explosions [*Ewing et al.*, 1957; *Ben-Menahem and Singh*, 1981]. Moreover, *Ewing et al.* [1957] have shown that some of the Rayleigh wave energy can radiated back into the atmosphere. Thus, surface waves generated from an underground source can also radiate acoustic waves into the atmosphere. While this mechanism is less sensitive to the source depth, the vertical angle of propagation in the atmosphere depends on the surface wave velocity v_{surface} and the atmospheric speed of sound c_{air}. For $v_{\text{surface}} \gg c_{\text{air}}$, the radiated wave will propagate vertically upwards. The vertical angle decreases as v_{surface} approaches the atmospheric sound speed, to the limit where the vertical angle is zero. Beyond this angle, for which $v_{\text{surface}} < c_{\text{air}}$, the acoustic wave propagates horizontally and decays vertically; this correspond to a Stoneley wave.

The transparency of the interface also depends on the source type (monopole, dipole, etc.) and the attenuation coefficients in the elastic medium [*Godin*, 2011]. Attenuation changes the behavior of transparency as a function of kz_s, as well as the relative contribution of the different seismic waves to the total emitted energy. Variations in these parameters can result in more than a 20dB difference in the emitted acoustic amplitudes [*Godin*, 2011].

3.3 Retrieving the seismo-acoustic wavefield

Modeling elastic and acoustic wavefields requires solving the elastic wave equation and the linearized fluid dynamics equations. Both sets of equations are based on the conservation of mass, momentum equation, and an equation of state. The elastic equation of motion for the displacement $\boldsymbol{u}$ can be written as [*Achenbach*, 1984]:

$$\rho_0 \frac{\partial^2 \boldsymbol{u}}{\partial t^2} - \nabla \cdot \boldsymbol{\sigma} = 0, \tag{3.3.1}$$

where $\boldsymbol{\sigma}$ is the stress tensor, and ρ_0 is the density. The elastic wave equation can be obtained by combining equation 3.3.1 with the complemented Hooke's law for isotropic media

$$\boldsymbol{\sigma} = \lambda tr(\boldsymbol{\epsilon}) I + 2\mu\boldsymbol{\epsilon}; \quad \boldsymbol{\epsilon} = \frac{1}{2}\Big(\nabla \boldsymbol{u} + (\nabla \boldsymbol{u})^T\Big), \tag{3.3.2}$$

where I is an identity matrix, λ and μ are the Lamé parameters, and $\boldsymbol{\epsilon}$ is the strain. The normal stress relates to the pressure in a fluid media according to $\sigma_{zz} = -p$.

For a moving medium, combining the momentum equation, conservation of mass, and the equation of state can yield the infrasound wave equation. Assuming a horizontally layered lossless atmosphere, where the background parameters vary only in the vertical direction and neglecting wind shear terms, the acoustic wave equation for atmospheric infrasound propagation can be written as [*Brekhovskikh and Godin*, 1999; *Assink et al.*, 2017]:

$$\frac{1}{c^2}\left(\frac{\partial}{\partial t} + \boldsymbol{v}_{0H} \cdot \nabla_H\right)^2 p - \nabla_H^2 p - \rho_0 \frac{\partial}{\partial z}\left(\frac{1}{\rho_0}\frac{\partial p}{\partial z}\right) = 0. \tag{3.3.3}$$

Here $\boldsymbol{v}_{0H} = \boldsymbol{v}_{0H}(z)$ is the horizontal wind component (vertical winds are negligible), ∇_H is the horizontal gradient operator, $\rho_0 = \rho_0(z)$ is the density, and $c = c(z)$ is the adiabatic speed of sound. Assuming an acoustic medium at rest, equation (3.3.3) reduces to the wave equation for ocean acoustics.

Numerous numerical methods provide different solutions to the acoustic and elastic linear wave equations. Solutions of the time-space and frequency-space forms of the wave equation are commonly obtained by using finite-difference [*Kelly and Ward*, 1976; *Tappert*, 1977], spectral methods [*Kosloff et al.*, 1990], finite/spectral elements [*Komatitsch and Tromp*, 1999] and ray methods [*Virieux*, 1986; *Cerveny*, 2001]. Modeling wave propagation in layered media with smooth lateral variations, like the ocean, is usually done by using normal modes [*Pekeris*, 1939] and parabolic-equation [*Tappert*, 1977] methods for solving the frequency-wavenumber (f-k) wave equation.

In order to use the solution for the coupled elastic-acoustic model as suggested by *Schmidt and Tango* [1986], for the coupled atmosphere system, the effective sound

speed approximation is used. In this approximation, the horizontal wind in the direction of propagation is added to the sound speed. The resulting effective sound speed is then used to model atmospheric infrasound propagation. It has been shown (e.g. *Assink et al.* [2017]) that this approximation is sufficient for many applications. Mathematically, the approximation corresponds to the following. In the frequency-(horizontal)wavenumber form of equation (3.3.3), the operator $(\partial/\partial t+\boldsymbol{v}_{0H}\cdot\nabla_H)^2/c^2$ can be written as $(i\omega - i\boldsymbol{k}_H\cdot\boldsymbol{v}_{0H})^2/c^2$. Approximating $\boldsymbol{k}_H \approx \omega\hat{k}_H/c$, where $\hat{k}_H$ is the horizontal direction of propagation, the operator can be approximated by

$$\frac{i\omega}{c}\left(1-\frac{\boldsymbol{v}_{0H}\cdot\hat{k}_H}{c}\right)=\frac{i\omega}{c}\left(\frac{1}{1+\frac{\boldsymbol{v}_{0H}\cdot\hat{k}_H}{c}}\right)+\mathcal{O}(M^2)+...\approx\frac{i\omega}{c+\boldsymbol{v}_{0H}\cdot\hat{k}_H}\equiv\frac{i\omega}{c_{\text{eff}}}. \tag{3.3.4}$$

The effective sound speed, c_{eff}, overestimates the effects of the winds on the propagation. Therefore, this approximation holds for (1) small vertical propagation angles (2) in-plane propagation, and (3) low Mach number, $\text{M} = |\boldsymbol{v}_{0H}|/c$ [*Godin*, 2002; *Waxler*, 2004].

Plugging equation (3.3.4) into the the frequency domain form of equation (3.3.3) yields

$$k_{z,\text{eff}}^2 p+\rho_0\frac{1}{\partial z}\left(\frac{1}{\rho_0}\frac{\partial p}{\partial z}\right)=0. \tag{3.3.5}$$

The vertical wavenumber is defined as $k_{z,\text{eff}}=\sqrt{k_{\text{eff}}^2-k_H^2}$, and $k_{\text{eff}}=\omega/c_{\text{eff}}$. In the case of a dissipative atmosphere, absorption is frequency-dependent, and the winds can cause a Doppler shift to the waves' frequencies. Nevertheless, this effect is small for infrasonic frequencies [*Waxler et al.*, 2017a].

Assink et al. [2017] studied the influence of the effective speed of sound approximation on infrasound propagation in a lossless atmosphere with a maximum Mach number of M=0.4 and horizontal winds up to 97 m/s. It is shown that (1) overestimation of effect of horizontal wind on refraction, leading to underestimates of traveltime and trace velocity. (2) overestimation of the acoustic frequency, leading to small inaccuracies of the estimated absorption. However, for low wind conditions, the influence of this approximation is negligible. In both cases, the amplitudes were not affected by the effective speed of sound approximation.

The Fast Field Program (FFP) solves the Helmholtz equation for a horizontally stratified medium. This method is based on dividing the medium (velocity and density profiles) into small homogeneous layers, while the layers are coupled to each other by explicitly imposing the boundary conditions between them. This allows one to take the influence of an exponentially decreasing density on the acoustic field into account. In addition, it allows one to easily handle discontinuities between solid-fluid, solid-gas, and fluid-gas interfaces as well as providing a direct control over the simulated frequencies and wavenumbers. Therefore, the contribution of the different coupling mechanisms is distinguishable and quantified. In seismology, this

approach is known as the reflectivity method [*Fuchs and Muller*, 1971].

Approximating a piecewise medium of M homogeneous layers with a thickness of 20 m implies that within each layer, $m = 1...M$, the density is constant and the vertical operator in equation (3.3.5) takes the form of $\partial^2/\partial z^2$. Moreover, the relation between the particle displacement and pressure is $w_m = \nabla p_m/\rho_{m0}\omega^2$. Since the density is constant within each layer, the curl of the displacement, w_m, is zero. Therefore the displacement field in the atmosphere can be expressed by an independent potential within each layer.

Following that, in seismo-acoustic modeling the displacement field in each layer can be expressed in terms of a scalar potential for the acoustic medium and a scalar and a vector potential for the elastic medium. These potentials are the basis of the Green's functions of the displacement field. In the case of a homogeneous elastic medium, the wavefield can be decoupled into P-SV and SH motions. These decoupled motions can be expressed by two scalar potentials and one scalar potential, respectively [*Aki and Richards*, 2002]. In this work, we assume the medium to be horizontally stratified, axisymmetric, with coupled elastic-acoustic layers. For such set-up, the SH motion has no contribution to the acoustic wavefield in the fluid layers, and it will be neglected.

Under these assumptions, the displacement field within a layer at a distance r and depth z, in the acoustic medium can be written in cylindrical coordinates as

$$\begin{aligned} u_m^f(r,z) &= \frac{\partial \Phi_m^f}{\partial r} \\ w_m^f(r,z) &= \frac{\partial \Phi_m^f}{\partial z}. \end{aligned} \tag{3.3.6}$$

Accounting only for P-SV motion in the elastic medium, the displacement field within a layer can be written as

$$\begin{aligned} u_m^s(r,z) &= \frac{\partial \Phi_m^s}{\partial r} + \frac{\partial^2 \Psi_m^s}{\partial r \partial z} \\ w_m^s(r,z) &= \frac{\partial \Phi_m^s}{\partial z} - \frac{1}{r}\frac{\partial}{\partial r} r \frac{\partial \Psi_m^s}{\partial r}. \end{aligned} \tag{3.3.7}$$

In equation (3.3.6)the potential Φ_m^f represent the compressional-wave potential, and in equation (3.3.7) the potentials Φ_m^s and Ψ_m^s represent the compressional and shear potentials, respectively. All potentials must satisfy the wave equation. u_m and w_m are the horizontal and vertical displacements, respectively, and suffixes f and s correspond to fluid and solid medium. Hooke's law, which relates stress and strain in an elastic medium, is used to compute the corresponding stress field.

Since the different coupling mechanisms are frequency and wavenumber dependent, solving the wave equation in the f-k domain is beneficial. Defining Λ as an arbitrary potential, the frequency-domain wave equation is known as the Helmholtz

Table 3.1: *Potential types, wavenumber definitions and propagation velocities for the different media. The seismic wave velocities are functions of the density and Lamé parameters. The speed of sound in the ocean depends on the unperturbed pressure and density p_0 and ρ_0, the temperature T, and salinity S. The effective speed of sound in the atmosphere depends on the unperturbed pressure and density, temperature T, and the horizontal winds.*

Wave type	Earth	Ocean	Atmosphere
Compressional	Φ^s $k = \omega/v_p$ $v_p(\rho_0, \lambda, \mu)$	Φ^f $k = \omega/c_{\text{ocean}}$ $c_{\text{ocean}}(p_0, \rho_0, T, S)$	Φ^f $k = \omega/c_{\text{eff}}$ $c_{\text{eff}}(p_0, \rho_0, T, \boldsymbol{v}_{0H})$
Shear	Ψ^s $\tilde{k} = \omega/v_s$ $v_s(\rho_0, \mu)$		

equation $[\nabla^2 + k_m^2]\Lambda_m(r, z) = 0$. Applying the Hankel transform to the Helmholtz equation yields the depth-separated Helmholtz equation

$$\left[\frac{d^2}{dz^2} + k_z^2\right]\Lambda_m(k_r, z) = 0, \tag{3.3.8}$$

where $k_z = \sqrt{k_m^2 - k_r^2}$ is the vertical wavenumber. k_r is the horizontal wavenumber, and k_m is the layer wavenumber. Depending on the medium type in each layer, the potential Λ and the vertical wavenumber k_z will be replaced according to the potentials and propagation velocities presented in Table 3.1. For the elastic layers, solutions of both compressional and shear potentials need to be combined in order to obtain a complete representation of P-SV motion. Moreover, only a combination of both potentials gives rise to surface waves which are significant contributors to the seismo-acoustic wavefield.

Equation (3.3.8) is an ordinary differential equation in the vertical axis, and the solution for each layer is a linear combination of the homogeneous solution $\Lambda_m(k_r, z)$and a particular solution $\hat{\Lambda}_m(k_r, z)$ if a source is present. Exact solutions for equation (3.3.8) can be written in terms of wavenumber integrals. The latter implies that field's exact Green's functions in the f-k domain can be retrieved. Decomposing the solution into up and down going wavefields allows for a straightforward implementation of the boundary conditions (BC) in the numerical solution. Defining A^- and A^+ respectively as the up and down going wavefield amplitudes, the compressional potential solution can be written as $\Phi_m(k_r, z) = A^- e^{-ik_z z} + A^+ e^{ik_z z}$. Its frequency-space domain representation is

$$\Phi_m(r, z) = \int_0^\infty [A^- e^{-ik_z z} + A^+ e^{ik_z z}] J_0(k_r r) k_r dk_r, \tag{3.3.9}$$

and $J_0(k_r r)$ is the Bessel function of the first kind. Similarly, $\Psi_m(r, z)$ is represented

as

$$\Psi_m(r,z) = \int_0^\infty \frac{1}{k_r}[B^- e^{-i\tilde{k}_z z} + B^+ e^{i\tilde{k}_z z}]J_0(k_r r)k_r dk_r. \tag{3.3.10}$$

The $1/k_r$ factor ensures that the two potentials have the same dimensions due to an extra spatial derivative of the shear potential in equation (3.3.7). When $k_r > k_m$ or $k_r > \tilde{k}_m$, the vertical wavenumber of the potentials is imaginary. This part of the spectrum is known as evanescent, and its amplitude decays exponentially with vertical distance. As k_r increases with increasing frequency or decreasing trace velocity, k_z and $\tilde{k}_z$ obtain a larger imaginary value and decay over a shorter distance. This property plays an essential role in the coupling process and affects the emitted infrasonic wave amplitude. This is further discussed in Chapters 3.4 and 3.5.

The potentials' coefficients are obtained using the Direct Global Matrix (DGM) method, which is based on solving the continuity equations for all the interfaces (BC between the layers) as well as the top and bottom BC simultaneously [*Schmidt and Tango*, 1986]. The BC for a solid-solid interface are the continuity of normal and tangential stress and vertical and horizontal displacements. A fluid-fluid interface requires the continuity of normal stress and vertical displacement. Finally, the BC at a solid-fluid interface are the continuity of vertical displacement and normal stress, and the vanishing of the tangential stress. Note that as the shear wavefield is part of both vertical displacement and normal stress, the SV motion contributes to the acoustic field in the fluid layer.

Discrete variations in the medium properties (density and velocity) are handled through the BC. These properties are encompassed in the equations of displacement and stress. The BC at the top and bottom layers can be free surface, rigid surface, or radiation condition. The presented solution allows for an exact implementation of the boundary conditions between the layers. This is in contrast to finite-difference discretization, which is often used in acoustic propagation models. Therefore, one can study the interaction of the wavefields in the different media in a straightforward manner and without any numerical approximations.

In this work, a compressional monopole source is used. The medium response for such a source, in terms of the compressional potential, is

$$\hat{\Phi}(k_r,z) = \frac{S(\omega)}{4\pi}\int_0^\infty \frac{e^{ik_z|z-z_s|}}{ik_z}J_0(k_r r)k_r dk_r, \tag{3.3.11}$$

where z_s is the source depth, and $S(\omega)$ is the frequency-domain source function. Depending on its position, the expressions for the wavefield components can be derived using equations (3.3.6) and (3.3.7), and can be included in the continuity equations in the DGM. Source functions like an S-wave point source and a double-couple force will generate different wavefields and radiation patterns that will affect the radiated pressure field in the atmosphere. For simplicity, this study will use only the compressional monopole source .

The Green's function $\Lambda_m(r,z)$ is obtained after applying the inverse Hankel transform. As the inverse Hankel transform is computationally expensive, this transform is typically replaced in algorithms by the Fast Fourier Transform (FFT). This is an accurate approximation, except for near-field computations or steep propagation angles. Hence, the FFP algorithm gets its name from the use of the FFT algorithm to evaluate the horizontal wavenumber integral. Following [*DiNapoli and Deavenport*, 1980], the discrete form of equation 3.3.9 is

$$\Lambda_m(r_j,z) = dk_r e^{(\epsilon+ik_{min})r_j}\sqrt{\frac{1}{2\pi r_j}}e^{-i\pi/4}\sum_{l=0}^{L-1}[\Lambda_m(k_l,z)e^{ir_{min}ldk_r}\sqrt{k_l}]e^{i\frac{2\pi lj}{L}}, \tag{3.3.12}$$

where L is the number of the discrete wavenumbers and ranges k_l and r_j, respectively. Their corresponding intervals are dk and dr. ϵ is a randomly small value in the order of dk. A detailed explanation can be found in Chapter four of the text book by *Jensen et al.* [2011].

Transforming the Green's functions from frequency-domain to the time-domain yields the wavefield's space-time representation. Considering a set of N frequencies and their corresponding frequency-space Green's functions, a broadband signal can be obtained using Fourier synthesis. That is to say, an inverse FFT (IFFT) is applied to the frequency-domain wavefield, convolved with the frequency-domain source function, $\Lambda_m(r,z,t) = \mathrm{IFFT}[\Lambda_m(r,z,\omega)\cdot S(\omega)]$.

3.4 Numerical examples

■ 3.4.1 Underwater source

Radiation of acoustic waves from an underwater source into the atmosphere involves the coupling of homogeneous and inhomogeneous body waves. Their contribution to long-range infrasound propagation in terms of transmission loss (TL) is investigated with a model that consists of a smooth atmospheric profile above a Munk oceanic profile (Figure 3.1). The TL describes the decrease in the wave intensity, and it is defined as

$$\mathrm{TL} = 10\log_{10}\left(\frac{p(r,z)^2/\rho(z)c(z)}{p_s(r_0,z_s)^2/\rho(z_s)c(z_s)}\right), \tag{3.4.1}$$

where $p_s(r_0,z_s)$ is the pressure produced by the source at a distance of $r_0 = 1$ m and at a depth z_s in unbounded medium. Also, the same definition holds for an underground source as long as a compressional monopole source is used. In case of other source types, the stresses are anisotropic, and a different scaling should be considered [*Frank et al.*, 2013].

A point source is placed at a depth of 1000 m, and its radiation into the atmosphere is simulated for two discrete frequencies. At 50 Hz, the source's distance from the ocean-atmosphere interface is larger than 30 wavelengths ($kz > 1$). The

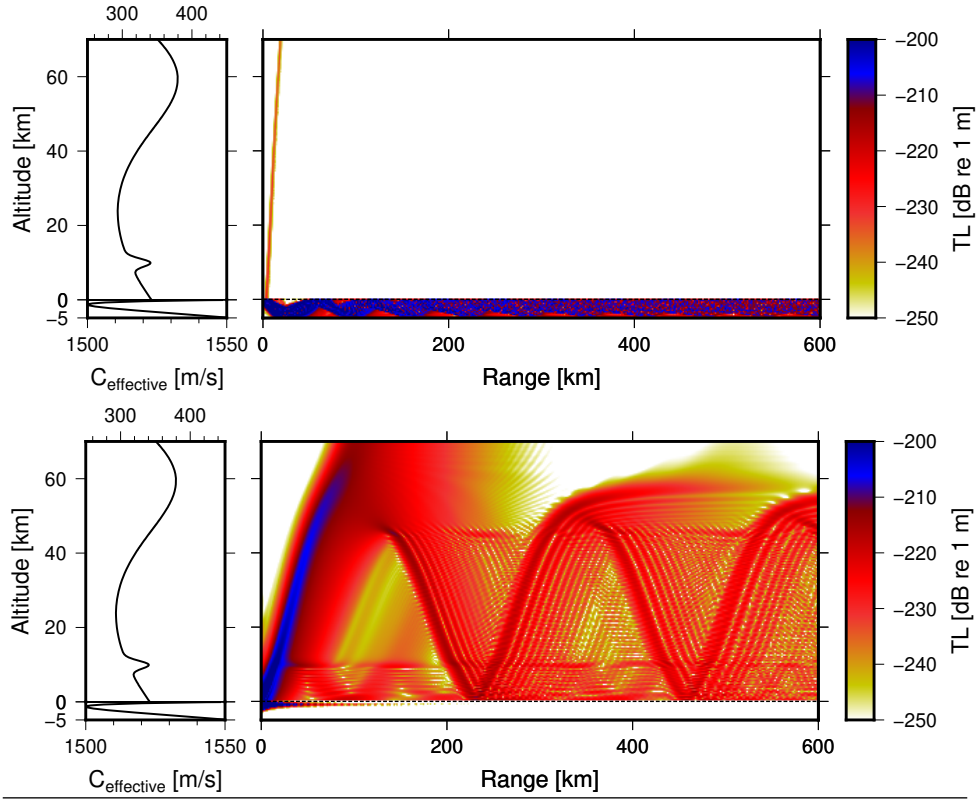

Figure 3.1: *Propagation from an underwater source at a depth of 1000 m. The top frame shows propagation from a 50 Hz source. In the ocean, the waves are bounded by the entire water column as well as being trapped by the SOFAR channel. The radiated wave into the atmosphere corresponds to the direct acoustic wave from the source. Due to its high trace velocity, the wave propagates upwards. The bottom frame shows propagation from a 0.5 Hz source. Due to its low frequency, 1000 m equals a third of a wavelength. For these source parameters, the interface becomes transparent to the evanescent waves, allowing it to get trapped in both tropospheric (10 km) and stratospheric (60 km) waveguides.*

top frame in Figure 3.1 shows the narrowband field from such a source. In the ocean, the propagation is bounded in two waveguides. With its axis at a depth of one kilometer, the Sound Fixing and Ranging channel (SOFAR) is the first waveguide. The second waveguide is the entire water column with its margins at the ocean-atmosphere interface and the ocean bottom. At this frequency, the ocean-atmosphere interface behaves almost as a perfect reflector, preventing most of the acoustic waves from radiating into the atmosphere; only a small fraction of the wavefield, with steep propagation angles, radiates above the source. Due to the exponential decay of the inhomogeneous waves and the high-frequency source, this part of the spectrum decays and vanishes before reaching the atmosphere.

Reducing the simulated frequency to 0.5 Hz, the distance to the ocean-atmosphere interface decreases to half a wavelength ($kz < 1$). For this setup, the interface becomes transparent to the evanescent regime, allowing waves with trace velocities of at least the sound speed at sea level (i.e., 340 m/s) to radiate into the atmosphere. These waves are then trapped in the tropospheric (first 10 km) and stratospheric (between Earth's surface and 50 km) waveguides and propagate over vast horizontal distances (Figure 3.1, lower frame).

Before reaching the atmosphere, the inhomogeneous spectrum of the source undergoes an exponential decay that depends on the source depth and the vertical wavenumber which depends on the trace velocity. Subsequently, both transmitted amplitudes and radiation patterns differ for different source depths. Figure 3.2 shows the effect of the source depth on the transmitted acoustic pressure. An increase in the source depth leads to a decrease in the coupled wave amplitude, and therefore a decrease in TL (Figure 3.2a).

Variations in the radiation patterns due to different source depth are evident when comparing the normalized modal amplitudes. As the source depth increases, the relative amplitudes of the lower trace velocities decrease while the amplitudes of the higher trace velocities increase. This is further detailed by the ratios of the normalized modes (Figure 3.2c). For this particular atmospheric model, the lower trace velocity modes correspond to tropospheric propagation, and the higher trace velocity modes correspond to stratospheric propagation. The exponential decay of the evanescent waves is inversely proportional to the trace velocity. Therefore, the low trace velocity evanescent waves decay faster, and emit waves with lower amplitudes into the atmosphere. Consequentially, higher amplitude waves are trapped in the stratospheric waveguide for deeper sources, when compared to the tropospheric waveguide.

■ 3.4.2 Earth-atmosphere coupling from an underground source

In an Earth-atmosphere system with an underground compressional monopole source, infrasound waves radiate into the atmosphere due to the coupling of inhomogeneous body waves and surface waves. Broadband simulations are used to investigate the effect of the elastic properties and the source depth on the radiated infrasonic waves in the atmosphere. The model consists of either a soft or hard elastic halfspace (Table 3.2) with the same smooth atmospheric profile from Figure 3.1 on top of it. A source is placed at depths of 1000, 1500, and 2000 meters, and a Ricker wavelet with a central frequency of 0.5 Hz is used as a source function.

Figure 3.3 shows the simulated pressure timeseries in the atmosphere (1 km above the interface) from a source at a depth of 1000 m in the hard elastic halfspace. The first visible arrival is the air-coupled surface wave that travels along the interface with a trace velocity of 1800 m/s. After the surface wave, there is a sequence of dif-

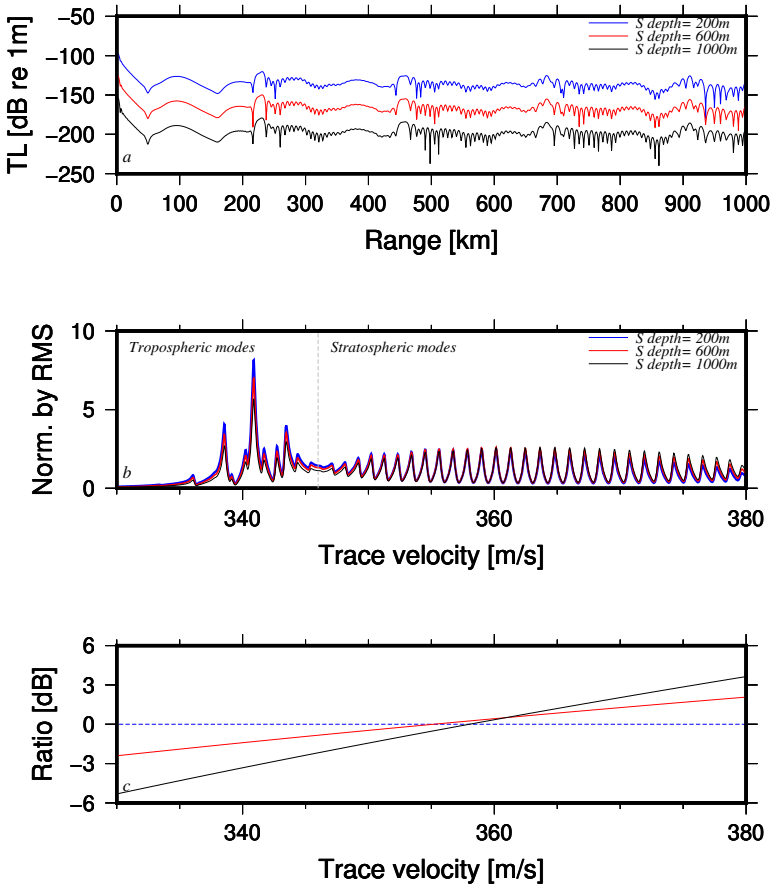

Figure 3.2: *Simulated TL curves and propagating modes above ground for a 0.5 Hz source at different depths. (a) TL values decrease as the source depth increases. (b) The normalized modes show the effect of the source depth on the modal amplitudes. The exponential decay of the evanescent waves is wavenumber dependent. Therefore, waves with lower trace velocities decay faster. This behavior is evident in the increase of the stratospheric modes as the source depth enlarges. The dashed line at 345 m/s represents the transition between tropospheric to stratospheric modes. (c) Ratios of the normalized modal amplitudes (compared to the blue curve) imply that as the source depth increases, the relative stratospheric-phases amplitudes will be higher than the tropospheric ones.*

ferent atmospheric phases. The direct wave that radiates from the source is visible over the first 50 km. Then, the first guided tropospheric arrival appears between 50 to 150 km from the source. At 120 km the second tropospheric bounce arrives, and at 220 km the first stratospheric arrival appears. At further distances, the atmospheric arrivals consist of two tropospheric and two stratospheric phases. A zoom-in to such arrivals is shown in the boxed signal. It shows two tropospheric (I_w)

and two stratospheric (I_s) signals. The small wiggle leading the first stratospheric arrival is a result of horizontal propagation across the Earth-atmosphere interface (diving wave or refracted wave). An f-k analysis reveals two main branches with trace velocities of 1800 m/s and 330-400 m/s. These branches correspond to the surface wave and the inhomogeneous body waves, respectively (Figurte 3.3, right frame). A faint branch that corresponds to a trace velocity of 5000 m/s represents the coupling from the homogeneous P wave. As predicted, the homogeneous P wave has the smallest contribution to the atmospheric perturbations due to the high density and velocity contrast.

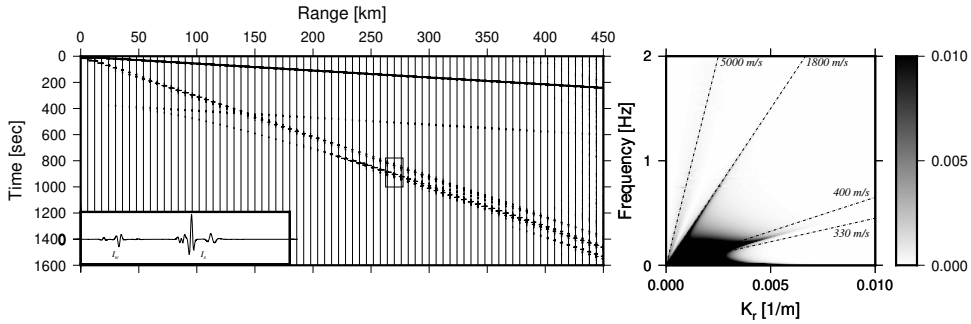

Figure 3.3: *Synthetic pressure timeseries. Broadband simulation for a source at a depth of one kilometer with a central frequency of 0.5 Hz in the hard bottom. The first arrivals correspond to the air-coupled surface wave with a trace velocity of 1800 m/s. Following it are the first tropospheric refractions in the range of 50-150 km, and second tropospheric refractions between 120 and 250 km. The first stratospheric refraction appears at approximately 220 km after the tropospheric phases. A zoom-in on the boxed signal reveals a signal that consists of two tropospheric (I_w) and two stratospheric (I_s) phases .Right: f-k plot shows the dispersion relation of the propagating waves in the atmosphere. Coupling from the direct P wave from the source is barely not visible (branch of 5000 m/s). The 1800 m/s branch represents the air-coupled surface wave, and the 300-400 m/s cone shows the amplitudes of the coupled evanescent waves.*

Simulation for a source in a soft bottom show a better coupling to the atmosphere (Figure 3.4). Beside having stronger amplitudes, the main difference is the lower surface wave velocity. Coupling from a slower elastic layer may result in air-coupled surface waves also getting trapped in the atmospheric waveguides. This mechanism may explain the observed secondary infrasound source in sedimentary basins [*Shani-Kadmiel et al.*, 2018; *Assink et al.*, 2018]. Accounting for viscoelastic attenuation will change the relative coupled amplitudes from evanescent and surface waves. While the general trend is a reduction of the signals' amplitudes, surface waves will experience a faster decay than body waves. The effect on the coupled acoustic signal in the atmosphere is modeled for a sample scenario in the Appendix D

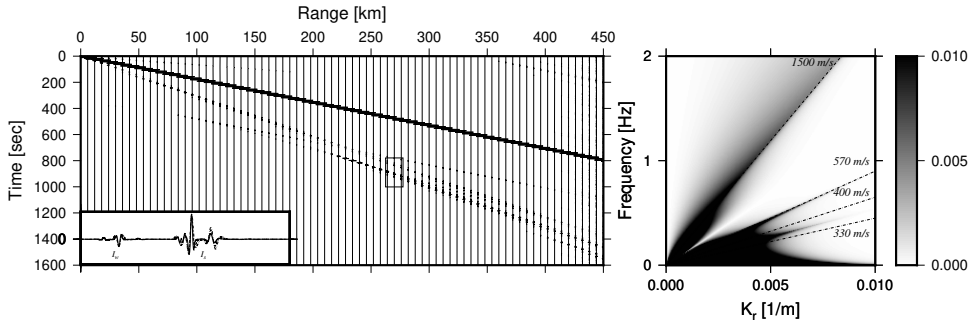

Figure 3.4: *Synthetic pressure timeseries. Broadband simulation for a source at a depth of one kilometer with a central frequency of 0.5 Hz in the soft bottom. The direct P wave (branch of 1500 m/s) is prominent for frequencies up to 2 Hz. Higher amplitudes of the surface wave (570 m/s branch) and the coupled inhomogeneous waves are also apparent.*

Following the analysis of the modes in Figure 3.2, the effect of the source depth is demonstrated in Figure 3.5. As the source depth increases, the relative amplitude of the second stratospheric phase, which corresponds to higher trace velocity, increases compared to the other atmospheric phases. The different acoustic partitioning in the atmosphere is a consequence of the exponential decay of the evanescent waves in the elastic layers.

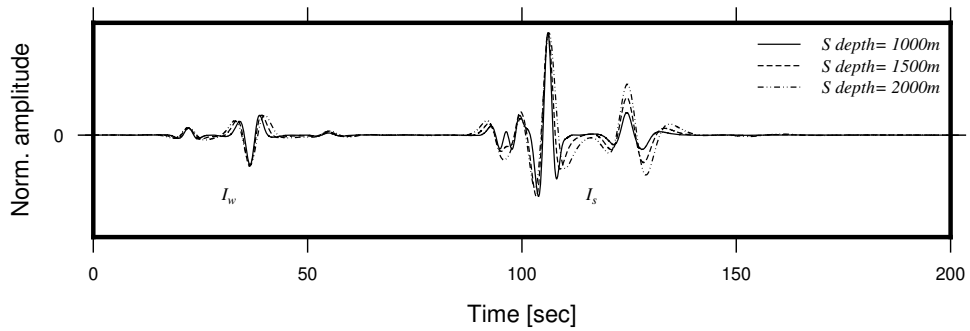

Figure 3.5: *Comparison of the normalized signals arriving at 270 km (boxed signal Fig. 3.4) for different source depths. It shows that as the source depth increases, the relative amplitude of the second stratospheric phase increases compares to the other phases. Such behavior agrees with the modal analysis in Fig. 3.2 and the theoretical predictions of Godin [2006].*

With the new understandings of the Earth-atmosphere coupling mechanisms, let us re-examine the detected signals from 12 February 2013 and 6 January 2016

North Korean underground nuclear tests. *Assink et al.* [2016] (Figure 4) detected three infrasound phases from the 2013 test, and one phase from the January 2016 test. The three prominent phases are associated with tropospheric propagation (I_w), stratospheric propagation (I_s), and a combined propagation path (I_{ws}). On the other hand, in 2016, a weak signal was detected, and it was not possible to determine the nature of its propagation. It was postulated that a combination of unfavorable propagation condition and a deeper source during the 2016 test are the reason for the weak signal. While further exploring the conclusions of that study, the influence of the source depth can now be deduced in more detail. Considering a deeper source and the exponential decay of the evanescent waves, the amplitude of the coupled signal in 2016 was one order of magnitude weaker than on 2013. Such decay levels the signal's amplitude with the background noise. Moreover, the radiation pattern from deeper sources makes it more likely that the observed signal was a stratospheric phase.

Table 3.2: *Rock properties used in the calculation of the coupled fields for a soft and hard bottom.*

Elastic medium	$\rho\ [kg/m^3]$	$V_p[m/s]$	$V_s[m/s]$
Soft	1900	1500	600
Hard	2700	5000	2000

3.5 Summary and discussion

Observations of long-range infrasound signals originated from underwater and underground sources contradict the usually considered free surface behavior of the ocean-atmosphere and Earth-atmosphere interfaces, which implies almost total reflection. While wave propagation in solids, fluids and solid-fluid systems has been well studied, long-range infrasound propagation from subsurface sources is not yet well understood. In this work, coupling mechanisms are proposed and studied regarding long-range infrasound propagation. The presented results are essential for the understanding of the complex infrasound signals originating from seismo-acoustic events.

The Fast Field Program (FFP) is used to model the seismo-acoustic coupling between the solid Earth, the ocean, and the atmosphere under the variation of source depth and frequency, and properties of the subsurface and atmospheric conditions. Modeling in the $f-k$ domain provides a convenient way to distinguish between the different coupling mechanisms and study their contribution to the acoustic wavefield in the atmosphere. Results show the important role of evanescent coupling between the Earth, ocean, and the atmosphere and the ability of the emitted waves to get trapped in the atmospheric waveguides and propagate over vast distances. Evanes-

cent waves with low trace velocities decay faster than ones with high trace velocities. The differences in the decay rate lead to an inhomogeneous radiation pattern in the atmosphere, which leads to different acoustic partitioning in the atmospheric waveguides. Therefore, for the same atmosphere and different source depths, the relative amplitudes of the atmospheric phases will change. Particularly, as the source depth increases, the relative amplitudes of the higher trace velocity phases are larger than the lower trace velocity phases.

In the Earth-atmosphere system, surface waves have a significant contribution to the acoustic radiation into the atmosphere. Nevertheless, the radiated waves do not necessarily get trapped and propagate in the atmospheric waveguides. The propagation direction of the coupled surface waves in the atmosphere depends on the atmospheric sound speed relative to the surface wave velocity. Therefore, only surface waves with trace velocities in the order of the atmospheric sound speed profile will enable the radiated waves to get trapped in the atmospheric waveguides.

The presented study assumes a horizontally layered medium to reduce complexity and understand the underlying mechanisms of seismo-acoustic coupling. Although it provides essential insights into the effect of the coupling mechanisms on long-range infrasound propagation, it cannot accurately simulate events in a range dependent medium and with topographic features. Nevertheless, some conclusions on different setups can be derived. For example, the presence of a region with a low seismic velocity can lead to contribution of surface waves to long-range infrasound propagation.

The inhomogeneous radiation from underwater and underground sources brings up the question, how much information about the subsurface or underwater source can be retrieved. The effect of a different source depth on the atmospheric wavefield has been shown. However, the inverse problem regarding the source intensity, depth, and mechanism remains a challenge. Moreover, the interaction with complex topography and range dependent profile, and the influence of absorption will be subject of future research.

4

Probabilistic inversion for submerged source depth and strength from infrasound observations

"The mind is the most important muscle."

Wolfgang Güllich

Abstract In seismology, the depth of a near-surface source is hard to estimate in the absence of local stations. The depth-yield trade-off leads to significant uncertainties in the source's depth and strength estimations. Long-range infrasound propagation from an underwater or underground source is very sensitive to variations in the source's depth and strength. This characteristic is employed in an infrasound based inversion for the submerged source parameters. Firstly, a Bayesian inversion scheme is tested under the variations of the number of stations, the signals frequency band, and the signal-to-noise ratio (SNR). Secondly, an ensemble of realistic perturbed atmospheric profiles is used to investigate the effect of atmospheric uncertainties on the inversion results.

Results show that long-range infrasound signals can be used to estimate the depth and strength of an underwater source. Using a broadband signal proved to be a fundamental element to obtain the real source parameters, whereas the SNR was secondary. Multiple station inversions perform better than one-station inversions; however, variations in their position can lead to source strength estimations with

Published as: G. Averbuch, R. Waxler, P. S. M. Smets, L. G. Evers (2020), Probabilistic inversion for submerged source depth and strength from infrasound observations, The Journal of the Acoustical Society of America, 147 (2), 1066-1077, doi.org/10.1121/10.0000695
Note that minor changes have been introduced to make the text consistent with the other chapters.

uncertainties up to 50%. Regardless of the number of stations, their positions, and SNRs, all of the estimated depths were within 10% from the real source depth.

4.1 Introduction

Since the 1940's, efforts have been made to study the acoustic and seismic response of explosions [*Sharpe*, 1942a,b; *Carpenter*, 1967; *Holt*, 1977]. Experimental, analytical, and numerical tests showed the effect of the explosion medium [*Werth and Herbst*, 1963], yield [*Carpenter*, 1967], and depth [*Mueller and Murphy*, 1971a,b] on the recorded seismic waves. Moreover, analytic and empirical methods have been developed to differentiate underground explosions from natural seismic activity as well as to estimate the explosion's source parameters, i.e., yield and depth. These methods are based on separating the different phases and estimate their time differences and relative amplitude ratios [*Douglas et al.*, 1972; *Sykes and Wiggins*, 1986; *Kafka*, 1990; *Kim et al.*, 1993; *Walter et al.*, 1995; *Bowman*, 2019]. A depth-yield trade-off curve [*Rougier et al.*, 2011] usually links the explosion's source parameters. Consequently, an accurate estimation of one parameter provides the other.

The ability to separate the phases depends on the source depth and the recorded signal. For example, to distinguish between the direct P arrival and its free-surface reflection, Pp/s, their periods must be shorter than twice the travel time between the source and the Earth's surface. Therefore, for shallow sources, a common requirement is the presence of local or regional seismic stations. At these distances, the required high-frequency components (that correspond to short periods) are preserved, allowing to distinguish between the phases and making the source parameter estimation possible. In contrast, the low-frequency content that is recorded at teleseismic distances averts a proper separation of the phases, thus preventing an accurate estimation of the source parameters. The non-unique solution (depth-yield trade-off curve) and the uncertainties of the parameters lead to a broad spectrum of source parameter values.

Underground and underwater sources can also radiate low-frequency acoustic waves into the atmosphere. These waves are known as infrasound, and they can be trapped in the atmospheric waveguides and propagate over vast distances. Long-range infrasound signals from subsurface sources are usually attributed to earthquakes in an Earth-atmosphere [*Benioff et al.*, 1951; *Donn and Posmentier*, 1964; *Watada et al.*, 2006] and Earth-ocean-atmosphere system [*Evers*, 2014], as well as to underground nuclear explosions [*Assink et al.*, 2016]. Seismic waves can be coupled into the atmosphere at the source epicenter (epicentral infrasound), at different regions along the seismic propagation path (secondary infrasound), and locally at the infrasound array due to ground-coupled air-waves [*Shani-Kadmiel et al.*, 2018; *Assink et al.*, 2018]. Besides underwater and underground sources, infrasonic signals can be generated by natural and anthropogenic events; for example, explosions, ocean waves, and volcanic eruptions [*Campus and Christie*, 2009].

The coupling of acoustic and seismic waves to infrasonic waves is associated with three types of waves that can set apart by their trace velocity (horizontal phase velocity). In an Earth-atmosphere and ocean-atmosphere systems, the first type of

waves is homogeneous P and S waves (body waves). Due to their relatively high trace velocities, the radiated waves propagate almost vertically upwards, and cannot get trapped in the atmospheric waveguides. Therefore, their contribution to long-range infrasound propagation is minimal. The second type is inhomogeneous P and S waves. Their low trace velocity leads to a large horizontal wavenumber component and an imaginary vertical wavenumber component. As a result, these waves experience an exponential decay in amplitude between the source and the ocean/earth interface with the atmosphere. However, once in the atmosphere, they can propagate horizontally, get trapped in the atmospheric waveguides, and travel over hundreds or thousands of kilometers. Theory predicts that for a source in a distance of less than one acoustical wavelength from the interface with the atmosphere, the interface becomes transparent to the evanescent energy, meaning that all the evanescent energy can radiate into the atmosphere [*Godin*, 2006; *McDonald and Calvo*, 2007; *Godin*, 2011]. Moreover, it was shown that variation in the source depth leads to different radiation patterns in the atmosphere as well as changes in the total coupled energy [*Godin*, 2006; *McDonald and Calvo*, 2007].

The third type of waves is surface waves, and it exist in an Earth-atmosphere system. Depending on the Earth and atmosphere elastic and acoustic properties, surface waves can be recognized as leaky Rayleigh or Stoneley waves [*Biot*, 1952; *Scholte*, 1947]. The surface wave velocity determines the direction of propagation in the atmosphere. For high surface wave velocity, the radiated wave will have a small horizontal wavenumber component; hence, it will propagate vertically upwards. As the surface wave velocity decreases, the horizontal wavenumber component of the radiated wave increases, allowing the coupled wave to propagate horizontally and get trapped in the atmospheric waveguides. Analytical studies show that for a horizontally layered medium, inhomogeneous body waves and surface waves are the main contributors to the acoustic perturbations in the atmosphere with amplitudes up to three orders of magnitudes larger than from homogeneous body waves [*Godin*, 2006; *McDonald and Calvo*, 2007; *Godin*, 2011].

The sensitivity of the coupled wave's amplitude to the source parameters leads us to the hypothesis that long-range infrasound signals can be used to invert for the underwater or underground source parameters. *Assink et al.* [2016], made the first step and used infrasonic signals from the 2013 and 2016 North Korea's underground nuclear tests to evaluate the relative source depth. Here, the prospect of an infrasound-based inversion, which extracts the submerged source's absolute depth and strength is tested numerically. Inversion schemes in geophysics are a common practice for estimating an unknown set of parameters from observations [*Tarantola*, 2005]. They can be found in seismic tomography [*Tromp et al.*, 2005], seismic wavefield reconstruction [*Maranò et al.*, 2012], explosion yield estimation [*Kim and Rodgers*, 2016; *Bowman*, 2019], and evaluation of atmospheric properties [*Lalande et al.*, 2012; *Assink et al.*, 2013]. Although it is used in different fields, the philosophy is similar: assuming a set of observations $\boldsymbol{M}$, model parameters $\boldsymbol{m}$, and a forward model G, one should find the model parameters that minimize the

function $\|\boldsymbol{M} - G(\boldsymbol{m})\|$.

The remainder of the paper concentrates on answering the following question: given an observed signal $\boldsymbol{M}$, what are the submerged source's depth (z_s) and strength (S)? Our hypothesis is based on the sensitivity of the coupled evanescent body waves to variations in the source characteristics. This behavior belongs to both seismic and acoustic evanescent body waves[*Godin*, 2006, 2011]. Therefore, although this study focuses on submerged sources, the presented results can be useful also to subsurface sources. Chapter 4.2 describes the probabilistic inversion scheme as well as the Fast Field Program (FFP), which is the numerical model used to generate both "observed" signals and the data set for the inversion scheme. Assuming a known atmospheric profile, Chapter 4.3.1 shows the effect of the signal's frequency band, number of stations, and SNR on the inversion results. Then, in Chapter 4.3.2, the effect of atmospheric uncertainties is investigated. The paper is concluded with a summary and a discussion of the results.

4.2 Method

Before diving into the inversion scheme, the possibility of overcoming the depth-yield trade-off needs to be investigated. The FFP [*Schmidt and Tango*, 1986] is used to simulate the acoustic pressure in the atmosphere from a submerged source at different depths and with different strengths. It provides an exact solution for wave propagation in a 2D horizontally layered media in the f-k domain by solving the continuity equations for all interfaces. These equations comprise the continuity of normal stress (pressure) and vertical displacement. The explicit treatment of the boundary conditions allows handling variations in speed of sound and density profiles as well as stark discontinuities, such as the ocean-atmosphere interface, without numerical approximations (unlike finite-difference discretization). Both media are divided into 20 m homogeneous layers, and each layer is attributed with speed of sound and density values which correspond to the layer altitude. Atmospheric winds are integrated by the effective sound speed approximation, C_{eff}, which is defined as the sum of the adiabatic speed of sound and the wind component in the direction of propagation [*Godin*, 2002]. The source is set to a monopole volume injection, and the Fast Fourier Transform is used to reconstruct the frequency space pressure field.

Figure 4.1 shows the transmission loss of eastward propagation (90 degrees) in the atmosphere for a 0.5 Hz source at a depth of 500 m. The atmospheric profile consists of tropospheric and stratospheric waveguides at 10 and 50 km, respectively, and the depth of the oceanic layer is five kilometers. The simulated trace velocities, which indicates the wavenumbers, range from 300 m/s to 450 m/s and is kept fixed through the remainder of this study. Due to the low-frequency contents of the source, the interface becomes transparent to the evanescent waves, allowing it to get trapped in both waveguides and efficiently propagate over vast distances. For this atmospheric profile, the tropospheric waveguide encompass low trace velocity

modes (<345 m/s), and the stratospheric waveguide encompass high trace velocity modes.

The effects due to variations of the source depth and strength on the atmospheric perturbations are demonstrated in Figure 4.2. Although different source parameters may yield similar pressure curves (row (A), blue and red lines), the ratios of the curves (a/b, b/c, d/e, and e/f) within each set are different (row (B)). There is a linear relation for the source strength and a non-linear relation for the source depth. Row (C) shows the normalized modes above ground, for a 0.5 Hz source. An increase in the source depth leads to a relative decrease in the lower trace velocity amplitudes compared to the higher trace velocity amplitudes. This behavior is further emphasized by the ratios of normalized modes in row (D). Such variations imply that the radiation pattern in the atmosphere depends on the source depth. In contrast, there are no variations in the normalized modes due to changes in the source strength. It means that a linear scalar, as strength, cannot adequately compensate for a different source depth. Therefore, the use of infrasonic signals to distinguish between different underwater source parameters is feasible.

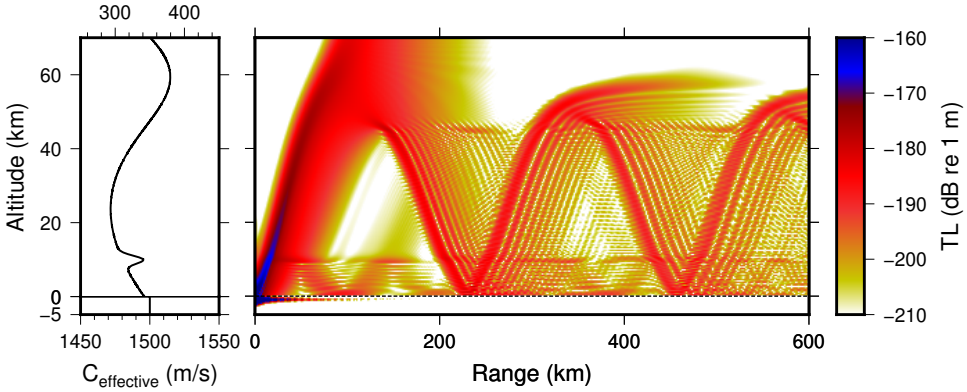

Figure 4.1: *Infrasound propagation from an underwater source at a depth of 500 m and a 0.5 Hz source.*

The linear effect of the source strength in Figure 4.2 is a direct consequence of the linear FFP model. However, the non-linear impact of the variation in the source depth is less intuitive. Let us define v and v_{tr} as the medium's acoustic velocity and modeled trace velocity, respectively. The corresponding medium's wavenumber is $k = 2\pi f/v$, horizontal wavenumber is $k_r = 2\pi f/v_{tr}$, and vertical wavenumber is $k_z = 2\pi f\sqrt{1/v^2 - 1/v_{tr}^2}$. Propagation between the source to the ocean-atmosphere interface is proportional to $Ae^{ik_z z}e^{ik_r r}$. Assuming that the coupling is predominantly due to inhomogeneous waves ($v_{tr} < v$), $k_z = i\hat{k}_z$, and the source-to-interface propagation can be written as $Ae^{-\hat{k}_z z}e^{ik_r r}$. The function $e^{-\hat{k}_z z}$ is a real decaying

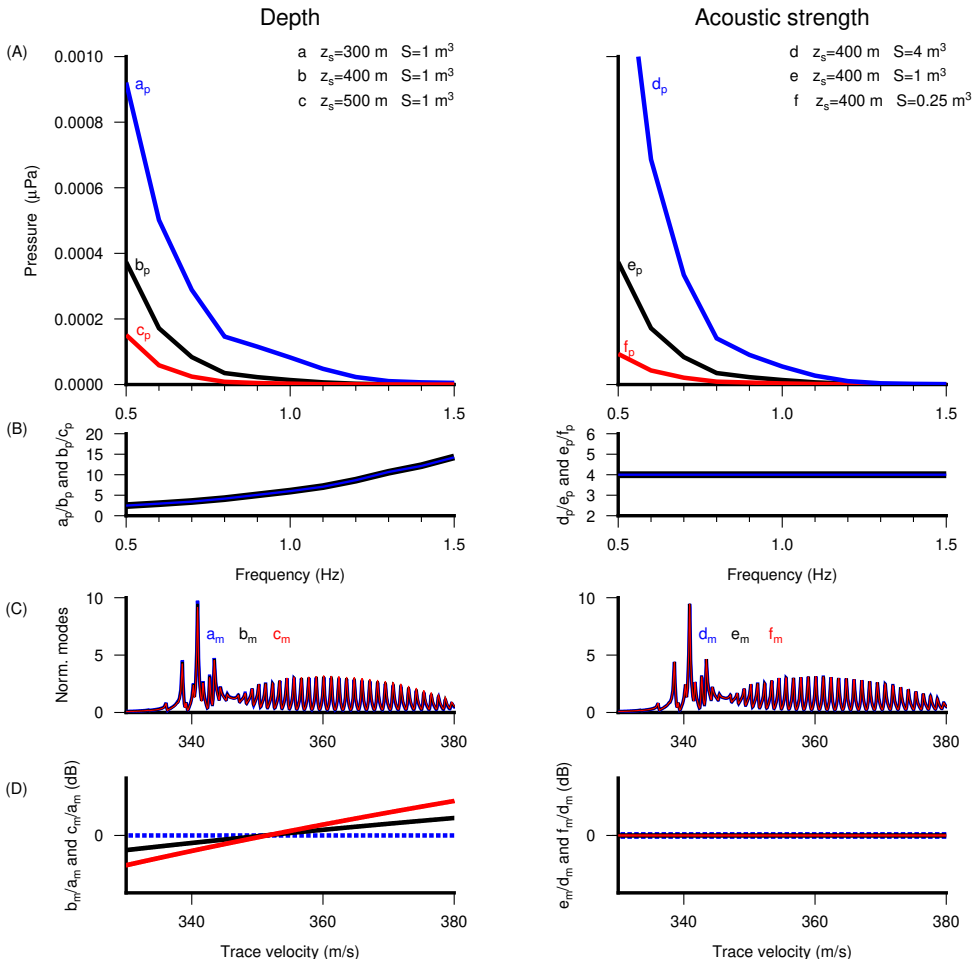

Figure 4.2: *Changes in the atmospheric pressure perturbations due to variations in the source parameters The left column shows the effect of the source depth on the simulated pressure, and the right column shows the effect of the source strength on the simulated pressure. Subscripts p and m correspond to pressure and normalized modes by RMS, respectively. Row (A) shows atmospheric discrete frequency pressure curves 300 km from the source for different source parameters. Row (B) shows the ratios of the curves in the upper frames,e.g., the pressure of curve a for 1 Hz divided by the pressure of curve b for the same frequency. Row (C) shows the normalized, propagating modes for a 0.5 Hz source, and row (D) shows the ratio of the normalized modes (relative to the red curve).*

,

function and it explains the non-linear relation due to variations in the source depth (Figure 4.2, rows (A) and (B)). Also, different trace velocities correspond to differ-

ent vertical wavenumbers $\hat{k}_z$. As a result, for a fixed frequency, the decay rate of the modeled trace velocities differ from one to another, leading to variations in the radiation pattern in the atmosphere due to changes in the source depth (Figure 4.2, rows (C) and (D)).

Bayesian inversions are used in a wide range of physical problems when a parameter space needs to be evaluated from a set of observations [*Tarantola*, 2005]. It provides a rigorous probabilistic framework that combines a priori knowledge on the parameter space and a set of observations into a posterior probability distribution as a function of the free parameters. Here, a probabilistic Bayesian inversion scheme is used to estimate the source parameters from a set of observed signals. The Bayesian formulation of our original question is $P(z_s, S|\boldsymbol{M})$, where P is the probability density function.

A synthetic data set, $m(z_s, r_i, \theta_j, \omega_k, S)$, of the acoustic pressure perturbation on ground level ($z = 0$ m) is generated by the FFP for a range of source depths, z_s, ranges, r_i, directions of propagation, θ_j, frequencies, ω_k, and source strengths, S. The motivation to use discrete frequencies and not absolute travel times, as in seismology, is purely due to numerical costs. Due to the stark contrast of densities and acoustic velocities, fast methods to compute travel times, like ray tracing, cannot be used. Therefore, in order to obtain travel times from an underwater source, one must use a full-wave model either in the time domain or compute it for a large number of frequencies in the frequency domain. These simulations are numerically expensive. It will be shown that accurate results can be obtained by using a selection of discrete frequencies and avoid simulating an entire time series. Moreover, higher accuracy can be easily obtained by adding more frequencies with a low numerical cost.

After choosing certain values for the source depth and strength, the observations, $M(r_i, \theta_j, \omega_k)$ are obtained by adding noise to the synthetic data as follows:

$$M(r_i, \theta_j, \omega_k) = m(z_s, r_i, \theta_j, \omega_k, S) + \mathrm{N}, \quad \mathrm{N} \sim \mathcal{N}(\mu = 0, \sigma^2(\mathrm{SNR})). \tag{4.2.1}$$

Where N is a randomly added noise from a normal distribution with a zero mean (μ), and a variance (σ) that is defined by the SNR.

In order to calculate the Bayesian probability of a given z_s and S, their probability distributions, $p(z_s)$ and $p(S)$, and the variance of the cost function need to be evaluated. $p(z_s)$ and $p(S)$ are assumed to be piecewise constant functions defined as:

$$\begin{aligned} p(z_s) &= \begin{cases} \frac{1}{(z_{max} - z_{min})/dz} & z_{min} < z < z_{max}. \\ 0 & \text{elsewhere.} \end{cases} \\ p(S) &= \begin{cases} \frac{1}{(S_{max} - S_{min})/dS} & S_{min} < S < S_{max}. \\ 0 & \text{elsewhere.} \end{cases} \end{aligned} \tag{4.2.2}$$

Here, z_{min}, z_{max}, S_{min},and S_{max} represent the boundaries of the searching range.

Their corresponding increments are dz, and dS. Equation (4.2.2) means that the occurrence probabilities of the parameters within the searching range are equal. The variance of the cost function, $\sigma(r_i, \theta_j, \omega_k)$, is the same variance defined by the SNR in equation 4.2.1. In practice, this assumption is valid since SNR values are evaluated continuously as part of the data analysis [*Melton and Bailey*, 1957; *Averbuch et al.*, 2018].

Given a set of observations $M(r_i, \theta_j, \omega_k)$ and synthetic data set $m(z_s, r_i, \theta_j, \omega_k, S)$, the probability that a source was in a certain depth z_s and strength S is:

$$P(z_s, S|M(\boldsymbol{r}, \boldsymbol{\theta}, \boldsymbol{\omega})) = \frac{p(z_s)p(S)e^{-\sum_{i,j,k} \frac{1}{2\sigma(r_i,\theta_j,\omega_k)^2} \|M(r_i,\theta_j,\omega_k) - m(z_s,r_i,\theta_j,\omega_k,S)\|^2}}{\int_{S_{min}}^{S_{max}} \int_{z_{min}}^{z_{max}} p(z)p(S)e^{-\sum_{i,j,k} \frac{1}{2\sigma(r_i,\theta_j,\omega_k)^2} \|M(r_i,\theta_j,\omega_k) - m(z_s,r_i,\theta_j,\omega_k,S)\|^2} dz dS}. \tag{4.2.3}$$

This posterior probability is calculated for each possible combination of source depths and strengths. The integration of the likelihood function over the entire search range, as in the denominator, acts as a normalization function. It ensures that the sum over all probabilities will be unity. The trapezoidal rule is used to evaluates the double integral.

The accuracy of the inversion is tested under the variation of the number of stations, source depth, frequency range (number of discrete frequencies), and SNRs. The experiment starts with a broad station coverage, where the effect of the frequency band is investigated. Then, the number of stations is reduced until attaining a one-station inversion. For this part, a known atmospheric profile is used. Finally, the influence of atmospheric uncertainty is tested by using an ensemble of 25 realistic perturbed atmospheric profiles provided by the European Center for Medium-Range Weather Forecasts (ECMWF).

4.3 Results

■ 4.3.1 Number of stations vs frequencies.

Here, we estimate the effects of the number of stations, frequency range, and SNR on the inversion results. In order to reduce the uncertainties of the problem, a known, smooth atmospheric profile is used. The idealized profile consists of a tropospheric (10 km) and a stratospheric (50 km) duct with varying strength as a function of the propagation azimuth. Defining zero degrees as the north, the strengths of the ducts increase easterly. Table 4.1 shows the modeling parameters used for generating the data, and the search ranges in the inversion scheme were set to all of the modeled depths and strengths. The parameters dz, $d\theta$, df, and dS represent the increments size within the ranges z, θ, f, and S, respectively.

To demonstrate the feasibility of the inversion, a ten-station, and ten-frequency inversion is used (the position of the stations is shown in Appendix E.1). From each azimuth of propagation, two ranges were chosen according to the atmospheric ducts to ensure that signals arrive at all stations. The calculated probabilities for the different source depths are presented in Figure 4.3. Besides one inversion (SNR = 1 for $z_s = 1200$ m), all of the inversion results provided accurate results for the source depth. As the SNR decreases, the uncertainty of the source depth increases. However, it is always bounded within a ± 60 m range. Most of the source strength estimations are within a range of ± 0.05 m^3, which is less than a 5% error. This small deviation can be attributed to the randomly added noise. For SNR=1, the uncertainty of the depth and strength increases, and a depth-yield trade-off relation appears in a ridge-like form. Throughout this section, the observation's source parameters are set to $z_s = 1000$ m, and $S = 1$ m^3.

Statistics from 1000 realizations are used to estimate the impact of the number of frequencies, number of stations, and SNRs on the inversion results. The observations are set according to equation (4.2.1), and the source parameters with the highest probability are extracted. The first inversion test is set to estimate the effect of the frequency range. Figure 4.4 shows the distribution of the 1000 source parameters from a ten-station inversion for a single (discrete) frequency. For the source depth, the medians are either accurate or very close to its real value, and the 25 and 75 percentiles are bounded between 20 m to 100 m from it. Medians of the source strength provide a good estimation as well. However, there is a distinct skewness of the source strength distribution around its median, and the 25 and 75 percentiles are bounded between 0.5 m^3 to 2.7 m^3 from it. Results from the combined three-frequency inversions accurately resolve both depth and strength for all SNRs while minimizing the variance range. Table E.1 in Appendix E.2 contain the number of outliers presented in Figure 4.4

Using multiple frequencies provides more constraints for the inversion, therefore, improving the accuracy as well as reducing their variance. Acquiring more discrete frequencies depends only on the signal and its sampling rate. However, recordings from multiple stations are not always available. Results of ten frequencies and ten-, five-, and a single-station inversions show almost no difference in the estimated depth (Figure 4.5). Nevertheless, the approximated source strength is sensitive to the number of stations and SNR. The variance of the one station inversion increases with the decrease of SNR, and the peaky distributions of the higher SNRs lead to a high number of outliers (Table E.2 in Appendix E.2).

Table 4.1: *Modeling parameters for the smooth atmospheric profiles.*

z [m]	dz [m]	θ [deg]	$d\theta$ [deg]	f [Hz]	df [Hz]	S [m^3]	dS [m^3]
200-1000	20	10-90	20	0.5-1.5	0.1	0.2-3	0.002

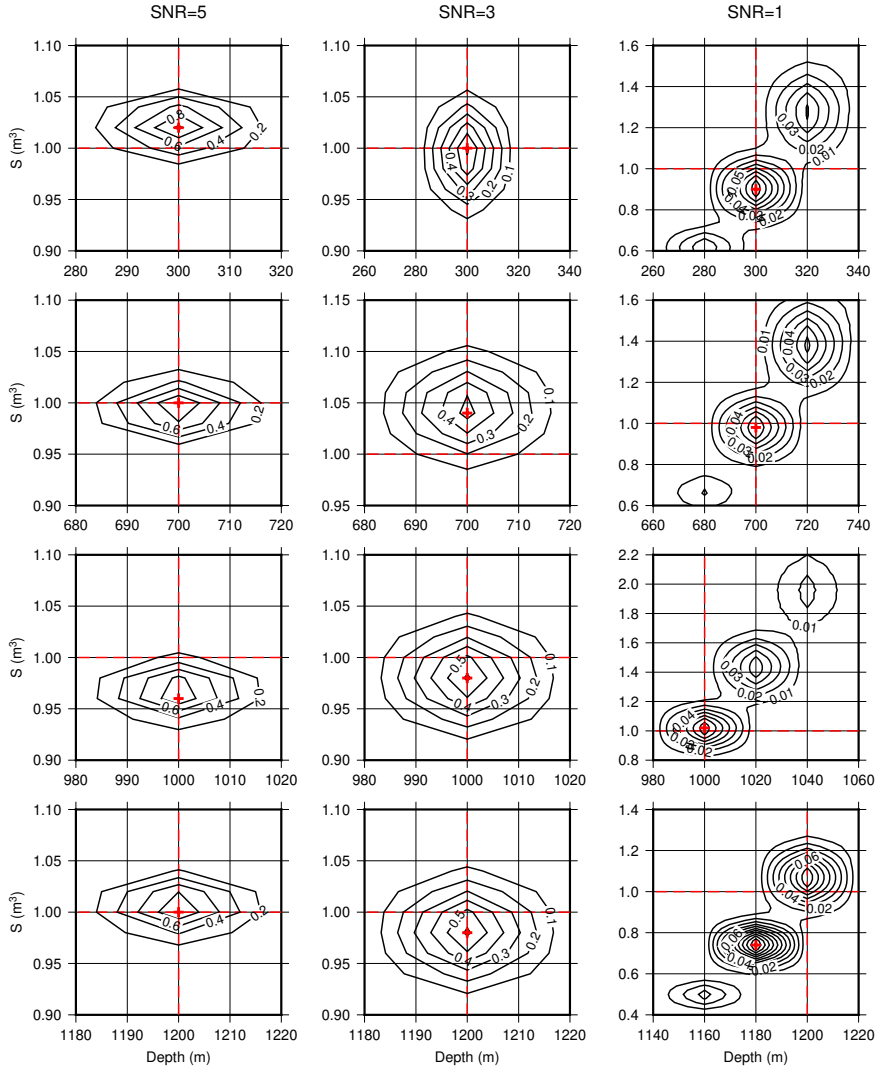

Figure 4.3: *Inversion results using ten stations and ten frequencies. The red lines correspond to the real source depth and strength, and the contour lines provide the probabilities. (a) for SNR=5, the inversion results are correct, and the probability is high. (b) SNR=3 leads to overestimating the source strength. The source depth is correct. (c) SNR=1 leads to higher uncertainties in both depth and strength. Moreover, the probabilities are one order of magnitude lower than in a and b.*

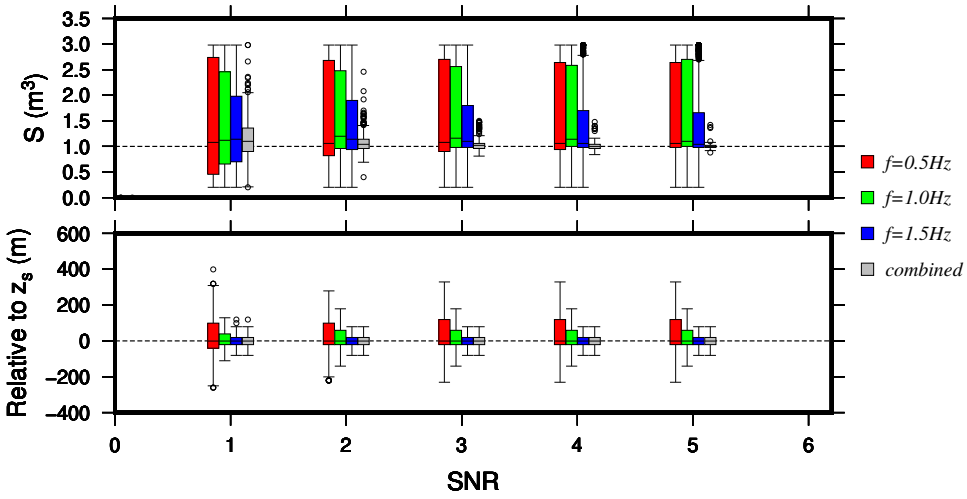

Figure 4.4: *Result distributions of 1000 realizations for varying SNR. The boxes represent the 25 and 75 percentile range, and the bars the 5, 50, and 95 percentiles. The circles represent outliers. The red, green, and blue colors are ten-station single-frequency inversions. Gray boxes represent the ten-station and three-frequency inversions results.*

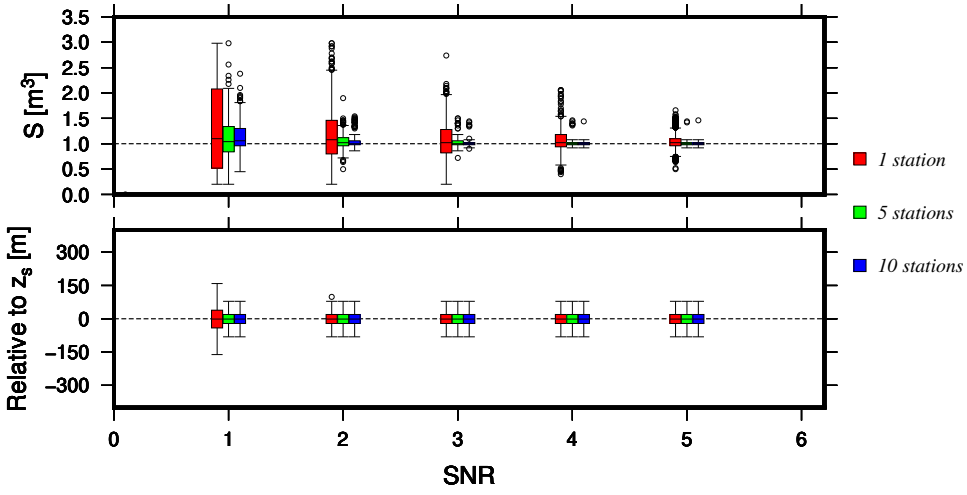

Figure 4.5: *Results distributions of 1000 ten-frequency inversions with a different number of stations. The blue, green, and red boxes represent the ten-station, five-station, and one-station inversions, respectively.*

■ 4.3.2 Atmospheric uncertainties using an ECMWF ensemble.

An exact atmospheric profile, as in Chapter 4.3.1, provides robust inversion results given a different number of stations and SNRs. However, the actual state of the

atmosphere is estimated by an atmospheric model and a data assimilation system, which is never exact. The atmospheric properties can differ from the real atmosphere due to both model and observation uncertainties. To study the influence of the atmospheric uncertainties on the accuracy of the inversion, we apply probabilistic infrasound propagation modeling using an ensemble of realistic perturbed atmospheric profiles [*Smets et al.*, 2015].

Realistic perturbed atmospheric profiles are provided by the Ensemble Data Assimilation (EDA) system of the ECMWF. The EDA consists of 25 members that discretely sample the probability density function of the atmosphere [*Buizza et al.*, 1999, 2008]. The EDA mean is defined as the "real" atmosphere, and used to generate the "observations" while the individual EDA members are used to create 25 synthetics, but likely, data sets for the inversion. For each of the data sets, the source parameters probabilities are calculated and eventually combined into one posterior probability distribution that captures the effect of the atmospheric uncertainties. Therefore, the final posterior probability, $\bar{P}(z_s, S|M(\boldsymbol{r},\boldsymbol{\theta},\boldsymbol{\omega})$, will be

$$\bar{P}(z_s, S|M(\boldsymbol{r},\boldsymbol{\theta},\boldsymbol{\omega})) = \frac{1}{N}\sum_{l=1}^{N} P_l(z_s, S|M(\boldsymbol{r},\boldsymbol{\theta},\boldsymbol{\omega})), \tag{4.3.1}$$

when N is the number of the ensemble members, and $P_l(z_s, S|M(\boldsymbol{r},\boldsymbol{\theta},\boldsymbol{\omega}))$ is the posterior probability for the inversion with the l^{th} member.

Unlike the homogeneous water layer that is used in Chapter 4.3.1, now, the atmospheric profiles are placed on top of a typical oceanic profile known as the Munk profile [*Munk*, 1974]. This oceanic profile consists of a minimum in the speed of sound profile around a depth of 1000 m which forms the Sound Fixing and Ranging channel. Defining the EDA mean as the "real" atmospheric conditions, an "observation" data set, $M(r_i, \theta_j, \omega_k)$, is generated for a source at z=1000 m and $S = 1$ m^3. Then, a synthetic data set, $m_l(z_s, r_i, \theta_j, \omega_k, S)$, is generated for each ensemble member according to the parameters in Table 4.2. Figure 4.6 shows the simulated absolute pressure curves on the ground ($z = 0$ m) from a 0.8 Hz source at a depth of 1000 m, for the 25 ensemble members (gray) and the EDA mean (black). The variation in the pressure curves is associated with the variance of the profiles (Figure 4.6 left column). Small variations in the ducts' altitude lead to different spatial maxima positions. For example, the absolute pressure at 290 km for $\theta = 70°$ ranges between ,approximately, 0 μPa to 0.009 μPa, while for $\theta = 90°$ at 280 km it ranges between 0.0005 μPa to 0.0055 μPa. Moreover, inspecting the propagation for $\theta = 110°$ shows that the absolute pressure at 160 km ranges between 0.005 μPa to 0.01 μPa, and between ,approximately, 0 μPa to 0.007 μPa at 300 km. Due to such differences, the positions of the receivers will have a significant role in the inversion results.

The inversion performance is tested on four different setups (Figure 4.7). Two-station inversion is performed for three location pairs along propagation paths in three azimuths. The fourth test is a one-station inversion. Receiver locations are picked according to the return height of the ducts to guarantee the arrival of atmo-

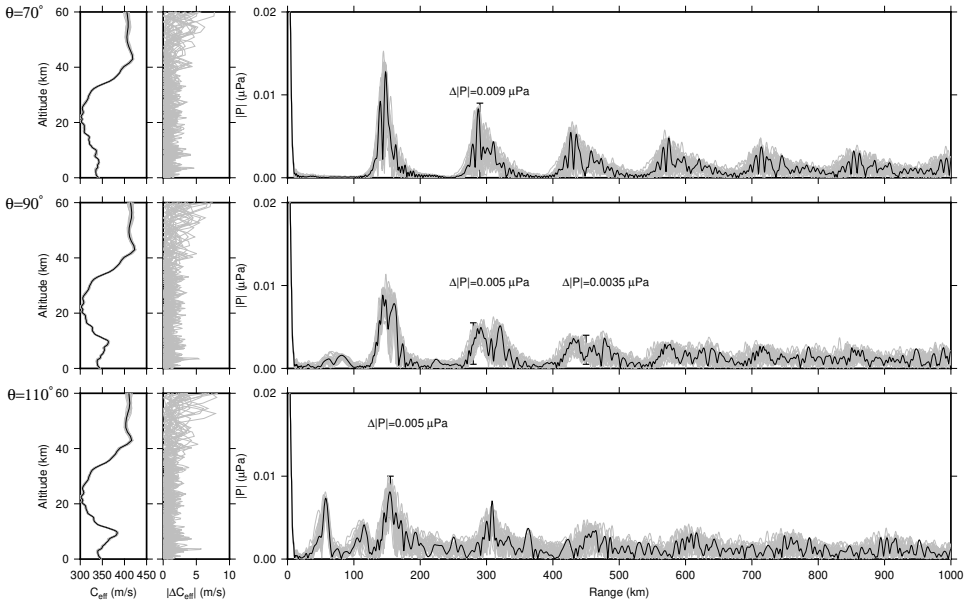

Figure 4.6: *Simulated absolute pressure curves on the ground (z=0 m) from a 0.8 Hz source at a depth of 800 m, for the 25 ensemble members (gray) and the EDA mean (black). The left frames show the effective sound speed profiles for each propagation azimuth, and the absolute difference of each ensemble member from the EDA mean. The bars in the absolute pressure frames indicate the absolute pressure range in three of the locations of the receivers.*

spheric phases at the sites. However, the absolute pressure range at the locations varies in order to capture the atmospheric uncertainties effect. For instance, there is a 0.005 μPa and 0.009 μPa range at $R_{110^\circ} = 160$ km and $R_{70^\circ} = 290$ km, respectively. These ranges correspond to the station locations for inversions a-c, and g-i in Figure 4.7.

Figure 4.7 shows the inversion results for the four setups (rows), and three SNRs (columns). Regardless of the inversion setup and SNR, all of the approximated source depths are bounded between 900 m and 1100 m. Inversions (a) and (d) have the most significant uncertainties in the source depth, while inversions (b) and (c) are bounded between 950 m and 1050 m. The effect of the absolute pressure range at the sites is prominent in the source strength estimations. Inversions (a) underestimate the source strength to half of its real value, as well as having low probabilities. In contrast, inversions (c) estimate it to be 0.9 m^3 with relatively high probabilities. Finally, the one station inversions (d) perform better than the two station inversions (a). The large variance in the propagation in 70° impairs the capability to resolve the source parameters accurately.

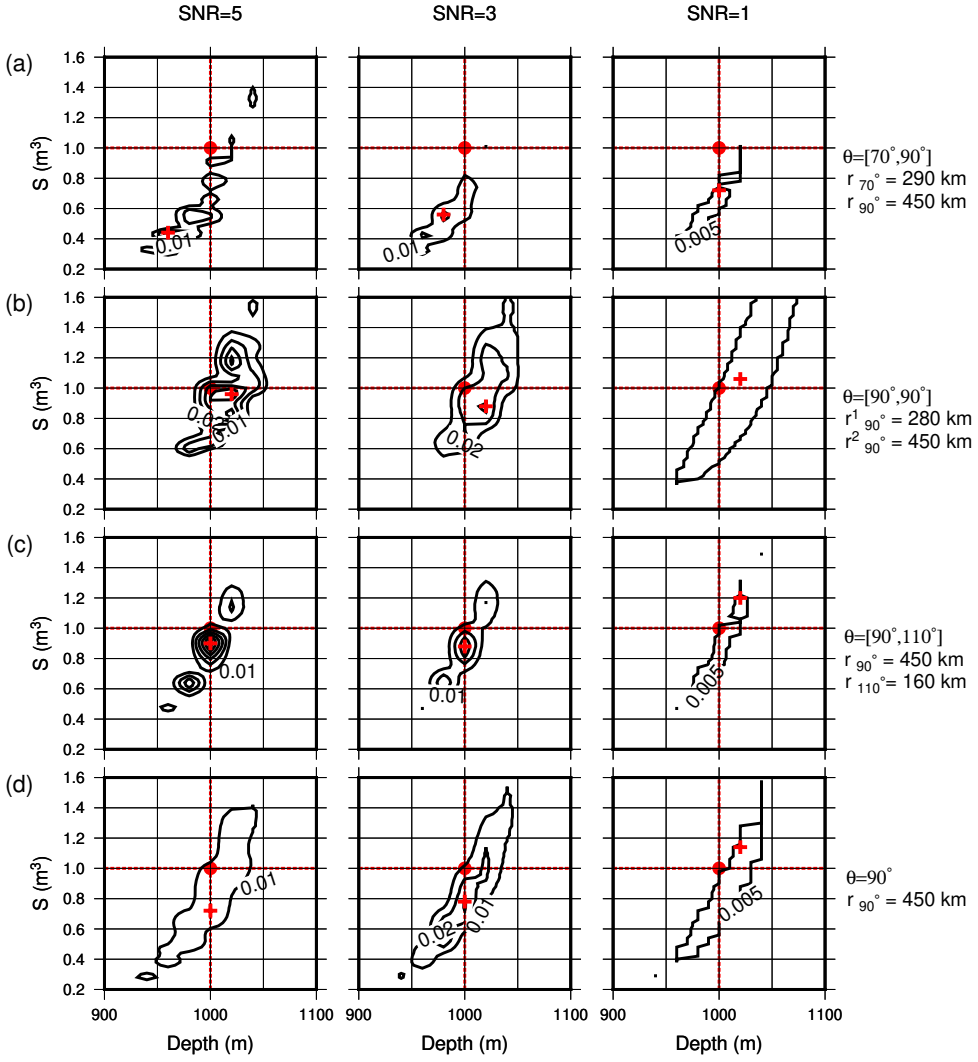

Figure 4.7: *Probabilities for different inversions' setups. The number of stations and their locations is indicated on the right-hand side of each row. The columns indicate the SNR. Red lines indicate the real source parameters, and red crosses indicate the parameters with the highest probability.*

Table 4.2: *ECMWF modeling parameters*

z [m]	dz [m]	θ [deg]	$d\theta$ [deg]	f [Hz]	df [Hz]	S [m^3]	dS [m^3]
500-1500	20	70-110	20	0.5-1.5	0.1	0.2-3	0.02

4.4 Conclusions and discussion

This work studied the prospect of using long-range infrasound signals from submerged sources to invert for the source depth and strength. A probabilistic inversion scheme was tested on two synthetic case studies and showed that using long-range infrasound signals to resolve the depth and strength of a shallow submerged source is attainable. Although the analysis focuses on underwater sources, the results can be useful also for subsurface sources.

The inversion is based on minimizing the difference between an observable and modeled signal and provides a posterior probability density function for the parameter space. In the first synthetic case, a known atmospheric profile is used to evaluate the effect of the number of stations, the signals' frequency band, and SNR on the inversion results (Chapter 4.3.1). It is shown that broadband signals are essential for resolving the source parameters. The sensitivity of the coupling mechanisms to different frequency bands set stringent constraints on the inversion, allowing an accurate estimation of the source depth and strength even for low SNRs. The skewness of the source depth and strength distribution if Figure 4.4 can be a result of the linear and non-linear effects due to variations in the source parameters. Variations in the source depth can lead to significant variations in amplitude with a stronger effect for decreasing depth, i.e., small decrease in the source depth lead to a large increase in the received signal's amplitude. Therefore, it seems that fine-tuning of the source parameters for minimizing the likelihood function can be easily achieved by small increase of the source depth and larger variations of the source strength. Note that this behavior exists only in the single-frequency inversions, and multiple frequencies provide a symmetric distribution around the real source parameters.

There was no difference between the five- and ten-station inversion. However, comparing one- and five-station inversion results show that multiple stations reduce the depth-yield trade-off. This behavior is further seen in the comparison between one- and two-station inversion in Chapter 4.3.2. Results from Chapter 4.3.1 indicate that using a broader frequency range is more beneficial than multiple station inversion. A significant increase in/of the frequency range will allow obtaining the space-time representation of the simulated wavefield. In such case, arrival times of the different atmospheric phases can further constrain the inversion.

An ensemble of perturbed atmospheric profiles by the ECMWF is used to appraise the effect of atmospheric uncertainties on the inversion results. Propagation in three different azimuths experience different speed-of-sound profiles, provided us

with versatile data sets to choose the location of the stations. Results show that the spatial position of the stations is crucial to the accuracy of the estimated source parameters. The large variance of the pressure at $\theta = 70°$, compared to the stations at $\theta = 90°$ and $\theta = 110°$, leads to underestimating the source strength by approximately 50%. Moreover, inversions (a) perform worse than the one station inversions (d), which may seem like a contradiction of our previous statement that higher spatial coverage improves the results. While in this case it is true, one must keep in mind that the quality of the data plays an essential role in the inversion. Naturally, inversion with a small variance data set performs better than with a large variance data set. Yet, regardless of the number of stations, their positions, and SNRs, all of the estimated depths were within a ± 100 m range from the real source depth. Variations up to 5 m/s in the ensemble effective speed of sound profiles proved to have a significant impact on the narrowband simulated pressure. This behavior motivates the incorporation of narrowband acoustic simulations in inversions for atmospheric specifications.

Throughout this study, the source type was kept as a monopole in order to limit the number of unknown parameters. Different source types will have a different radiation pattern, and whether one can invert also for the source type is still unknown. Another behavior that was excluded from this study is the non-linearity in the vicinity of the source. Although it is known that explosions are non-linear in the near-field, to the best of our knowledge, its effect on the transmission through stark interfaces has not been studied. In addition, no constraints or prior knowledge on the source parameters were used. Therefore, any restrictions on the source parameters will improve the accuracy of the estimated parameters.

Implications regarding shallow underground sources can be deduced on the basis of this study. However, benchmark tests with real events should be the scope of future research. Moreover, this study assumes a horizontally stratified range-independent medium. Therefore, further study on the effect of a complex environment, such as topography and range dependent medium, on the inversion results, is needed.

5

Conclusions and recommendations

"It's not the mountain we conquer but ourselves."

Edmund Hillary

5.1 Conclusions

The goal of this thesis was to perform an empirical and numerical study about the generation of atmospheric infrasound waves from subsurface sources. The empirical studies (based on observations from the 2013, 2016, and 2017 DPRK's underground nuclear tests) provided complex data sets that raised questions like: why are there observables signals? Where are they coupled to the atmosphere? What is the effect of the atmospheric conditions on the observations? Also, can we use infrasonic signals to provide information about the subsurface source parameters? Motivated by these observations (and others), a numerical investigation was carried out to study how the different parts of the subsurface wavefield spectrum (seismic or acoustic) are coupled to the atmosphere and allow long-range infrasound propagation.

Chapter 2 shows the complex infrasound wavefield that is generated by a subsurface source, and demonstrates, as well, the effect of the atmospheric conditions on the prospect of detecting such signals. Detection of long-range infrasound propagation is strongly dependent on the propagation conditions along the source-receiver path, and on the local noise levels at the receiver due to winds a turbulences. During the 2016 test, the development of a sudden stratospheric warming changed the regional winds regime, causing unfavorable propagation conditions from the test site to both IS45 and IS30 (Chapter 2.1). Analysis of the atmospheric conditions during the 2017 test (Chapter 2.2) shows that low wind conditions, due to the autumnal equinox, lead to a lack of both tropospheric and stratospheric waveguides.

Despite the absence of these efficient waveguides, detections were possible through thermospheric propagation as well as (partial) reflections from small scale structures.

Earth-atmosphere and Earth-ocean-atmosphere coupling played an essential role in the detections of the mentioned DPRK tests. Both 2013 and 2016 tests were estimated to have the same moment magnitude (M_w~4.7), however, only signals from the 2013 test were clearly detected. The lack of observations of the 2016 test can be explain by a combination between variations in the source parameters and atmospheric conditions. Since both tests had the same moment magnitude and the atmospheric conditions are known, we hypothesized that the 2016 test occurred in a larger depth than in 2013. Using a first-order approximation, we show that the source at the 2016 test was 1.5 times deeper than in 2013. This result is in agreement with source estimations from regional seismic observations. The exponential decay of the near-field seismic waves leads to an amplitude decrease of one order of magnitude, which levels the infrasound signal's amplitude with the background noise levels. This finding coincides with the effects of the source depth that is presented in Chapter 3. Back-projections of the 2017 test's detections reveal that infrasound was generated through Earth-atmosphere and Earth-ocean-atmosphere coupling. Coupling in an Earth-atmosphere system comprises of epicentral infrasound, and radiation from the Hamgyong mountain range and the Tumen River delta. Signals arriving from the Japan Basin were coupled through an Earth-ocean-atmosphere system. Analysis of the coupling mechanisms in Chapter 3 can explain only part of these observations by coupling of inhomogeneous body waves and air-coupled surface waves. The effect of topographic features on the coupled energy has not yet studied.

The detailed analysis of the coupling mechanisms in Chapter 3 provides fundamental insights on the influence of the subsurface source parameters on long-range infrasound propagation. The simplified model allows to: (1) obtain exact solutions of the propagating wavefield in the different coupled systems. (2) Differentiate between the coupling mechanisms, and (3) quantify their contributions. Variations in the source parameters impacts both the coupled amplitude and the radiation pattern. As the source depth increase, less energy is coupled to the atmosphere. Also, the radiation pattern from a subsurface source is not homogeneous, and it depends on the source parameters. Consequently, the energy balance in the atmospheric waveguides may differ. For example, assuming the same atmosphere, the relative amplitudes of tropospheric and stratospheric phases will change according to the source parameters. These characteristics are further employed in an infrasound-based inversion for the source parameters (Chapter 4). It is shown that broadband signals are essential for resolving the source parameters. The sensitivity of the coupling mechanisms to different frequency bands set stringent constraints on the inversion, allowing an accurate estimation of the source depth and strength even for low SNRs.

In an Earth-atmosphere system, surface waves also contribute to the radiated acoustic energy. Depending on the source depth, the amplitude of the radiated en-

ergy can be within the same order of magnitude as from the evanescent coupling or becoming the dominant contributor to the radiated energy. Although surface waves radiate high amplitude acoustic waves, they do not necessarily play a part in long-range propagation. The ability of air-coupled surface waves to get trapped in the atmospheric waveguides depends on their phase velocities. Radiated energy from high phase velocity surface waves will propagate steeply upwards and will not get trapped in the waveguides. As the phase velocity decrease, the surface-waves' horizontal component increase, eventually allowing the coupled energy to get trapped in the atmospheric waveguides. This coupling mechanism generated the observed signal from the Tumen River delta in the 2017 DPRK's underground nuclear test.

In the last part of this study, we use an ensemble of perturbed atmospheric profiles from the ECMWF to appraise the effect of atmospheric uncertainties on the inversion results. The variance of the data sets played a significant role in the inversion's performance. Naturally, inversion with a small variance data set performs better than with a large variance data set. Since the location of the stations also affects the variance, their spatial position is crucial to the accuracy of the estimated source parameters. Here, no constraints or prior knowledge on the source parameters was used. Such restrictions can be obtained from seismic observations, and improve the accuracy of the estimated parameters. One must keep in mind that the variations in the ensemble drive the variance in the data sets. Fluctuations up to 5 m/s in the effective speed of sound profiles and small variations in the tropospheric and stratospheric return heights had a significant impact on the narrowband simulated pressure. Therefore, in the case of using modeling results like pressure and transmission-loss, the atmospheric uncertainties must be taken into account.

5.2 Recommendations and outlook

The presented theoretical and numerical work on long-range infrasound propagation assumes a homogeneous horizontally layered medium. This simplified assumption provides a basic understanding of infrasound propagation from subsurface sources. However, the Earth-ocean-atmosphere system is more complicated than that. Underground geological structures, topographic features, and range dependent variations in the density and velocity profiles are elementary parts in our planet. Observations of infrasound signals that were generated in mountain ranges and different parts along the propagation path between seismic sources and infrasound receivers motivate further investigation of their effect on the coupled infrasonic waves.

The influence of the subsurface source parameters on the radiated acoustic energy was examined. It is shown that coupling of inhomogeneous body waves depends on near-field effects, i.e., the source needs to be in a distance of less than a wavelength from the Earth or ocean interface with the atmosphere. Studying near-field effects, especially regarding shallow explosions, lead to reflections about the contributions of non-linearities to the coupled energy. Incorporating existing studies on acoustic

and seismic explosions source models (which are non-linear) with propagation models in coupled systems should be taken into account in future studies.

The sensitivity of infrasonic signals to the subsurface source parameters and medium properties (both subsurface and atmosphere) endorses the development of additional infrasound-based inversions. Previous studies on atmospheric inversions using infrasonic signals are based on back-azimuth and apparent velocity measurements, while the synthetic data is modeled by ray-tracing methods. A full waveform inversion is an expensive (numerically) process for long-range infrasound propagation. However, using discrete frequencies for narrow-band modeling can provide constraints like pressure amplitudes, and can be easily incorporated in the inversion schemes.

Finally, I would like to encourage the development of infrasound-remote-sensing for subsurface sources like underground explosions, earthquakes' ground motions and source mechanisms, and volcanic eruptions both underwater and above ground. Integrating the results and techniques from the presented studies imply that we now have the tools to accurately process seismo-acoustic signals, backproject the detections to the coupling locations, quantify the contribution of the coupling mechanisms, and forward propagate the waves from source to receiver considering the atmospheric effects. Moreover, an ongoing study shows that using these tools, the earthquake radiation pattern, wich corresponds to the event's moment tensor, can be resolved from infrasonic signals.

A

Supplemental information to: Wave propagation theory

A.1 Infrasound wave equation for reduced pressure

Let us start with the infrasound wave equation for a stratified moving medium

$$\frac{d}{dt}\left[\frac{d}{dt}\left(\frac{1}{\rho_0 c^2}\frac{dp'}{dt}\right) - \nabla\cdot\left(\frac{1}{\rho_0}\nabla p'\right)\right] + 2\left(\frac{d\boldsymbol{v}_{0H}}{dz}\cdot\nabla_H\right)\left(\frac{1}{\rho_0}\frac{\partial p'}{\partial z}\right) = 0. \quad \text{(A.1.1)}$$

In the frequency-(horizontal)wavenumber domain,the material derivative can be written as

$$\frac{d}{dt} = (\partial/\partial t + \boldsymbol{v}_{0H}\cdot\nabla_H) = (i\omega - i\boldsymbol{k}_H\cdot\boldsymbol{v}_{0H}) = i\omega\left(1 - \frac{\boldsymbol{k}_H\cdot\boldsymbol{v}_{0H}}{\omega}\right) = i\omega\beta, \quad \text{(A.1.2)}$$

where the horizontal gradient ∇_H is a multiplication by $-i\boldsymbol{k}_H$. Plugging it in equation (A.1.1) yields

$$i\omega\beta\left[-\frac{\omega^2\beta^2}{\rho_0 c^2}p' + \frac{k_H^2}{\rho_0}p' - \frac{\partial}{\partial z}\left(\frac{1}{\rho_0}\frac{\partial p'}{\partial z}\right)\right] - \frac{2i\boldsymbol{k}_H}{\rho_0}\frac{d\boldsymbol{v}_{0H}}{dz}\frac{\partial p'}{\partial z} = 0, \quad \text{(A.1.3)}$$

which after simple algebra becomes

$$\frac{\omega^2\beta^2}{\rho_0 c^2}p' - \frac{k_H^2}{\rho_0}p' + \frac{\partial}{\partial z}\left(\frac{1}{\rho_0}\frac{\partial p'}{\partial z}\right) + \frac{2\boldsymbol{k}_H}{\omega\beta\rho_0}\frac{d\boldsymbol{v}_{0H}}{dz}\frac{\partial p'}{\partial z} = 0. \quad \text{(A.1.4)}$$

Recognizing that

$$\frac{d\beta}{dz} = -\frac{\boldsymbol{k}_H}{\omega}\frac{d\boldsymbol{v}_{0H}}{dz}, \quad \text{(A.1.5)}$$

equation (A.1.4) can be written as

$$\frac{\omega^2\beta^2}{\rho_0 c^2}p' - \frac{k_H^2}{\rho_0}p' + \frac{\partial}{\partial z}\left(\frac{1}{\rho_0}\frac{\partial p'}{\partial z}\right) - \frac{2}{\beta\rho_0}\frac{d\beta}{dz}\frac{\partial p'}{\partial z} = 0. \quad \text{(A.1.6)}$$

Dividing equation (A.1.6) by β^2 yields

$$\frac{\omega^2}{\rho_0 c^2}p' - \frac{k_H^2}{\rho_0\beta^2}p' + \frac{1}{\beta^2}\frac{\partial}{\partial z}\left(\frac{1}{\rho_0}\frac{\partial p'}{\partial z}\right) - \frac{2}{\rho_0\beta^3}\frac{d\beta}{dz}\frac{\partial p'}{\partial z} = 0. \tag{A.1.7}$$

One can show that

$$-\frac{2}{\beta^3}\frac{d\beta}{dz} = \frac{d}{dz}\left(\frac{1}{\beta^2}\right). \tag{A.1.8}$$

In addition,

$$\begin{aligned}\frac{1}{\beta^2}\frac{\partial}{\partial z}\left(\frac{1}{\rho_0}\frac{\partial p'}{\partial z}\right) + \frac{1}{\rho_0}\frac{d}{dz}\left(\frac{1}{\beta^2}\right)\frac{\partial p'}{\partial z} &= \frac{1}{\rho_0\beta^2}\frac{\partial^2 p'}{\partial z^2} + \frac{d}{dz}\left(\frac{1}{\rho\beta^2}\right)\frac{\partial p'}{\partial z} \\ &= \frac{\partial}{\partial z}\left(\frac{1}{\rho_0\beta^2}\frac{\partial p'}{\partial z}\right)\end{aligned} \tag{A.1.9}$$

Using equation (A.1.9), identifying ω^2/c^2 as k^2, and multiplying by $\rho_0\beta^2$, equation (A.1.7) takes the form

$$\left(k^2\beta^2 - k_H^2\right)p' + \rho_0\beta^2\frac{\partial}{\partial z}\left(\frac{1}{\rho_0\beta^2}\frac{\partial p'}{\partial z}\right) = 0. \tag{A.1.10}$$

Defining the reduced pressure as $\tilde{p} = p'/\sqrt{\rho_0}\beta$, and substituting it in equation (A.1.10) yields the infrasound wave equation for the reduced pressure

$$\frac{\partial^2\tilde{p}}{\partial z^2} + \left[(k^2\beta^2 - k_H^2) + \frac{1}{2\rho_0\beta^2}\frac{\partial^2(\rho_0\beta^2)}{\partial z^2} - \frac{3}{4}\left(\frac{1}{\rho_0\beta^2}\frac{\partial(\rho_0\beta^2)}{\partial z}\right)^2\right]\tilde{p} = 0. \tag{A.1.11}$$

For infrasonic frequencies above 0.05Hz, the second-order derivative and the square of the first-order derivative of $\rho_0\beta^2$ are negligible [*Assink et al.*, 2017]. Omitting them provides the Helmholtz equation for the reduced pressure. One must keep in mind that the relation between the pressure and particle velocity is now $\partial p/\partial z = -i\omega\rho_0\beta v_z$. In the case of modeling with the FFP as shown in Chapter 4, after dividing the medium to piecewise homogeneous layers, the wavefield can be represented in terms of displacement potential, Φ, and the pressure can be computed by $p = -\omega^2\rho_0\beta\Phi$.

A.2 Retrieving the seismo-acoustic wavefield

■ A.2.1 Free-field Green's functions

In seismo-acoustic modeling the displacement field in each layer can be expressed in terms of a scalar potential for the acoustic medium and a scalar and a vector potential for the elastic medium. These potentials are the basis of the Green's functions of the displacement field. In the case of a homogeneous elastic medium, the wavefield can be decoupled into P-SV and SH motions. These decoupled motions can be expressed by two scalar potentials and one scalar potential, respectively [*Aki*

and Richards, 2002]. In this work, we assume the medium to be horizontally stratified, axisymmetric, with coupled elastic-acoustic layers. For such set-up, the SH motion has no contribution to the acoustic wavefield in the fluid layers, and it will be neglected.

Under these assumptions, the displacement field within a layer at a distance r and depth z, in the acoustic medium can be written in cylindrical coordinates as

$$\begin{aligned} u_m^f(r,z) &= \frac{\partial \Phi_m^f}{\partial r} \\ w_m^f(r,z) &= \frac{\partial \Phi_m^f}{\partial z}. \end{aligned} \tag{A.2.1}$$

Accounting only for P-SV motion in the elastic medium, the displacement field within a layer can be written as

$$\begin{aligned} u_m^s(r,z) &= \frac{\partial \Phi_m^s}{\partial r} + \frac{\partial^2 \Psi_m^s}{\partial r \partial z} \\ w_m^s(r,z) &= \frac{\partial \Phi_m^s}{\partial z} - \frac{1}{r}\frac{\partial}{\partial r} r \frac{\partial \Psi_m^s}{\partial r}. \end{aligned} \tag{A.2.2}$$

In equation (A.2.1)the potential Φ_m^f represent the compressional wave potential, and in equation (A.2.2) the potentials Φ_m^s and Ψ_m^s represent the compressional and shear potentials, respectively. All potentials must satisfy the wave equation. u_m and w_m are the horizontal and vertical displacements, respectively, and suffixes f and s correspond to fluid and solid medium. Hooke's law, which relates stress and strain in an elastic medium, is used to compute the corresponding stress field.

Wave type	Earth	Ocean	Atmosphere
Compressional	Φ^s $k = \omega / v_p$ $v_p(\rho_0, \lambda, \mu)$	Φ^f $k = \omega / c_{\text{ocean}}$ $c_{\text{ocean}}(p_0, \rho_0, T, S)$	Φ^f $k = \omega / c_{\text{eff}}$ $c_{\text{eff}}(p_0, \rho_0, T, \boldsymbol{v}_{0H})$
Shear	Ψ^s $\tilde{k} = \omega / v_s$ $v_s(\rho_0, \mu)$		

Table A.1: *Potential types, wavenumber definitions and propagation velocities for the different media. The seismic wave velocities are functions of the density and Lamé parameters. The speed of sound in the ocean depends on the unperturbed pressure and density p_0 and ρ_0, the temperature T, and salinity S. The effective speed of sound in the atmosphere depends on the unperturbed pressure and density, temperature T, and the horizontal winds.*

Since the different coupling mechanisms are frequency and wavenumber dependent, solving the wave equation in the f-k domain is beneficial. Defining Λ as an

arbitrary potential, the frequency-domain wave equation is known as the Helmholtz equation $[\nabla^2 + k_m^2]\Lambda_m(r,z) = 0$. Applying the Hankel transform to the Helmholtz equation yields the depth-separated Helmholtz equation

$$\left[\frac{d^2}{dz^2} + k_z^2\right]\Lambda_m(k_r,z) = 0, \tag{A.2.3}$$

where $k_z = \sqrt{k_m^2 - k_r^2}$ is the vertical wavenumber. k_r is the horizontal wavenumber, and k_m is the layer wavenumber. Depending on the medium type in each layer, the potential Λ and the vertical wavenumber k_z will be replaced according to the potentials and propagation velocities presented in Table A.1. Linear wave propagation is assumed to be an adiabatic process, and the propagation velocities are derived from the equations of state. For the elastic layers, solutions of both compressional and shear potentials need to be combined in order to obtain a complete representation of P-SV motion. Moreover, only a combination of both potentials gives rise to surface waves which are significant contributors to the seismo-acoustic wavefield.

Equation (A.2.3) is an ordinary differential equation in the vertical axis, and the solution for each layer is a linear combination of the homogeneous solution $\Lambda_m(k_r,z)$and a particular solution $\hat{\Lambda}_m(k_r,z)$ if a source is present. Exact solutions for equation (A.2.3) can be written in terms of wavenumber integrals. The latter implies that field's exact Green's functions in the f-k domain can be retrieved. Decomposing the solution into up and down going wavefields allows for a straightforward implementation of the boundary conditions (BC) in the numerical solution. Defining A^- and A^+ respectively as the up and down going wavefield amplitudes, the compressional potential solution can be written as $\Phi_m(k_r,z) = A^- e^{-ik_z z} + A^+ e^{ik_z z}$. Its frequency domain representation is

$$\Phi_m(r,z) = \int_0^\infty [A^- e^{-ik_z z} + A^+ e^{ik_z z}] J_0(k_r r) k_r dk_r, \tag{A.2.4}$$

and $J_0(k_r r)$ is the Bessel function of the first kind. Similarly, $\Psi_m(r,z)$ is represented as

$$\Psi_m(r,z) = \int_0^\infty \frac{1}{k_r}[B^- e^{-i\tilde{k}_z z} + B^+ e^{i\tilde{k}_z z}] J_0(k_r r) k_r dk_r. \tag{A.2.5}$$

The $1/k_r$ factor ensures that the two potentials have the same dimensions due to an extra spatial derivative of the shear potential in equation (A.2.2). When $k_r > k_m$ or $k_r > \tilde{k}_m$, the vertical wavenumber of the potentials is imaginary. This part of the spectrum is known as evanescent, and its amplitude decays exponentially with vertical distance. As k_r increases with increasing frequency or decreasing trace velocity, k_z and $\tilde{k}_z$ obtain a larger imaginary value and decay over a shorter distance. This property plays an essential role in the coupling process and affects the emitted infrasonic wave amplitude.

The potentials' coefficients are obtained using the Direct Global Matrix (DGM) method, which is based on solving the continuity equations for all the interfaces

(BC between the layers) as well as the top and bottom BC simultaneously [*Schmidt and Tango*, 1986]. The BC for a solid-solid interface are the continuity of normal and tangential stress and vertical and horizontal displacements. A fluid-fluid interface requires the continuity of normal stress and vertical displacement. Finally, the BC at a solid-fluid interface are the continuity of vertical displacement and normal stress, and the vanishing of the tangential stress. Note that as the shear wavefield is part of both vertical displacement and normal stress, the SV motion contributes to the acoustic field in the fluid layer.

The acoustic vertical stress and normal displacement are written as:

$$w^f(r,z) = \frac{\partial \Phi^f(r,z)}{\partial z} = \int_0^\infty [-ik_z A^- e^{-ik_z} + ik_z A^+ e^{ik_z z}] J_0(k_r r) k_r dk_r \tag{A.2.6}$$

$$\begin{aligned} \sigma_{zz}^f(r,z) &= -P^f(r,z) = K\nabla^2 \Phi^f(r,z) = -\rho\omega^2 \Phi^f(r,z) \\ &= -\rho\omega^2 \int_0^\infty [A^- e^{-ik_z z} + A^+ e^{ik_z z}] J_0(k_r r) k_r dk_r \end{aligned} \tag{A.2.7}$$

To obtain the elastic normal and tangential stress, and vertical and horizontal displacements, let us write the partial derivatives of the pressure and shear potentials.

$$\frac{\partial \Phi^s(r,z)}{\partial r} = -\int_0^\infty k_r [A^- e^{-ik_z z} + A^+ e^{ik_z z}] J_1(k_r r) k_r dk_r \tag{A.2.8}$$

$$\frac{\partial \Phi^s(r,z)}{\partial z} = \int_0^\infty [-ik_z A^- e^{-ik_z z} + ik_z A^+ e^{ik_z z}] J_0(k_r r) k_r dk_r \tag{A.2.9}$$

$$\frac{\partial \Psi^s(r,z)}{\partial r} = -\int_0^\infty [B^- e^{-i\tilde{k}_z z} + B^+ e^{i\tilde{k}_z z}] J_1(k_r r) k_r dk_r \tag{A.2.10}$$

$$\frac{\partial \Psi^s(r,z)}{\partial z} = \int_0^\infty \frac{1}{k_r} [-i\tilde{k}_z B^- e^{-i\tilde{k}_z z} + i\tilde{k}_z B^+ e^{i\tilde{k}_z z}] J_0(k_r r) k_r dk_r \tag{A.2.11}$$

$$\frac{\partial}{\partial r}\left(\frac{\partial \Psi^s(r,z)}{\partial z}\right) = \int_0^\infty [i\tilde{k}_z B^- e^{-i\tilde{k}_z z} - i\tilde{k}_z B^+ e^{i\tilde{k}_z z}] J_1(k_r r) k_r dk_r \tag{A.2.12}$$

Differentiation of Bessel functions

$$\begin{aligned} \frac{\partial J_0(z)}{\partial z} &= -J_1(z) \\ \frac{\partial z^n J_n(z)}{\partial z} &= z^n J_{n-1}(z) \\ \frac{\partial z^{-n} J_n(z)}{\partial z} &= -z^{-n} J_{n+1}(z) \end{aligned}$$

$$\begin{aligned}\frac{1}{r}\frac{\partial}{\partial r}\left(r\frac{\partial \Psi^s(r,z)}{\partial r}\right) &= \frac{1}{rk_r}\frac{\partial}{\partial r}\left(rk_r\frac{\partial \Psi^s(r,z)}{\partial r}\right)\\ &= \int_0^\infty k_r[B^- e^{-i\tilde{k}_z z} + B^+ e^{i\tilde{k}_z z}]J_0(k_r r)k_r dk_r\end{aligned} \tag{A.2.13}$$

Substituting the partial derivatives in the displacement equations A.2.2 and rearranging the arguments down going waves first and then up going (for numerical stability), we can express the displacements in the following integral forms:

$$\begin{aligned}u^s(r,z) &= \frac{\partial \Phi^s(r,z)}{\partial r} + \frac{\partial^2 \Psi^s(r,z)}{\partial r \partial z}\\ &= \int_0^\infty [-k_r A^- e^{-ik_z z} - k_r A^+ e^{ik_z z} + i\tilde{k}_z B^- e^{-i\tilde{k}_z z} - i\tilde{k}_z B^+ e^{i\tilde{k}_z z}]J_1(k_r r)k_r dk_r\\ &= \int_0^\infty [-k_r A^+ e^{ik_z z} - i\tilde{k}_z B^+ e^{i\tilde{k}_z z} - k_r A^- e^{-ik_z z} + i\tilde{k}_z B^- e^{-i\tilde{k}_z z}]J_1(k_r r)k_r dk_r\end{aligned} \tag{A.2.14}$$

$$\begin{aligned}w^s(r,z) &= \frac{\partial \Phi^s(r,z)}{\partial z} - \frac{1}{r}\frac{\partial}{\partial r} r\frac{\partial \Psi^s(r,z)}{\partial r}\\ &= \int_0^\infty [-ik_z A^- e^{-ik_z z} + ik_z A^+ e^{ik_z z} + k_r B^- e^{-i\tilde{k}_z z} + k_r B^+ e^{i\tilde{k}_z z}]J_0(k_r r)k_r dk_r\\ &= \int_0^\infty [ik_z A^+ e^{ik_z z} + k_r B^+ e^{i\tilde{k}_z z} - ik_z A^- e^{-ik_z z} + k_r B^- e^{-i\tilde{k}_z z}]J_0(k_r r)k_r dk_r\end{aligned} \tag{A.2.15}$$

The integral representation for the normal and tangential stresses σ_{zz} and σ_{rz} follows Hook's law. The partial derivatives of the displacement are:

$$\frac{\partial w^s(r,z)}{\partial z} = \int_0^\infty [-k_z^2 A^+ e^{ik_z z} + ik_r \tilde{k}_z B^+ e^{i\tilde{k}_z z} - k_z^2 A^- e^{-ik_z z} - ik_r \tilde{k}_z B^- e^{-i\tilde{k}_z z}]J_0(k_r r)k_r dk_r \tag{A.2.16}$$

$$\frac{\partial w^s(r,z)}{\partial r} = \int_0^\infty [-ik_r k_z A^+ e^{ik_z z} - k_r^2 B^+ e^{i\tilde{k}_z z} + ik_r k_z A^- e^{-ik_z z} - k_r^2 B^- e^{-i\tilde{k}_z z}]J_1(k_r r)k_r dk_r \tag{A.2.17}$$

$$\frac{\partial u^s(r,z)}{\partial z} = \int_0^\infty [-ik_r k_z A^+ e^{ik_z z} + \tilde{k}_z^2 B^+ e^{i\tilde{k}_z z} + ik_r k_z A^- e^{-ik_z z} + \tilde{k}_z^2 B^- e^{-i\tilde{k}_z z}]J_1(k_r r)k_r dk_r \tag{A.2.18}$$

$$\begin{aligned}\frac{1}{r}\frac{\partial(ru^s(r,z))}{\partial r} &= \frac{1}{rk_r}\frac{\partial(rk_r u^s(r,z))}{\partial r}\\ &= \int_0^\infty [-k_r^2 A^+ e^{ik_z z} - ik_r\tilde{k}_z B^+ e^{i\tilde{k}_z z}\\ &\quad - k_r^2 A^- e^{-ik_z z} + ik_r\tilde{k}_z B^- e^{-i\tilde{k}_z z}]J_0(k_r r)k_r dk_r\end{aligned} \tag{A.2.19}$$

$$\begin{aligned}\sigma_{zz}(r,z) &= (\lambda+2\mu)\frac{\partial w^s(r,z)}{\partial z} + \lambda\frac{1}{r}\frac{\partial(ru^s(r,z))}{\partial r}\\ &= \int_0^\infty [\underbrace{(-\lambda k_z^2 - \lambda k_r^2 - 2\mu k_z^2)}_{C_1}(A^+e^{ik_z z} + A^- e^{-ik_z z})\\ &\quad + \underbrace{2i\mu k_r\tilde{k}_z}_{C_2}(B^+e^{i\tilde{k}_z z} - B^- e^{-i\tilde{k}_z z})]J_0(k_r r)k_r dk_r\\ &= \int_0^\infty [C_1 A^+ e^{ik_z z} + C_2 B^+ e^{i\tilde{k}_z z} + C_1 A^- e^{-ik_z z} - C_2 B^- e^{-i\tilde{k}_z z}]J_0(k_r r)k_r dk_r\end{aligned} \tag{A.2.20}$$

$$\begin{aligned}\sigma_{rz}(r,z) &= \mu(\frac{\partial u^s(r,z)}{\partial z} + \frac{\partial w^s(r,z)}{\partial r})\\ &= \mu\int_0^\infty [\underbrace{-2ik_r k_z}_{C_3}(A^+e^{ik_z z} - A^- e^{-ik_z z})\\ &\quad - \underbrace{(k_r^2 - \tilde{k}_z^2)}_{C_4}(B^+e^{i\tilde{k}_z z} + B^- e^{-i\tilde{k}_z z})]J_1(k_r r)k_r dk_r\\ &= \mu\int_0^\infty [C_3 A^+ e^{ik_z z} - C_4 B^+ e^{i\tilde{k}_z z} - C_3 A^- e^{-ik_z z} - C_4 B^- e^{-i\tilde{k}_z z}]J_1(k_r r)k_r dk_r.\end{aligned} \tag{A.2.21}$$

The presented solution allows for an exact implementation of the boundary conditions between the layers. This is in contrast to finite-difference discretization, which is often used in acoustic propagation models. Therefore, one can study the interaction of the wavefields in the different media in a straight forward manner and without any numerical approximations.

■ A.2.2 Source representation

In this work, a compressional wave point source is used. The medium response for such source, in terms of compressional-wave potential, is

$$\hat{\Phi}(k_r,z) = \frac{S_\omega}{4\pi}\int_0^\infty \frac{e^{ik_z|z-z_s|}}{ik_z}J_0(k_r r)k_r dk_r, \tag{A.2.22}$$

where z_s is the source depth, and $S_\omega = S(\omega)$ is the frequency-domain source function. Depending on its position, the expressions for the medium response can be derived using equations A.2.1, A.2.2, and Hooke's law. The acoustic response to a point source will take the following form:

$$\begin{aligned}\hat{w}^f(r,z) &= \frac{S_\omega}{4\pi}\int_0^\infty sign(z-z_s)e^{ik_z|z-z_s|}J_0(k_r r)k_r dk_r \\ \hat{\sigma}^f(r,z) &= -\frac{S_\omega \rho\omega^2}{4\pi}\int_0^\infty \frac{e^{ik_z|z-z_s|}}{ik_z}J_0(k_r r)k_r dk_r.\end{aligned} \tag{A.2.23}$$

The elastic response is represented by:

$$\begin{aligned}\hat{w}^s(r,z) &= \frac{S_\omega}{4\pi}\int_0^\infty \text{sign}(z-z_s)e^{ik_z|z-z_s|}J_0(k_r r)k_r dk_r \\ \hat{u}^s(r,z) &= -\frac{S_\omega k_r}{4\pi}\int_0^\infty \frac{e^{ik_z|z-z_s|}}{ik_z}J_1(k_r r)k_r dk_r \\ \hat{\sigma}_{zz}(r,z) &= \frac{S_\omega}{4\pi}\int_0^\infty C_1\frac{e^{ik_z|z-z_s|}}{ik_z}J_0(k_r r)k_r dk_r \\ \hat{\sigma}_{rz}(r,z) &= -\frac{S_\omega \mu}{4\pi}\int_0^\infty 2k_r \text{sign}(z-z_s)e^{ik_z|z-z_s|}J_1(k_r r)k_r dk_r\end{aligned} \tag{A.2.24}$$

Source functions like an S-wave point source, and a double-couple force will generate different wavefields and radiation patterns that will affect the radiated energy

Derivatives for $\hat{\sigma}_{zz}$

$$\begin{aligned}\frac{\partial \hat{w}^s(r,z)}{\partial z} &= \frac{\partial}{\partial z}\left[\frac{S_\omega}{4\pi}\int_0^\infty \text{sign}(z-z_s)e^{ik_z|z-z_s|}J_0(k_r r)k_r dk_r\right] \\ &= \frac{S_\omega}{4\pi}\int_0^\infty [\underbrace{2\delta(z-z_s)}_{if\, z\neq z_s \to =0}e^{ik_z|z-z_s|} \\ &\quad + \underbrace{\text{sign}(z-z_s)^2}_{if\, z\neq z_s \to >0} ik_z e^{ik_z|z-z_s|}]J_0(k_r r)k_r dk_r \\ &= -\frac{S_\omega k_z^2}{4\pi}\int_0^\infty \frac{e^{ik_z|z-z_s|}}{ik_z}J_0(k_r r)k_r dk_r \\ \frac{1}{r}\frac{\partial(r\hat{u}(r,z))}{\partial r} &= \frac{1}{rk_r}\frac{\partial(rk_r\hat{u}(r,z))}{\partial r} \\ &= \frac{1}{rk_r}rk_r k_r(-\frac{S_\omega k_r}{4\pi})\int_0^\infty \frac{e^{ik_z|z-z_s|}}{ik_z}J_0(k_r r)k_r dk_r \\ &= -\frac{S_\omega}{4\pi}\int_0^\infty k_r^2\frac{e^{ik_z|z-z_s|}}{ik_z}J_0(k_r r)k_r dk_r\end{aligned}$$

into the atmosphere. Nevertheless, for simplicity, this study will use only the P wave point source.

■ A.2.3 Exact solutions

Following the derivation of the wavefield and source representations in ChaptersA.2.1 and A.2.2, we can now obtain exact solutions to sources in fluid and solid half-spaces with different boundary conditions. The following solutions are used as benchmarks for the coupled seismo-acoustic numerical scheme.

Homogeneous acoustic halfspace. Neumann (rigid) boundary conditions

A rigid boundary condition states that the displacement field on the boundary must vanish. Let us define the boundary at $z = 0$, and assume that no other sources are present in the medium (Sommerfeld radiation condition). If no other sources are present, the up-going wavefiled, A^- is zero. Now, the unknown amplitude A^+ can be calculated by writing the boundary conditions

$$\begin{aligned}
&w^f(k_r, z=0) + \hat{w}^f(k_r, z=0) = \\
&-ik_z A^- e^{-ik_z} + ik_z A^+ e^{ik_z z} + \frac{S_\omega}{4\pi}\mathrm{sign}(z - z_s)e^{ik_z|z-z_s|} = 0 \\
&\downarrow \\
&ik_z A^+ - \frac{S_\omega}{4\pi}e^{ik_z|z_s|} = 0 \\
&\downarrow \\
&A^+ = \frac{S_\omega}{ik_z 4\pi}e^{ik_z|z_s|}.
\end{aligned} \tag{A.2.25}$$

The acoustic wavefield can be computed by substituting this solution in any of the integral equations A.2.6 or A.2.7.

Homogeneous acoustic halfspace. Dirichlet (free) boundary conditions

A free-surface boundary condition states that the stress field on the boundary must vanish. Let us define the boundary at $z = 0$, and assume that no other sources are present in the medium (Sommerfeld radiation condition). If no other sources are present, the up-going wavefiled, A^- is zero. Now, the unknown amplitude A^+ can be calculated by writing the boundary conditions

$$
\begin{aligned}
&P^f(k_r, z=0) + \hat{P}^f(k_r, z=0) = \rho\omega^2(A^- e^{-ik_z} + A^+ e^{ik_z z}) - \frac{\rho\omega^2 S_\omega}{4\pi}\frac{e^{ik_z|z-z_s|}}{ik_z} = 0 \\
&\downarrow \\
&A^+ - \frac{S_\omega}{4\pi}\frac{e^{ik_z|-z_s|}}{ik_z} = 0 \\
&\downarrow \\
&A^+ = \frac{S_\omega}{ik_z 4\pi} e^{ik_z|z_s|}.
\end{aligned}
\tag{A.2.26}
$$

The acoustic wavefield can be computed by substituting this solution in any of the integral equations A.2.6 or A.2.7.

Homogeneous elastic halfspace. Neumann (rigid) boundary conditions

The rigid surface boundary conditions for a homogeneous elastic halfspace consist of two equations. Both the vertical and horizontal displacements are set to zero. After omitting the upgoing waves A^- and B^-, the equations take the form:

$$
\begin{aligned}
&u^s(k_r, z=0) + \hat{u}^s(k_r, z=0) = -k_r A^+ e^{ik_z z} - i\tilde{k}_z B^+ e^{i\tilde{k}_z z} - \frac{S_\omega k_r}{4\pi}\frac{e^{ik_z|z-z_s|}}{ik_z} = 0 \\
&w^s(r, z=0) + \hat{w}^s(r, z=0) = ik_z A^+ e^{ik_z z} + k_r B^+ e^{i\tilde{k}_z z} + \frac{S_\omega}{4\pi}\mathrm{sign}(z-z_s) e^{ik_z|z-z_s|} = 0 \\
&\downarrow \\
&A^+ = \left(\frac{i\tilde{k}_z}{2\pi\left(\frac{k_z\tilde{k}_z}{k_r} + k_r\right)} - \frac{1}{4\pi i k_r}\right) S_\omega e^{ik_z|z_s|} \\
&B^+ = \frac{S_\omega}{2\pi\left(\frac{k_z\tilde{k}_z}{k_r} + k_r\right)} e^{ik_z|z_s|}.
\end{aligned}
\tag{A.2.27}
$$

The displacement or stress wavefileds can be obtained by substituting these solutions to one of the integral equations A.2.14, A.2.15, A.2.20, and A.2.21.

Homogeneous elastic halfspace. Dirichlet (free) boundary conditions

$$
\begin{aligned}
&\sigma_{zz}(k_r, z=0) + \hat{\sigma}_{zz}(k_r, z=0) = C_1 A^+ e^{ik_z z} + C_2 B^+ e^{i\tilde{k}_z z} + \frac{C_1 S_\omega}{4\pi} \frac{e^{ik_z|z-z_s|}}{ik_z} = 0 \\
&\sigma_{rz}(k_r, z=0) + \hat{\sigma}_{rz}(k_r, z=0) = C_3 A^+ e^{ik_z z} - C_4 B^+ e^{i\tilde{k}_z z} - \frac{S_\omega 2k_r}{4\pi} \mathrm{sign}(z-z_s) e^{ik_z|z-z_s|} = 0 \\
&\downarrow \\
&C_1 A^+ + C_2 B^+ + C_1 S_\omega \frac{e^{ik_z|z_s|}}{4\pi i k_z} = 0 \\
&C_3 A^+ - C_4 B^+ + \frac{k_r S_\omega}{2\pi} e^{ik_z|z_s|} = 0 \\
&\downarrow \\
&A^+ = -\left(\frac{C_1}{4\pi i k_z} + \frac{C_2}{C_2 C_3 + C_4} \left(\frac{k_r}{2\pi} - \frac{C_1 C_3}{4\pi i k_z} \right) \right) S_\omega e^{ik_z|z_s|} \\
&B^+ = \frac{1}{C_2 C_3 + C_4} \left(\frac{k_r}{2\pi} - \frac{C_1 C_3}{4\pi i k_z} \right) S_\omega e^{ik_z|z_s|}
\end{aligned}
\tag{A.2.28}
$$

The displacement or stress wavefileds can be obtained by substituting these solutions to one of the integral equations A.2.14, A.2.15, A.2.20, and A.2.21.

Coupled homogeneous elastic and acoustic halfspaces.

The BC at a solid-fluid interface are the continuity of vertical displacement and normal stress, and the vanishing of the tangential stress. Assuming radiation conditions in both half-spaces implies that there are no upgoing waves in the solid half-space (A^{s-} and B^{s-} are zero), and no downgoing waves in the fluid half-space ($A^{f+} = 0$). These BC provide us with a set of three equation for the three unknowns A^{s+}, B^{s+},and A^{f-}.

$$
\begin{aligned}
&w^f(k_r, z=0) = w^s(k_r, z=0) + \hat{w}^s(k_r, z=0)\\
&\sigma^f_{zz}(k_r, z=0) = \sigma^s_{zz}(k_r, z=0) + \hat{\sigma}^s_{zz}(k_r, z=0)\\
&0 = \sigma^s_{rz}(k_r, z=0) + \hat{\sigma}^s_{rz}(k_r, z=0)\\
&\downarrow\\
&-ik^f_z A^{f-} = ik^s_z A^{s+} + k_r B^{s+} + \frac{S_\omega}{4\pi}\mathrm{sign}(z-z_s)e^{ik^s_z|z-z_s|}\\
&-\rho^f\omega^2 A^{f-} = C_1 A^{s+} + C_2 B^{s+} + \frac{C_1 S_\omega}{4\pi}\frac{e^{ik^s_z|z-z_s|}}{ik_z}\\
&0 = C_3 A^{s+} - C_4 B^{s+} - \frac{S_\omega 2k_r}{4\pi}\mathrm{sign}(z-z_s)e^{ik^s_z|z-z_s|}\\
&\downarrow\\
&A^{s+} =\\
&\frac{1}{\frac{\rho^f\omega^2}{ik^f_z}\left(ik^s_z + \frac{k_r C_3}{C_4}\right) - \left(C_1 - \frac{C_2 C_3}{C_4}\right)}\left(\left(\frac{2k_r C_2}{C_4} - \frac{C_1}{ik^s_z}\right) - \frac{\rho^f\omega^2}{ik^f_z}\left(\frac{2k_r^2}{C_4} - 1\right)\right)\frac{C_1 S_\omega}{4\pi}\frac{e^{ik^s_z|z-z_s|}}{ik_z}\\
&B^{s+} = \frac{1}{C_4}\left(C_3 A^{s+} + \frac{S_\omega 2k_r}{4\pi}e^{ik^s_z|z-z_s|}\right)\\
&A^{f-} = -\frac{1}{ik^f_z}\left(\left(ik^s_z + \frac{k_r C_3}{C_4}A^{s+}\right) + \left(\frac{2k_r^2}{C_4} - 1\right)\frac{S_\omega 2k_r}{4\pi}e^{ik^s_z|z-z_s|}\right)
\end{aligned}
\tag{A.2.29}
$$

The acoustic and elastic wavefields can be computed by substituting these solutions to one of the integral equations A.2.6, A.2.7, A.2.14, A.2.15, A.2.20, and A.2.21.

B

Supplemental information to: On the infrasound detected from the 2013 and 2016 DPRKs underground nuclear tests

Introduction This supporting information provides a quantitative evaluation of relative source depth comparing the 2013 and 2016 cases, in order to support the hypothesis that the 2016 test occurred deeper than the 2013 test. Besides the greater depth, we acknowledge alternative explanations of difference in yield or seismic coupling. Following the analysis in the supplemental information, one would estimate a factor 2 difference in source amplitude, keeping other variables equal. Such a value would be inconsistent with seismic data, especially considering the uncertainties associated with seismic moment magnitude estimation (0.1-0.2 units).

In this note, we derive an expression for the relative depth of the 2016 underground test, using the 2013 test as a reference. The expression is a function of the ratio of measured pressures in the far field and the relative propagation efficiency. The expression assumes a constant impedance contrast between ground and air as well as constant source amplitude. The expression is evaluated for two cases of stratospheric propagation in 2013 and 2016.

B.1 Propagation efficiency and pressure ratios

Recall that transmission loss (TL) due to propagation in a medium [*Jensen et al.*, 2011] is defined as:

$$\mathrm{TL} = 20\log_{10}\left(\frac{p_r}{p_s}\right) \tag{B.1.1}$$

Here, p_r and p_s correspond to the pressure at receiver and source positions, respectively.

Consider the two following equations, relating source and receiver pressure levels:

$$\mathrm{TL}_{2013} = 20\log_{10}\left(\frac{p_{r,2013}}{p_{s,2013}}\right) \tag{B.1.2}$$

and

$$\mathrm{TL}_{2016} = 20\log_{10}\left(\frac{p_{r,2016}}{p_{s,2016}}\right) \tag{B.1.3}$$

Combining equations B.1.2 and B.1.3:

$$\Delta\mathrm{TL} = 20\log_{10}\left[\left(\frac{p_{r,2016}}{p_{s,2016}}\right) / \left(\frac{p_{r,2013}}{p_{s,2013}}\right)\right] \tag{B.1.4}$$

Here, $\Delta\mathrm{TL} = \mathrm{TL}_{2016} - \mathrm{TL}_{2013}$. This leads, after some straightforward algebra, to:

$$P \equiv \frac{p_{s,2013}}{p_{s,2016}} = 10^{\frac{\Delta\mathrm{TL}}{20}} \times \frac{p_{r,2013}}{p_{r,2016}} = Q \times \frac{p_{r,2013}}{p_{r,2016}} \tag{B.1.5}$$

This relation expresses the ratio of amplitudes in the near field (s) as a function of ratio of amplitudes in the far field (r). In general, propagation factor Q scales the two ratios. It follows immediately that if $\Delta\mathrm{TL} = 0 \rightarrow Q = 1$. In this case, there is no difference in propagation efficiency, and thus the ratio of far field pressures equals the ratio of near field pressures. In other cases, propagation efficiency factor Q must be taken into account.

■ B.1.1 Stratospheric propagation

Consider the stratospheric propagation losses for propagation towards I45RU, as listed in Table 2.2. We find that $\mathrm{TL}_{2016} = -53.0$ dB, $\mathrm{TL}_{2013} = -47.9$ dB and hence $\Delta\mathrm{TL} = -5.1$ dB ($Q \approx 0.6$).

From Figure 4, it follows that $p_{r,_{2013}} \approx 0.02$ Pa. As no stratospheric arrival is clearly detected in 2016, this means that the stratospheric pressure has not exceeded the noise level. This implies an upper limit: $p_{r,_{2016}} \leq 0.005$ Pa. Substituting these numbers in equation B.1.5 yields $P \geq 2.2$.

B.2 Estimating relative depth from the pressure ratio

Also recall the impedance condition [*Jensen et al.*, 2011] for a plane wave with pressure p and vertical particle velocity w, in a medium with density ρ_0 and sound speed c:

$$p = \rho_0 c w \tag{B.2.1}$$

Now, the ratio of source pressures can be expressed as a ratio of particle velocities in the air:

$$P = \frac{p_{s,_{2013}}}{p_{s,_{2016}}} = \frac{\rho_{0,_{2013}} c_{_{2013}} w_{_{2013}}}{\rho_{0,_{2016}} c_{_{2016}} w_{_{2016}}} \tag{B.2.2}$$

Because of the continuity of vertical particle velocity, we can relate the particle velocity in the air to the particle velocity in the ground, through transmission coefficient $\mathcal{T}$. We also consider that the particle velocity w in the ground is in the near-field [*Lay and Wallace*, 1995], and is due to a source with amplitude A at distance r:

$$P = \frac{\rho_{0,_{2013}} c_{_{2013}} \mathcal{T}_{_{2013}} A_{_{2013}} r_{_{2013}}^{-2}}{\rho_{0,_{2016}} c_{_{2016}} \mathcal{T}_{_{2016}} A_{_{2016}} r_{_{2016}}^{-2}} \tag{B.2.3}$$

Next, we **assume** that the characteristic impedances $\rho_0 c$ are invariant over 2013 and 2016 (so $\mathcal{T}_{_{2013}} = \mathcal{T}_{_{2016}}$). This is justified as the source is in the same region in 2013 and 2016. Moreover, we **assume** that the amplitude factor $A_{_{2013}} = A_{_{2016}}$. We justify this, based on the moment tensor solution; comparable seismic moment magnitudes have been estimated for the 2013 ($M_w = 4.7$) and 2016 ($M_w = 4.71$) test explosions. A more complete analysis of the source parameters can be found on the IRIS event summary pages [*IRIS*, 2013, 2016]. Now, equation B.2.3 reduces to:

$$P = \frac{r_{_{2013}}^{-2}}{r_{_{2016}}^{-2}} = \frac{r_{_{2013}}^{-2}}{(r_{_{2013}} + \Delta r)^{-2}} \tag{B.2.4}$$

Solving for Δr:

$$\Delta r = -r_{_{2013}} \pm r_{_{2013}} \sqrt{P} \tag{B.2.5}$$

which equals:

$$\frac{r_{_{2016}}}{r_{_{2013}}} = \pm\sqrt{P} = \sqrt{10^{\frac{\Delta \mathrm{TL}}{20}} \times \frac{p_{r,_{2013}}}{p_{r,_{2016}}}} \tag{B.2.6}$$

Recalling that $P \geq 2.2$, we find:

$$\frac{r_{2016}}{r_{2013}} \geq 1.5 \tag{B.2.7}$$

Following this analysis, we estimate that the 2016 test took place at least 1.5 times deeper than the 2013 test. Assuming a minimum source depth of 450 m for the 2013 test, based on hydrodynamic simulation results [*Rougier et al.*, 2011] and the 2013 yield estimate of 10 kT TNT (Table 2.1), this would imply that the 2016 explosion would have occurred at least 225 m deeper.

C

Supplemental information to: A Seismo-Acoustic Analysis of the 2017 North Korean Nuclear Test

Using concurrent microbarom signals from Typhoon Sanvu to constrain atmospheric infrasound propagation conditions

During the 2017 North Korean nuclear test, the stratosphere was in a state of transition from summer to winter and the stratospheric vortex was relatively weak. As long-range infrasound propagation is largely conditioned by the strength and the direction of the stratospheric vortex, this implies that propagation from the test site to I45RU may have occurred along unexpected paths. The mode of propagation can be difficult to decipher from the seismo-acoustic signals alone, as is discussed in the article.

To supplement our understanding of infrasound propagation conditions during the test, it can be insightful to analyse concurrent infrasonic signals that were detected at the infrasound array. Indeed, all signals must have propagated through the same atmosphere, albeit from different directions. In particular, continuous signals in the microbarom band (0.1-0.4 Hz) may provide some additional evidence about the mode of propagation, be it stratospheric or thermospheric [*Donn and Rind*, 1972]. It appears that the diurnal amplitude variations are strongly sensitive to the return height. This is a consequence of the interplay between the varying return height due to the atmospheric tides and infrasonic attenuation in the thermosphere. It allows that semi-diurnal amplitude variations are associated with thermospheric ducting, whereas diurnal variations are associated with stratospheric propagation.

In the 1970s, William Donn and David Rind used continuous signals from ocean storms as a means to monitor the state of the upper atmosphere [*Donn and Rind*,

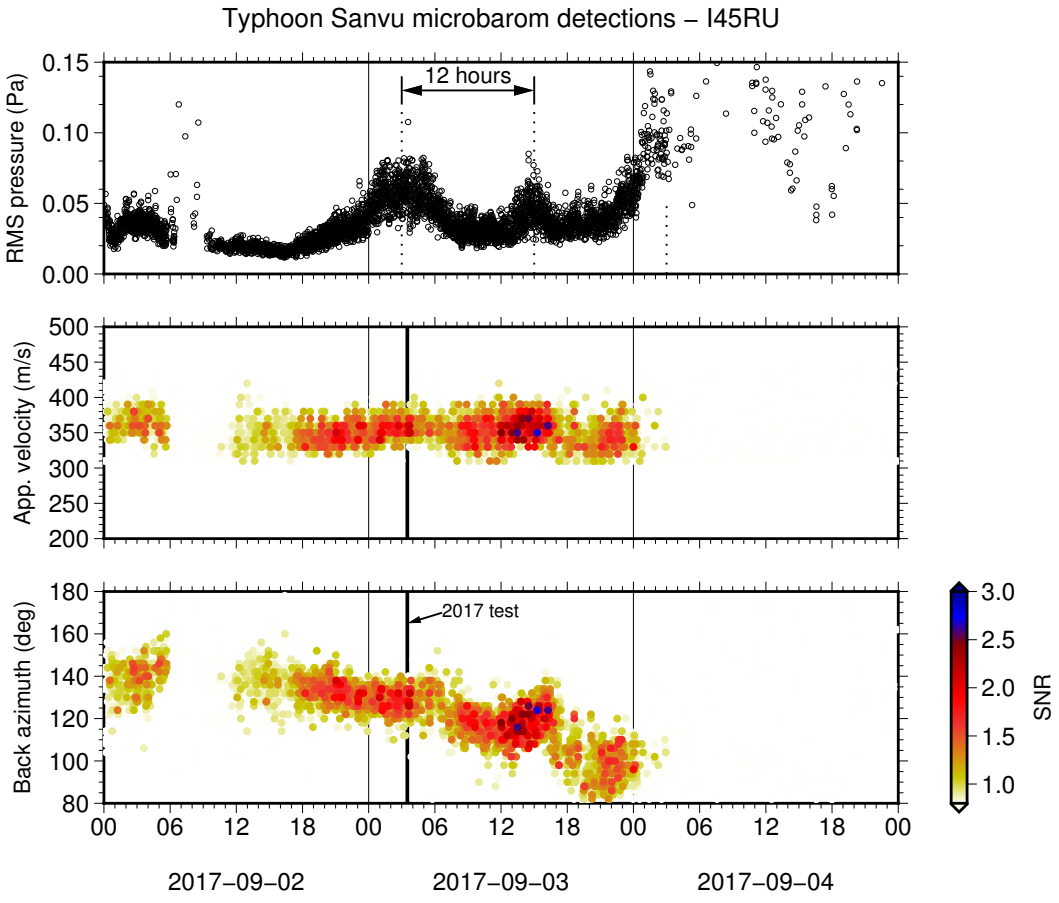

Figure C.1: *I45RU array processing in the microbarom band (0.1-0.4 Hz) during the first week of September 2017, showing microbarom signals from Typhoon Sanvu. This typhoon was active from 31 August through 3 September 2017 and strong signals were observed during the nuclear test (vertical line). The best beam amplitude shows a semi-diurnal trend that is indicative of thermospheric propagation.*

1972]. The method was applied by [*Smets and Evers*, 2014] to analyze the lifecycle of the 2009 Sudden Stratospheric Warming (SSW). During the 2017 North Korean nuclear test, Typhoon Sanvu was active in the Pacific basin, leading to continuous microbarom observations on array I45RU (Figure C.1). The semi-diurnal variation in best beam amplitudes suggest that these signals have propagated through the thermospheric waveguide. This independent observation is in line with the weak stratospheric vortex conditions, as described in the article.

D

Supplemental information to: Long-range atmospheric infrasound propagation from subsurface sources

The effect of viscoelastic attenuation is tested by introducing complex Lamé parameters and complex medium wavenumbers. Their imaginary part is derived from empirical Q factor relations [*Brocher*, 2008; *Shani-Kadmiel et al.*, 2014]. Based on the seismic velocities of the soft layer in Table 3.2, quality factors of $Q_p = 78$ and $Q_s = 39$ are calculated for pressure and shear waves, respectively. A narrowband simulation is carried out accounting for attenuation. Its effect is demonstrated in Figure D.1. The "ringing" in the blue curve (no attenuation) is the signature of the radiated surface wave. Despite its large amplitude, small features that correspond to the tropospheric and stratospheric propagation are still visible. Attenuation has two main effects on the coupled waves. (1) rapid decay of the surface wave leads to no observable signal from it. (2) the radiated acoustic waves are attributed to coupling from inhomogeneous body waves.

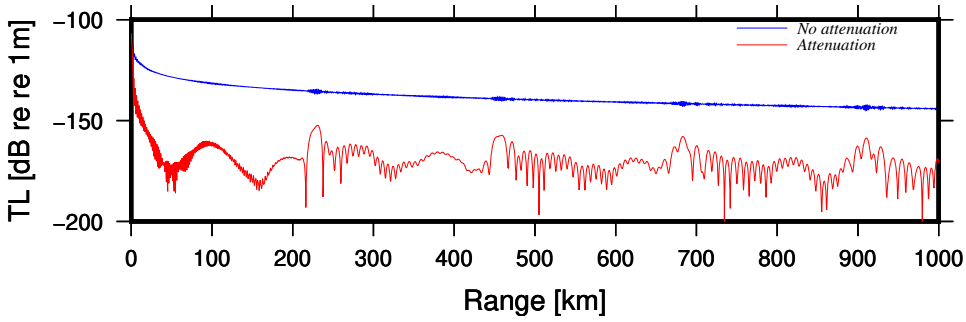

Figure D.1: *Results show that the radiated acoustic waves are attributed to coupling from inhomogeneous body waves while the contribution from surface waves is negligible. Moreover, depending on the source depth , a decrease of* $15 - 25dB$ *in TL is obtained*

E

Supplemental information to: Probabilistic inversion for submerged source depth and strength from infrasound observations

E.1 Stations position

Figure E.1 shows the lateral position of the stations, and the absolute pressure curves for propagation in the stations directions.

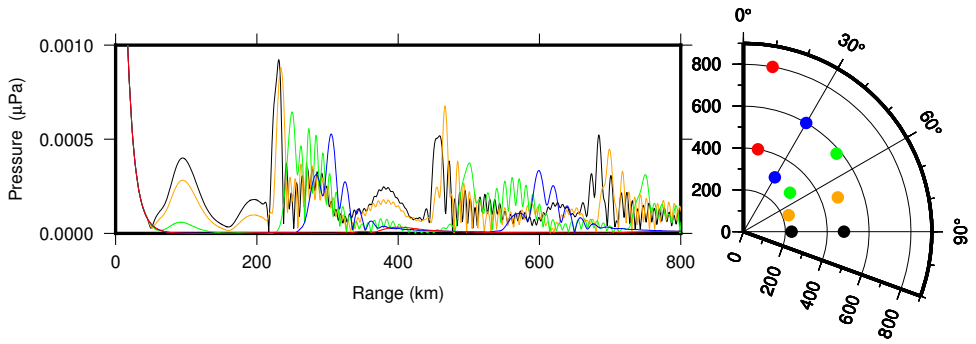

Figure E.1: *Lateral position of the stations, and the corresponding absolute pressure curves from a 0.5 Hz source at a depth of 500 m. The colors of the curves correspond to the colors of the stations.*

E.2 Number of outliers

The following Tables E.1 and E.2 show the number of outliers for each set up that is presented in Figures 4.4 and 4.5

Table E.1: *Number of outliers for each set up in Fig. 4.4 .*

SNR	1				2				3				4				5			
	f_1	f_2	f_3	comb	f1	f_2	f_3	comb	f1	f_2	f_3	comb	f1	f_2	f_3	comb	f1	f_2	f_3	comb
outliers S	-	-	-	58	-	-	-	107	-	-	-	104	-	-	74	35	-	-	98	25
outliers Z_s	5	4	2	2	12	-	-	-	1	-	-	-	-	-	-	-	-	-	-	-

Table E.2: *Number of outliers for each set up in Fig. 4.5 .*

SNR	1			2			3			4			5		
Num. of stations	1	5	10	1	5	10	1	5	10	1	5	10	1	5	10
outliers S	-	44	44	34	172	127	24	122	39	51	65	8	274	27	3
outliers Z_s	-	-	-	1	-	-	-	-	-	-	-	-	-	-	-

Bibliography

Achenbach, J. (1984), *Wave Propagation in Elastic Solids.*, 440 pp., Elsevier Science.

Aki, K., and P. G. Richards (2002), *Quantitative seismology*, 700 pp., University Science Books.

Alcoverro, B., P. Marysevich, and Y. Starovoit (2005), Mechanical Sensitivity of Microbarometers MB2000 (DASE, France) and Chaparral5 (USA) to Vertical and Horizontal Ground Motion, *Inframatics: The newsletter of subaudible sound*, *9*(09), 1–10.

Arrowsmith, S., R. Whitaker, and R. Stead (2011), Infrasound as a Depth Discriminant, in *Proceedings of the 2011 Monitoring Research Review - Ground-Based Nuclear Explosion Monitoring Technologies, 13-15 September 2011, Tucson, AZ*, pp. 755–765.

Artru, J., T. Farges, and P. Lognonné (2004), Acoustic waves generated from seismic surface waves: Propagation properties determined from Doppler sounding observations and normal-mode modelling, *Geophysical Journal International*, *158*(3), 1067–1077, doi:10.1111/j.1365-246X.2004.02377.x.

Assink, J., R. Waxler, and D. Velea (2017), A wide-angle high Mach number modal expansion for infrasound propagation, *The Journal of the Acoustical Society of America*, *141*(3), 1781–1792.

Assink, J., G. Averbuch, S. ShaniKadmiel, P. Smets, and L. Evers (2018), A SeismoAcoustic Analysis of the 2017 North Korean Nuclear Test, *Seismological Research Letters*, *89*(6), 2025–2033, doi:10.1785/0220180137.

Assink, J. D. (2012), Infrasound as upper atmospheric monitor, Phd thesis, University of Mississippi.

Assink, J. D., R. Waxler, W. G. Frazier, and J. Lonzaga (2013), The estimation of upper atmospheric wind model updates from infrasound data, *Journal of Geophysical Research Atmospheres*, *118*(19), 10,707–10,724, doi:10.1002/jgrd.50833.

Assink, J. D., R. Waxler, P. Smets, and L. G. Evers (2014), Bidirectional infrasonic ducts associated with sudden stratospheric warming events, *J. Geophys. Res. Atmos.*, *119*(3), 1140–1153, doi:10.1002/2013jd021062.

Assink, J. D., G. Averbuch, P. S. M. Smets, and L. G. Evers (2016), On the infrasound detected from the 2013 and 2016 DPRK's underground nuclear tests, *Geophysical Research Letters*, *43*(7), 3526–3533, doi:10.1002/2016GL068497.

Averbuch, G., J. D. Assink, P. S. M. Smets, and L. G. Evers (2018), Extracting low signal-to-noise ratio events with the Hough transform from sparse array data, *GEOPHYSICS*, *83*(3), WC43–WC51, doi:10.1190/geo2017-0490.1.

Averbuch, G., Y. Ben-Horin, P. S. M. Smets, and L. G. Evers (2019), The Mount Meron Infrasound Array: an infrasound array without a noise reduction system., *Geophysical Journal International*, doi:10.1093/gji/ggz350.

Ben-Menahem, A., and S. J. Singh (1981), *Seismic Waves and Sources*, 1108 pp., Springer New York.

Ben-Menahem, A., and M. Vered (1975), Modeling of atmospheric nuclear explosions over a mountainous region by vertical and horizontal single forces, *Bulletin of the Seismological Society of America*, *65*(4), 971–980.

Benioff, H., M. Ewing, and F. Press (1951), Sound Waves in the Atmosphere Generated by a Small Earthquake., *Proceedings of the National Academy of Sciences of the United States of America*, *37*(9), 600–3, doi:10.1073/PNAS.37.9.600.

Biot, M. A. (1952), The interaction of Rayleigh and Stoneley waves in the ocean bottom*, *Bulletin of the Seismological Society of America*, *42*(1), 81–93.

Blackstock, D. T. (2000), *Fundamentals of physical acoustics*, 541 pp., Wiley.

Bolt, B. A. (1964), Seismic Air Waves from the Great 1964 Alaskan Earthquake, *Nature*, *202*(4937), 1095–1096, doi:10.1038/2021095a0.

Bowers, D., and N. D. Selby (2009), Forensic Seismology and the Comprehensive Nuclear-Test-Ban Treaty, *Annual Review of Earth and Planetary Sciences*, *37*(1), 209–236, doi:10.1146/annurev.earth.36.031207.124143.

Bowman, D. C. (2019), Yield and Emplacement Depth Effects on Acoustic Signals from Buried Explosions in Hard Rock, *Bulletin of the Seismological Society of America*, doi:10.1785/0120180285.

Brekhovskikh, L., and Y. Lysanov (1982), *The Ocean as an Acoustic Medium*, 252 pp., Springer Berlin Heidelberg, Berlin, Heidelberg, doi:10.1007/978-3-662-02342-6.

Brekhovskikh, L. M., and O. A. Godin (1990), *Acoustics of Layered Media I*, *Springer Series on Wave Phenomena*, vol. 5, Springer Berlin Heidelberg, Berlin, Heidelberg, doi:10.1007/978-3-642-52369-4.

Brekhovskikh, L. M., and O. A. Godin (1999), *Acoustics of Layered Media II : Point Sources and Bounded Beams*, 524 pp., Springer Berlin Heidelberg, doi:10.1007/978-3-662-03889-5.

Brocher, T. M. (2008), Key elements of regional seismic velocity models for long period ground motion simulations, *Journal of Seismology*, *12*(2), 217–221, doi:10.1007/s10950-007-9061-3.

Bromwich, T. J. I. (1898), On the Influence of Gravity on Elastic Waves, and, in particular on the Vibrations of an Elastic Globe, *Proceedings of the London Mathematical Society*, *s1-30*(1), 98–165, doi:10.1112/plms/s1-30.1.98.

Brower, N. G., D. E. Himberger, and W. G. Mayer (1979), Restrictions on the existence of leaky rayleigh waves, *IEEE Transactions on Sonics and Ultrasonics*, *263*(4), 306–308.

Brown, D. J., C. N. Katz, R. Le Bras, M. P. Flanagan, J. Wang, and A. K. Gault (2002), Infrasonic Signal Detection and Source Location at the Prototype International Data Centre, *Pure and Applied Geophysics*, *159*(5), 1081–1125, doi:10.1007/s00024-002-8674-2.

Brown, L. B., A. J. Gerrard, J. W. Meriwether, and J. J. Makela (2004), All-sky imaging observations of mesospheric fronts in OI 557.7 nm and broadband OH airglow emissions: Analysis of frontal structure, atmospheric background conditions, and potential sourcing mechanisms, *Journal of Geophysical Research D: Atmospheres*, *109*(19), 1–19, doi:10.1029/2003JD004223.

Buizza, R., M. Miller, and T. N. Palmer (1999), Stochastic representation of model uncertainties in the ECMWF Ensemble Prediction System, *QUARTERLY JOURNAL OF THE ROYAL METEOROLOGICAL SOCIETY*, *125*(560), 2887–2908.

Buizza, R., M. Leutbecher, and L. Isaksen (2008), Potential use of an ensemble of analyses in the ECMWF Ensemble Prediction System, *Quarterly Journal of the Royal Meteorological Society*, *134*(637), 2051–2066, doi:10.1002/qj.346.

Campus, P., and D. R. Christie (2009), Worldwide observations of infrasonic waves, in *Infrasound Monitoring for Atmospheric Studies*, pp. 185–234, Springer Netherlands, Dordrecht, doi:10.1007/978-1-4020-9508-5_6.

Carpenter, E. W. (1967), TELESEISMIC SIGNALS CALCULATED FOR UNDERGROUND, UNDERWATER, AND ATMOSPHERIC EXPLOSIONS, *GEOPHYSICS*, *32*(1), 17–32, doi:10.1190/1.1439854.

Caviglia, G., and A. Morro (1992), *Inhomogeneous Waves in Solids and Fluids*, WORLD SCIENTIFIC, doi:10.1142/1519.

Cerveny, V. (2001), *Seismic ray theory*, 724 pp., Cambridge University Press.

Che, I.-Y., T. S. Kim, J.-S. Jeon, and H.-I. Lee (2009), Infrasound observation of the apparent north korean nuclear test of 25 may 2009, *Geophysical Research Letters*, *36*(22), doi:10.1029/2009GL041017, l22802.

Che, I.-Y., J. Park, I. Kim, T. S. Kim, and H.-I. Lee (2014), Infrasound signals from the underground nuclear explosions of North Korea, *Geophysical Journal International*, *198*(1), 495–503, doi:10.1093/gji/ggu150.

Chunchuzov, I., S. Kulichkov, V. Perepelkin, O. Popov, P. Firstov, J. D. Assink, and E. Marchetti (2015), Study of the wind velocitylayered structure in the stratosphere, mesosphere, and lower thermosphere by using infrasound probing of the atmosphere, *Journal of Geophysical Research: Atmospheres*, *120*(17), 8828–8840, doi:10.1002/2015JD023276.

Collins, M. D. (1993), A split-step Padé solution for the parabolic equation method, *J. Acoust. Soc. Am.*, *93*(4), 1736–1742, doi:10.1121/1.406739.

Colosi, J. A. (2016), *Sound Propagation through the Stochastic Ocean*, Cambridge University Press, doi:10.1017/CBO9781139680417.

Cook, R. K. (1971), Infrasound Radiated During the Montana Earthquake of 1959 August 18, *Geophysical Journal of the Royal Astronomical Society*, *26*(1-4), 191–198, doi:10.1111/j.1365-246X.1971.tb03393.x.

Dahlman, O., P. Mykkeltveit, and H. Haak (2009), Monitoring Technologies, in *Nuclear Test Ban*, chap. 2, pp. 1–34, Springer, Dordrecht, doi:10.1007/978-1-4020-6885-0_2.

de GrootHedlin, C. (2008), Finite-difference time-domain synthesis of infrasound propagation through an absorbing atmosphere, *The Journal of the Acoustical Society of America*, *124*(3), 1430–1441, doi:10.1121/1.2959736.

Dessa, J. X., J. Virieux, and S. Lambotte (2005), Infrasound modeling in a spherical heterogeneous atmosphere, *Geophysical Research Letters*, *32*(12), 1–5, doi:10.1029/2005GL022867.

DiNapoli, F. R., and R. L. Deavenport (1980), Theoretical and numerical Green's function field solution in a plane multilayered medium, *The Journal of the Acoustical Society of America*, *67*(1), 92–105, doi:10.1121/1.383794.

Donn, W. L., and E. S. Posmentier (1964), Ground-coupled air waves from the Great Alaskan Earthquake, *Journal of Geophysical Research*, *69*(24), 5357–5361, doi:10.1029/JZ069i024p05357.

Donn, W. L., and D. Rind (1972), Microbaroms and the Temperature and Wind of the Upper Atmosphere, *J. Atmos. Sci.*, *29*(1), 156–172.

Douglas, A., D. J. Corbishley, C. Blamey, and P. D. Marshall (1972), Estimating the Firing Depth of Underground Explosions, *Nature*, *237*(5349), 26–28, doi:10.1038/237026a0.

Drob, D. P., J. T. Emmert, J. W. Meriwether, J. J. Makela, E. Doornbos, M. Conde, G. Hernandez, J. Noto, K. A. Zawdie, S. E. McDonald, J. D. Huba, and J. H. Klenzing (2015), An update to the Horizontal Wind Model (HWM): The quiet time thermosphere, *Earth and Space Science*, *2*(7), 301–319, doi:10.1002/2014EA000089.

Evers, L. G. (2008), The inaudible symphony: On the detection and source identification of atmospheric infrasound, Phd thesis, Delft University of Technology, The Netherlands.

Evers, L. G. (2014), Evanescent Wave Coupling in a Geophysical System, in *AGU Fall Meeting Abstracts*, vol. 1, p. 3871.

Evers, L. G., and P. Siegmund (2009), Infrasonic signature of the 2009 major sudden stratospheric warming, *Geophysical Research Letters*, *36*(23), n/a–n/a, doi:10.1029/2009GL041323, l23808.

Evers, L. G., A. R. J. van Geyt, P. Smets, and J. T. Fricke (2012), Anomalous infrasound propagation in a hot stratosphere and the existence of extremely small shadow zones, *Journal of Geophysical Research: Atmospheres*, *117*(D6), doi:10.1029/2011JD017014, d06120.

Evers, L. G., D. Brown, K. D. Heaney, J. D. Assink, P. S. Smets, and M. Snellen (2014), Evanescent wave coupling in a geophysical system: Airborne acoustic signals from the Mw 8.1 Macquarie Ridge earthquake, *Geophysical Research Letters*, *41*(5), 1644–1650, doi:10.1002/2013GL058801.

Ewing, M., and J. L. Worzel (1948), LONG-RANGE SOUND TRANSMISSION, in *Propagation of Sound in the Ocean*, Geological Society of America, doi:10.1130/MEM27-3-p1.

Ewing, W. M., W. S. Jardetzky, F. Press, and A. Beiser (1957), Elastic Waves in Layered Media, *Physics Today*, *10*(12), 27–28, doi:10.1063/1.3060203.

Fee, D., and R. S. Matoza (2013), An overview of volcano infrasound: From hawaiian to plinian, local to global, *Journal of Volcanology and Geothermal Research*, *249*, 123–139, doi:10.1016/J.JVOLGEORES.2012.09.002.

Ford, S. R., A. J. Rodgers, H. Xu, D. C. Templeton, P. Harben, W. Foxall, and R. E. Reinke (2014), Partitioning of seismoacoustic energy and estimation of yield and height-of-burst/depth-of-burial for near-surface explosions, *Bulletin of the Seismological Society of America*, *104*(2), 608–623, doi:10.1785/0120130130.

Frank, S. D., R. I. Odom, and J. M. Collis (2013), Elastic parabolic equation solutions for underwater acoustic problems using seismic sources, *The Journal of the Acoustical Society of America*, *133*(3), 1358–1367, doi:10.1121/1.4790355.

Fricke, J., L. Evers, P. Smets, K. Wapenaar, and D. Simons (2014), Infrasonic interferometry applied to microbaroms observed at the Large Aperture Infrasound Array in the Netherlands, *Journal of Geophysical Research: Atmospheres*, *119*, 9654–9665, doi:10.1002/2014JD021663.1.

Fuchs, K., and G. Muller (1971), Synthetic Seismograms with the Reflectivity Method and Comparison with Observations, *Geophys. J. Int.*, pp. 417–433.

Gibbons, S., F. Pabian, S. Näsholm, T. Kværna, and S. Mykkeltveit (2017), Accurate relative location estimates for the North Korean nuclear tests using empirical slowness corrections, *Geophysical Journal International*, *208*(1), 101–117, doi:10.1093/gji/ggw379.

Godin, O. A. (2002), An effective quiescent medium for sound propagating through an inhomogeneous, moving fluid, *The Journal of the Acoustical Society of America*, *112*(4), 1269–1275, doi:10.1121/1.1504853.

Godin, O. A. (2006), Anomalous transparency of water-air interface for low-frequency sound, *Physical review letters*, *97*(16), 164,301.

Godin, O. A. (2008), Sound transmission through water–air interfaces: New insights into an old problem, *Contemporary Physics*, *49*(2), 105–123.

Godin, O. A. (2011), Low-frequency sound transmission through a gas-solid interface, *The Journal of the Acoustical Society of America*, *129*(2), EL45–EL51, doi:10.1121/1.3535578.

Green, D. N., J. Guilbert, A. Le Pichon, O. Sebe, and D. Bowers (2009), Modelling Ground-to-Air Coupling for the Shallow ML 4.3 Folkestone, United Kingdom, Earthquake of 28 April 2007, *Bulletin of the Seismological Society of America*, *99*(4), 2541–2551, doi:10.1785/0120080236.

Green, D. N., J. Vergoz, R. Gibson, A. Le Pichon, and L. Ceranna (2011), Infrasound radiated by the Gerdec and Chelopechene explosions: Propagation along unexpected paths, *Geophysical Journal International*, *185*(2), 890–910.

Green, D. N., L. G. Evers, D. Fee, R. S. Matoza, M. Snellen, P. Smets, and D. Simons (2013), Hydroacoustic, infrasonic and seismic monitoring of the submarine eruptive activity and subaerial plume generation at South Sarigan, May 2010, *Journal of Volcanology and Geothermal Research*, *257*, 31–43, doi:10.1016/J.JVOLGEORES.2013.03.006.

Holt, M. (1977), UNDERWATER EXPLOSIONS, *Tech. rep.*

IRIS (2013), Special Event: North Korea nuclear explosion, http://ds.iris.edu/ds/nodes/dmc/specialevents/2013/02/12/north-korea-nuclear-explosion/, accessed 16 March 2016.

IRIS (2016), Special Event: 2016 North Korean nuclear test, https://ds.iris.edu/ds/nodes/dmc/specialevents/2016/01/05/2016-north-korean-nuclear-test/, accessed 16 March 2016.

Jensen, F. B., W. A. Kuperman, M. B. Porter, and H. Schmidt (2011), *Computational Ocean Acoustics*, Springer New York, New York, NY, doi:10.1007/978-1-4419-8678-8.

Kafka, A. L. (1990), Rg as a depth discriminant for earthquakes and explosions: A case study in New England, *Bulletin of the Seismological Society of America*, *80*(2), 373–394.

Kanamori, H., J. Mori, D. L. Anderson, and T. H. Heaton (1991), Seismic excitation by the space shuttle Columbia, *Nature*, *349*(6312), 781–782, doi:10.1038/349781a0.

Kausel, E. (2006), *Fundamental Solutions in Elastodynamics: A Compendium*, Cambridge University Press, doi:10.1017/CBO9780511546112.

Kelly, K. R., and R. W. Ward (1976), Synthetic Seismograms: A Finite-Difference Approach, *Tech. rep.*

Kennett, B. L. N., E. R. Engdahl, and R. Buland (1995), Constraints on seismic velocities in the Earth from travel times, *Geophysical Journal International*, *122*(June), 108–124, doi:10.1111/j.1365-246X.1995.tb03540.x.

Kim, K., and A. Rodgers (2016), Waveform inversion of acoustic waves for explosion yield estimation, *Geophysical Research Letters*, *43*(13), 6883–6890, doi:10.1002/2016GL069624.

Kim, W.-Y., D. W. Simpson, and P. G. Richards (1993), Discrimination of earthquakes and explosions in the eastern United States using regional high-frequency data, *Geophysical Research Letters*, *20*(14), 1507–1510, doi:10.1029/93GL01267.

Komatitsch, D., and J. Tromp (1999), Introduction to the spectral element method for three-dimensional seismic wave propagation, *Geophysical Journal International*, *139*(3), 806–822, doi:10.1046/j.1365-246x.1999.00967.x.

Komatitsch, D., C. Barnes, and J. Tromp (2000), Wave propagation near a fluidsolid interface: A spectralelement approach, *GEOPHYSICS*, *65*(2), 623–631, doi:10.1190/1.1444758.

Kosloff, D., D. Kessler, A. Q. Filho, E. Tessmer, A. Behle, and R. Strahilevitz (1990), Solution of the equations of dynamic elasticity by a Chebychev spectral method, *GEOPHYSICS*, *55*(6), 734–748, doi:10.1190/1.1442885.

Kulichkov, S. (2010), On the Prospects for Acoustic Sounding of the Fine Structure of the Middle Atmosphere, in *Infrasound Monitoring for Atmospheric Studies*, edited by A. Le Pichon, E. Blanc, and A. Hauchecorne, chap. 16, pp. 511–540, Springer, New York, USA.

Lalande, J.-M., O. Sèbe, M. Landès, P. Blanc-Benon, R. S. Matoza, A. Le Pichon, and E. Blanc (2012), Infrasound data inversion for atmospheric sounding, *Geophysical Journal International*, *190*(1), 687–701, doi:10.1111/j.1365-246X.2012.05518.x.

Lay, T., and T. C. Wallace (1995), *Modern Global Seismology*, 612pp. pp., Academic Press, San Diego, USA.

Le Pichon, A., J. Guilbert, M. Vallée, J. X. Dessa, and M. Ulziibat (2003), Infrasonic imaging of the Kunlun Mountains for the great 2001 China earthquake, *Geophysical Research Letters*, *30*(15), 2–5, doi:10.1029/2003GL017581.

Le Pichon, A., P. Mialle, J. Guilbert, and J. Vergoz (2006), Multistation infrasonic observations of the Chilean earthquake of 2005 June 13, *Geophysical Journal International*, *167*(2), 838–844, doi:10.1111/j.1365-246X.2006.03190.x.

Liu, J., L. Li, J. Zahradník, E. Sokos, C. Liu, and X. Tian (2018), North Korea's 2017 Test and its Nontectonic Aftershock, *Geophysical Research Letters*, *45*(7), 3017–3025, doi:10.1002/2018GL077095.

Lonzaga, J. B., R. M. Waxler, J. D. Assink, and C. L. Talmadge (2014), Modelling waveforms of infrasound arrivals from impulsive sources using weakly non-linear ray theory, *Geophysical Journal International*, *200*(3), 1347–1361, doi:10.1093/gji/ggu479.

Maranò, S., C. Reller, H.-A. Loeliger, and D. Fäh (2012), Seismic waves estimation and wavefield decomposition: application to ambient vibrations, *Geophysical Journal International*, *191*(1), 175–188, doi:10.1111/j.1365-246X.2012.05593.x.

Marchetti, E., G. Lacanna, A. Le Pichon, D. Piccinini, and M. Ripepe (2016), Evidence of Large Infrasonic Radiation Induced by Earthquake Interaction with Alluvial Sediments, *Seismological Research Letters*, *87*(3), 678–684, doi:10.1785/0220150223.

Martire, L., Q. Brissaud, V. H. Lai, R. F. Garcia, R. Martin, S. Krishnamoorthy, A. Komjathy, A. Cadu, J. A. Cutts, J. M. Jackson, D. Mimoun, M. T. Pauken, and A. Sournac (2018), Numerical Simulation of the Atmospheric Signature of Artificial and Natural Seismic Events, *Geophysical Research Letters*, *45*(21), 12,085–12,093, doi:10.1029/2018GL080485.

McDonald, B. E., and D. C. Calvo (2007), Enhanced sound transmission from water to air at low frequencies., *The Journal of the Acoustical Society of America*, *122*(6), 3159–3161, doi:10.1121/1.2793709.

Melton, B. S., and L. F. Bailey (1957), Multiple signal correlators, *Geophysics*, *22*(3), 565–588.

Mikhailenko, B. G., and A. A. Mikhailov (2014), Numerical modeling of seismic and acoustic-gravity waves propagation in an Earth-Atmosphere model in the presence of wind in the air, *Numerical Analysis and Applications*, *7*(2), 124–135, doi:10.1134/S1995423914020062.

Mikumo, T. (1968), Atmospheric pressure waves and tectonic deformation associated with the Alaskan earthquake of March 28, 1964, *Journal of Geophysical Research*, *73*(6), 2009–2025, doi:10.1029/JB073i006p02009.

Mikumo, T., T. Shibutani, A. Le Pichon, M. Garces, D. Fee, T. Tsuyuki, S. Watada, and W. Morii (2008), Low-frequency acoustic-gravity waves from coseismic vertical deformation associated with the 2004 Sumatra-Andaman earthquake (Mw = 9.2), *Journal of Geophysical Research: Solid Earth*, *113*(12), 1–11, doi:10.1029/2008JB005710.

Mueller, R. A., and J. R. Murphy (1971a), Seismic characteristics of underground nuclear detonations: Part I. Seismic spectrum scaling, *Bulletin of the Seismological Society of America*, *61*(6), 1675–1692.

Mueller, R. A., and J. R. Murphy (1971b), Seismic characteristics of underground nuclear detonations: Part II. Elastic energy and magnitude determinations, *The Journal of Geology*, *61*(6), 1693–1704, doi:10.1086/622062.

Munk, W. H. (1974), Sound channel in an exponentially stratified ocean, with application to SOFAR, *The Journal of the Acoustical Society of America*, *55*(2), 220–226, doi:10.1121/1.1914492.

Mutschlecner, J. P., and R. W. Whitaker (2005), Infrasound from earthquakes, *Journal of Geophysical Research*, *110*(D1), D01,108, doi:10.1029/2004JD005067.

Ostashev, V. E., D. K. Wilson, and D. K. Wilson (2015), *Acoustics in Moving Inhomogeneous Media*, CRC Press, doi:10.1201/b18922.

Pekeris, C. L. (1939), The Propagation of a Pulse in the Atmosphere, *Proceedings of the Royal Society A: Mathematical, Physical and Engineering Sciences*, *171*(947), 434–449, doi:10.1098/rspa.1939.0076.

Picone, J. M., A. E. Hedin, D. P. Drob, and A. C. Aikin (2002), NRLMSISE-00 empirical model of the atmosphere: Statistical comparisons and scientific issues, *Journal of Geophysical Research: Space Physics*, *107*(A12), SIA 15–1–SIA 15–16, doi:10.1029/2002JA009430.

Pierce, A. D. (2019), *Acoustics : an introduction to its physical principles and applications*, Springer International Publishing, doi:10.1007/978-3-030-11214-1.

Possee, D., D. Keir, N. Harmon, C. Rychert, F. Rolandone, S. Leroy, J. Corbeau, G. Stuart, E. Calais, F. IllsleyKemp, D. Boisson, R. Momplaisir, and C. Prépetit (2019), The Tectonics and Active Faulting of Haiti from Seismicity and Tomography, *Tectonics*, *38*(3), 1138–1155, doi:10.1029/2018TC005364.

Rayleigh, L. (1885), On Waves Propagated along the Plane Surface of an Elastic Solid, *Proceedings of the London Mathematical Society*, *s1-17*(1), 4–11, doi:10.1112/plms/s1-17.1.4.

Rougier, E., H. J. Patton, E. E. Knight, and C. R. Bradley (2011), Constraints on burial depth and yield of the 25 May 2009 North Korean test from hydrodynamic simulations in a granite medium, *Geophysical Research Letters*, *38*(16), n/a–n/a, doi:10.1029/2011GL048269.

Schmidt, H., and G. Tango (1986), Efficient global matrix approach to the computation of synthetic seismograms, *Geophysical Journal of the Royal Astronomical Society*, *84*(2), 331–359, doi:10.1111/j.1365-246X.1986.tb04359.x.

Scholte, J. G. (1947), THE RANGE OF EXISTENCE OF RAYLEIGH AND STONELEY WAVES, *Geophysical Journal International*, *5*(s5), 120–126, doi:10.1111/j.1365-246X.1947.tb00347.x.

Selby, N. D. (2010), Relative Locations of the October 2006 and May 2009 DPRK Announced Nuclear Tests Using International Monitoring System Seismometer Arrays, *Bull. Seism. Soc. Am.*, *100*(4), 1779–1784, doi:10.1785/0120100006.

Shani-Kadmiel, S., M. Tsesarsky, J. N. Louie, and Z. Gvirtzman (2014), Geometrical focusing as a mechanism for significant amplification of ground motion in sedimentary basins: analytical and numerical study, *Bulletin of Earthquake Engineering*, *12*(2), 607–625, doi:10.1007/s10518-013-9526-4.

Shani-Kadmiel, S., J. D. Assink, P. S. M. Smets, and L. G. Evers (2018), Seismoacoustic Coupled Signals From Earthquakes in Central Italy: Epicentral and Secondary Sources of Infrasound, *Geophysical Research Letters*, *45*(1), 427–435, doi:10.1002/2017GL076125.

Sharpe, J. A. (1942a), THE PRODUCTION OF ELASTIC WAVES BY EXPLOSION PRESSURES. I. THEORY AND EMPIRICAL FIELD OBSERVATIONS, *GEOPHYSICS*, *7*(2), 144–154, doi:10.1190/1.1445002.

Sharpe, J. A. (1942b), THE PRODUCTION OF ELASTIC WAVES BY EXPLOSION PRESSURES. II. RESULTS OF OBSERVATIONS NEAR AN EXPLODING CHARGE, *GEOPHYSICS*, *7*(3), 311–321, doi:10.1190/1.1445016.

Smart, E., and E. A. Flinn (1971), Fast Frequency-Wavenumber Analysis and Fisher Signal Detection in Real-Time Infrasonic Array Data Processing, *Geophysical Journal of the Royal Astronomical Society*, *26*, 279–284.

Smets, P. S., and L. G. Evers (2014), The life cycle of a sudden stratospheric warming from infrasonic ambient noise observations, *Journal of Geophysical Research*, *119*(21), 12,084–12,099, doi:10.1002/2014JD021905.

Smets, P. S., J. D. Assink, A. Le Pichon, and L. G. Evers (2016), ECMWF SSW forecast evaluation using infrasound, *Journal of Geophysical Research: Atmospheres*, *121*(9), 4637–4650, doi:10.1002/2015JD024251.

Smets, P. S. M., L. G. Evers, S. P. Näsholm, and S. J. Gibbons (2015), Probabilistic infrasound propagation using, *Geophysical Research Letters*, *42*, 6510–6517, doi:10.1002/2015GL064992.1.

Stoneley, R. (1926), The Effect of the Ocean on Rayleigh Waves., *Geophysical Journal International*, *1*(s7), 349–356, doi:10.1111/j.1365-246X.1926.tb05382.x.

Sykes, L. R., and G. C. Wiggins (1986), Yields of Soviet underground nuclear explosions at Novaya Zemlya, 1964-1976, from seismic body and surface waves., *Proceedings of the National Academy of Sciences of the United States of America*, *83*(2), 201–5, doi:10.1073/PNAS.83.2.201.

Tappert, F. D. (1977), The parabolic approximation method, in *Wave Propagation and Underwater Acoustics*, pp. 224–287, Springer Berlin Heidelberg, Berlin, Heidelberg, doi:10.1007/3-540-08527-0_5.

Tarantola, A. (2005), *Inverse Problem Theory and Methods for Model Parameter Estimation*, Society for Industrial and Applied Mathematics, doi:10.1137/1.9780898717921.

Tauzin, B., E. Debayle, C. Quantin, and N. Coltice (2013), Seismoacoustic coupling induced by the breakup of the 15 February 2013 Chelyabinsk meteor, *Geophysical Research Letters*, *40*(14), 3522–3526, doi:10.1002/grl.50683.

Tromp, J., C. Tape, and Q. Liu (2005), Seismic tomography, adjoint methods, time reversal and banana-doughnut kernels, *Geophysical Journal International*, *160*(1), 195–216, doi:10.1111/j.1365-246X.2004.02453.x.

Virieux, J. (1986), P-SV wave propagation in heterogeneous media: Velocitystress finitedifference method, *GEOPHYSICS*, *51*(4), 889–901, doi:10.1190/1.1442147.

Walker, K. T., A. L. Pichon, T. S. Kim, C. de Groot-Hedlin, I.-Y. Che, and M. Garcés (2013), An analysis of ground shaking and transmission loss from infrasound generated by the 2011 Tohoku earthquake, *J. Geophys. Res. Atmos.*, *118*(23), 12,831–12,851, doi:10.1002/2013jd020187.

Walter, W. R., K. M. Mayeda, and H. J. Patton (1995), Phase and spectral ratio discrimination between NTS earthquakes and explosions. Part I: Empirical observations, *Bulletin of the Seismological Society of America*, *85*(4), 1050–1067.

Wapenaar, C. P. A., and A. J. Berkhout (1989), *Elastic wave field extrapolation*, 468 pp., Elsevier.

Watada, S., T. Kunugi, K. Hirata, H. Sugioka, K. Nishida, S. Sekiguchi, J. Oikawa, Y. Tsuji, and H. Kanamori (2006), Atmospheric pressure change associated with the 2003 Tokachi-Oki earthquake, *Geophysical Research Letters*, *33*(24), 1–5, doi:10.1029/2006GL027967.

Waxler, R. (2004), Modal expansions for sound propagation in the nocturnal boundary layer, *The Journal of the Acoustical Society of America*, *115*(4), 1437–1448, doi:10.1121/1.1646137.

Waxler, R., L. G. Evers, J. D. Assink, and P. Blom (2015), The stratospheric arrival pair in infrasound propagation, *J. Acoust. Soc. Am.*, *137*(4), 1846–1856, doi:10.1121/1.4916718.

Waxler, R., J. Assink, and D. Velea (2017a), Modal expansions for infrasound propagation and their implications for ground-to-ground propagation, *The Journal of the Acoustical Society of America*, *141*(2), 1290–1307, doi:10.1121/1.4976067.

Waxler, R., J. Assink, and D. Velea (2017b), Modal expansions for infrasound propagation and their implications for ground-to-ground propagation, *The Journal of the Acoustical Society of America*, *141*(2), 1290–1307, doi:10.1121/1.4976067.

Weatherall, P., K. M. Marks, M. Jakobsson, T. Schmitt, S. Tani, J. E. Arndt, M. Rovere, D. Chayes, V. Ferrini, and R. Wigley (2015), A new digital bathymetric model of the world's oceans, *Earth and Space Science*, *2*, 331–345, doi:10.1002/2015EA000107.

Wen, L., and H. Long (2010), High-precision Location of North Korea's 2009 Nuclear Test, *Seism. Res. Lett.*, *81*(1), 26–29.

Werth, G. C., and R. F. Herbst (1963), Comparison of amplitudes of seismic waves from nuclear explosions in four mediums, *Journal of Geophysical Research*, *68*(5), 1463–1475, doi:10.1029/JZ068i005p01463.

Whitaker, R. W., and J. P. Mutschlecner (2008), A comparison of infrasound signals refracted from stratospheric and thermospheric altitudes, *Journal of Geophysical Research Atmospheres*, *113*(8), 1–13, doi:10.1029/2007JD0008852.

Wilson, A. H. (1957), *Thermodynamics and Statistical Mechanics*, 495 pp., University Press.

Young, J. M., and G. E. Greene (1982), Anomalous infrasound generated by the Alaskan earthquake of 28 March 1964, *The Journal of the Acoustical Society of America*, *71*(2), 334–339, doi:10.1121/1.387457.

Yue, J., C. Y. She, and H. L. Liu (2010), Large wind shears and stabilities in the mesopause region observed by Na wind-temperature lidar at midlatitude, *Journal of Geophysical Research: Space Physics*, *115*(10), 1–12, doi:10.1029/2009JA014864.

Zhang, M., and L. Wen (2015), Seismological Evidence for a Low-Yield Nuclear Test on 12 May 2010 in North Korea, *Seism. Res. Lett.*, *86*(1), 138–145, doi:10.1785/02201401170.

,

List of symbols and abbreviations

Symbols

The principal symbols used are alphabetically listed. Symbols formed by adding overbars, primes or indices are not listed separately. Boldface type indicates vector quantities.

Symbol	Description	Units
$\aleph^{\text{visc}}$	viscous energy dissipation	Pa
ϵ	Strain	-
	Small number	-
θ	Azimuth	degrees
λ	Lamé first parameter	Pa
Λ	Potential	-
κ	Thermal conductivity	W/mK
μ	Shear modulus	Pa
	Mean	-
ρ	Density field	kg/m^3
σ	Stress	Pa
	Variance	-
Φ	Pressure–displacement potential	m^2
Ψ	Shear–displacement potential	m^2
ω	angular frequency	rad
A	Amplitude	-
B	Amplitude	-
c	Speed of sound	m/s

Symbol	Description	Units
c_{eff}	Effective speed of sound	m/s
f	Frequency	1/s
g	Gtravity constant	m/s^2
G	Forward model	-
I	Identity matrix	-
I_w	Tropospheric phases	-
I_s	Stratospheric phases	-
I_{ws}	Combined phases	-
$J_{0/1}$	First kind Bessel function	-
$\boldsymbol{k}$	Wavenumber	1/m
K	Bulk modulus	Pa
$\boldsymbol{m}$	Model parameters	-
$\boldsymbol{M}$	Observation	-
m_b	Body-wave magnitude	-
M_w	Moment magnitude	-
$\hat{n}$	Direction	-
p	Pressure field	Pa
Q	Quality factor	-
r	Distance	m
R	Gas constant	J/K mol
S	Source strength	m^3
	Entropy	J/K
SNR	Signal-to-noise ratio	-
t	time	s
T	Temperature	°C
TL	Transmission loss	dB
$\boldsymbol{u}$	Displacement field	m
u	Horizontal displacement	m
v	velocity field	Pa
v_p	Pressure waves velocity	m/s
v_s	Shear waves velocity	m/s
$v_{surface}$	Surface waves velocity	m/s
w	Vertical displacement	m
$\boldsymbol{W}$	Wind	m/s
$\boldsymbol{x}$	position	m
z	vertical distance	m

Abbreviations

CTBT	Comprehensive Nuclear-Test-Ban Treaty
CTBTO	Comprehensive Nuclear-Test-Ban Treaty Organization
DGM	Direct Global Matrix
DPRK	Democratic People's Republic of Korea
ECMWF	European Centre for Medium-Range Weather Forecasts
FFP	Fast Field Program
FFT	Fast Fourier Transform
GMT	Generic Mapping Tools
HRES EDA	High Resolution Ensemble of Analysis
HWN	Horizontal Wind Model
IMS	International Monitoring System
IFFT	Inverse Fast Fourier Transform
KNMI	Royal Netherlands Meteorological Institute
MSIS	Mass Spectrometer and Incoherent Scatter radar
MIL	Mesospheric Inversion Layer
PE	Parabolic Equation
SOFAR	Sound Fixing and Ranging
SSW	Sudden Stratospheric Warming
UTC	Universal Time Coordinated

Publications

Peer-reviewed publications

2020

- Long-range atmospheric infrasound propagation from subsurface sources
  G. Averbuch, J. D. Assink, L. G. Evers
  The Journal of the Acoustical Society of America, 2020, accepted

- Probabilistic inversion for submerged source depth and strength from infrasound observations
  G. Averbuch, R. Waxler, P. S. M. Smets, L. G. Evers
  The Journal of the Acoustical Society of America, 2020, 147 (2), pp: 1066-1077, doi.org/10.1121/10.0000695

- CLEAN beamforming for the enhanced detection of multiple infrasonic sources
  O. F. C. den Ouden, J. D. Assink, P. S. M. Smets, S. Shani-Kadmiel, **G. Averbuch**, and L. G. Evers
  Geophysical Journal International, 2020, 221 (1), pp: 305317, doi.org/10.1093/gji/ggaa010

- Infrasound observations of sprites associated with winter thunderstorms in the eastern mediterranean
  D. Applbaum, **G. Averbuch**, C. Price, Y. Yair, Y. Ben-Horin
  Atmospheric Research, 2020, 235, pp: 104770, doi.org/10.1016/j.atmosres.2019.104770

2019

- The Mount Meron Infrasound Array: an infrasound array without a noise reduction system
  G. Averbuch, Y. ben-Horin, P. S. M. Smets, L. G. Evers
  Geophysical Journal International, 2019, 219 (2), pp: 1109-1117, doi.org/10.1093/gji/ggz350

2018
- A Seismo-Acoustic Analysis of the 2017 North Korean Nuclear Test
  J. D. Assink, **G. Averbuch**, S. Shani-Kadmiel, P. S. M. Smets, L. G. Evers
  Seismological Research Letters, 2018, 89 (6), pp: 2025-2033, doi.org/10.1785/0220180137
- Extracting low signal-to-noise ratio events with the Hough transform from sparse array data
  G. Averbuch, J. D. Assink, P. S. M. Smets, L. G. Evers
  Geophysics, 83(3), WC43-WC51, doi:10.1190/GEO2017-0490.1

2016
- On the infrasound detected from the 2013 and 2016 DPRK's underground nuclear tests
  J. D. Assink, **G. Averbuch**, P. S. M. Smets, and L. G. Evers
  Geophys. Res. Lett. (2016), 43, 3526–3533, doi:10.1007/s10712-017-9444-0